Technische Universität München
Physik Department E18

The Free Neutron β-Decay: A Powerful Tool for the Investigation in Particle Physics

Xiangzun Wang

Vollständiger Abdruck der von der Fakultät für **Physik** der Technischen Universität München zur Erlangung des akademischen Grades eines
Doktors der Naturwissenschaften
genehmigten Dissertation.

Vorsitzender: Univ.-Prof. Dr. Björn Garbrecht

Prüfer der Dissertation:

1. Univ.-Prof. Dr. Hartmut Abele
2. Univ.-Prof. Dr. Peter Fierlinger

Die Dissertation wurde am 23.11.2012 bei der Technischen Universität München eigereicht und durch die Fakultät für **Physik** am 20.03.2013 angenommen.

Abstract

The free neutron β decay provides a clean environment for the researches in particle physics. In this semi-leptonic decay, all of the quarks and leptons in the first generation are involved, and both the weak and strong interactions take part in the process. Hence plenty of measurable quantities are accessible in the neutron decay, and indicate the characters of different particles and interactions. Further, precise measurements of the quantities may imply the new physics and new symmetry concepts, which are excluded from the Standard Model.

In the first part of this dissertation, we introduce the β asymmetry measurement with the PERKEOIII spectrometer during the beam time of the Institut Laue Langevin in 2008-2009. In the experiment, the pulsed neutron beam was applied, in which case the systematic errors are sufficiently decreased. From a preliminary data analysis, we deduce the angular correlation coefficient A and the Axial-vector Vector coupling ratio λ. Compared with the latest values given by the Particle Data Group, the results from the PERKEOIII measurement are expected to be 5 times more precise.

In the second part, we present the design of the next generation of neutron decay product spectrometer PERC, which aims to measure the electron and proton spectra, as well as the correlation coefficients in free neutron decay with high precisions. With the well defined decay volume and magnetic field, the observables are expected to be measured distortion-free on 10^{-4} level. We studied the physical, systematic, and experimental properties of PERC. To realize the momentum analyses of the decay products, we propose a method of $\mathbf{R}\times\mathbf{B}$ drift momentum spectrometer.

In the PERKEOIII experiment and the PERC design, different kinds of simulations were applied for investigating the neutron properties, magnetic field, and the trajectories of electrons and protons. With the simulation results, we obtain better understanding of the systems, further determine the systematic effects and corrections.

Zusammenfassung

Der β-Zerfall des freien Neutrons bietet eine saubere Umgebung für Forschungen in der Teilchenphysik. An diesem semi-leptonischen Zerfall sind alle Quarks und Leptonen der ersten Generation beteiligt. Beide, die schwache und die starke Wechselwirkung, nehmen an diesem Prozess Teil. Daher sind zahlreiche Messgrößen im Neutronenzerfall zugänglich, welche die Eigenschaften vieler verschiedener Teilchen und Wechselwirkungen beschreiben. Außerdem können Präzisionsmessungen dieser Größen neue Physik und neue Symmetriekonzepte implizieren, die im Standardmodell ausgeschlossen sind.

Im ersten Teil dieser Dissertation führen wir die Messung der β-Asymmetrie mit dem PERKEO III Spektrometer während der 2008/2009 Strahlzeit am Institut Laue-Langevin ein. Das Experiment wurde mit gepulstem Neutronenstrahl durchgeführt, wodurch der systematische Fehler ausreichend reduziert werden konnte. In einer vorläufigen Datenanalyse haben wir den Winkelkorrelationskoeffizienten A und das Axial-Vektor zu Vektor-Kopplung-Verhältnis λ bestimmt. Im Vergleich zu den letzten Particle Data Group Werten, erwarten wir, dass die Ergebnisse der PERKEO III Messung fünfmal präziser sind.

Im zweiten Teil präsentieren wir das Design des PERC Spektrometers - die nächste Generation eines Spektrometers zur Untersuchung der Zerfallsteilchen im Neutronenzerfall. Ziel des PERC Instrumentes ist es, die Spektren der Zerfallselektronen und –protonen sowie die Korrelationskoeffizienten im freien Neutronenzerfall mit hoher Präzision zu messen. Dank des wohldefinierten Zerfallsvolumens und des wohldefinieren Magnetfeldes können wir die Observablen verzerrungsfrei auf dem 10^{-4} Niveau zu messen. Wir haben die physikalischen, systematischen und experimentellen Eigenschaften von PERC untersucht. Zur Realisierung der Impulsanalyse der Zerfallsteilchen schlagen wir die Methode eines $\mathbf{R}\times\mathbf{B}$ -Drift Impulsspektrometers vor.

Im PERKEO III Experiment und im PERC Design wurden verschiedene Arten der Simulation angewandt, zur Untersuchung von Neutroneneigenschaften, Magnetfeld, und Teilchenbahnen der Elektronen und Protonen. Durch die Simulationsergebnisse erhalten wir ein besseres Verständnis beider Systeme und bestimmen ferner die systematischen Effekte und Korrekturen.

Contents

Chapter 1

Introduction

The β-decay of the free neutron, as the most general weak process, is a powerful tool for the researches in various areas of particles physics and cosmology.

A free neutron is not stable. It can decay into a proton p^+, an electron e^-, and an electron anti-neutrino $\bar{\nu}_e$ with the life time τ as 880.1 s.

$$n(udd) \rightarrow p^+(uud) + e^- + \bar{\nu}_e + 782.3 \text{ keV} \tag{1.1}$$

This semi-leptonic decay process includes all of the leptons and the quarks in the first generation, and is mainly induced by the weak interaction. In the mean time, the strong interaction also takes part in the process, and determines the characters of the decay. Therefore, a large number of measurable quantities which reflect the properties of the particles and interactions, e.g. the Axial-vector and Vector ratio λ, the V_{ud} element of CKM matrix, and various angular correlation coefficients, are accessible in the free neutron decay. These quantities are important parameters, and have been used in various domains of theoretical and experimental physics.

Furthermore, there is ample room in the measurement of neutron β-decay for searching new physics beyond the Standard Model. By investigating the observables in the decay precisely, we are able to determine the limits of some quantities that are excluded from the Standard Model. In particular, the quantities including

- the mass and the mixing angle of the right-handed weak boson in the left-right symmetry model;
- the unitarity of CKM matrix;
- the Scalar and Tensor interactions;
- the time reversal violation;

are able to be tested in the low energy neutron decay. These quantities may imply new physics and new symmetry concepts, which are related to the grand unifications of the interactions, supersymmetry, and extra particles etc..

Because of the absence of the nuclear structure influences, the free neutron β-decay supplies a clean environment for the precise tests of the theories. The precise measurements in low energy scale are generally complementary to the researches in high energy physics.

From 2008-11 to 2009-08, we performed a β-asymmetry measurement with the spectrometer PERKEOIII at the research reactor of the Institute Laue Langevin in Grenoble. In the experiment, the pulsed neutron beam was applied, with which the systematic errors, e.g., from the neutron related background, the electron edge effect, and the magnetic field inhomogeneity, are considerably suppressed.

Besides the experiment with PERKEOIII, the next generation of the neutron decay product spectrometer, the beam station PERC is also designed and studied. The motivation of PERC is to perform the measurements of the electron and proton spectra, and the angular correlation coefficients in high precision. With the well defined decay volume, the detection system, and the specified functional magnetic field system, the charged decay products can be measured with distortion-free on the level of 10^{-4}, and the precisions of the observables in the neutron decay are expected to be improved by one order of magnitude.

In Chapter 2, we provide a brief introduction to the theories of the weak interaction and the neutron decay in the framework of Standard Model, also in the extended theories excluded from the Standard Model.

In Chapter 3, we introduce the PERKEOIII spectrometer, and the experiment performed in 2008-2009 for the β asymmetry measurement. The properties of the pulsed neutrons, and the characters of the magnetic field in the experiment are studied in Chapter 4. In Chapter 5, we analyse the data from the measurements, and derive the values of angular correlation coefficient A and the coupling ratio λ.

In Chapter 6, we introduce the motivation and the principles of PERC. In Chapter 7, we introduce the design of PERC magnet system, and study the magnetic field, as well as the electron and proton trajectories inside PERC. Chapter 8 introduces the experimental properties of PERC instrument, the components related to PERC, and some possible post spectrometers. The new type of $\mathbf{R}\times\mathbf{B}$ drift spectrometer for momentum analyses is also introduced.

In Chapter 9, we conclude a summary of the work. An introduction to the V–A theory is given in Appendix A, and the motion of the charged particles in static magnetic field is introduced in Appendix B.

During the PERKEOIII experiment and the design of PERC, different kinds of simulation programs were applied, e.g., for the calculations of the neutron behaviour, the magnetic field, and the trajectories of the charged particles. The simulated results are further used in the data selection, the determination of systematic corrections, and design optimization etc..

Chapter 2

Theories of Weak Interaction and Neutron Decay

The nuclear and neutron β-decay played prominent roles in developing the theories of the particle physics to the Standard Model nowadays. Although the Standard Model has been very successful till now, there are still plenty of open questions in the fields of particle physics and cosmology. In this case, many new physics theories beyond the Standard Model have been proposed. In the area of weak interaction, the precise measurements of the neutron β-decay supply unique opportunities to search the new physics beyond the Standard Model.

In this chapter, we provide a brief introduction to the theories of the weak interaction and the neutron β-decay in the frame of Standard Model. Then we introduce some theoretical extensions of Standard Model, and the expected limits of the quantities in these theories determined by the present and possible future values of observables in neutron decay.

2.1 Theories of Weak Interaction

In 1896, Becquerel discovered the radioactivity from the uranium crystals. From then, the vision of physics was extended to the nuclear field. Till 1904, the electrically charged β-rays were verified as electrons with very high energies. After the neutron was discovered in 1932 [Cha32], it became evident that the electron is created simultaneously when a neutron transforms into a proton. Besides, the β-rays were discovered containing both discrete and continuous energy spectra [Cha14]. Because both the initial and final nuclei have defined energies, the continuous β spectrum was difficult to understand, since it means the violation of energy conservation. To solve this problem, Pauli proposed in 1930s that an additional neutral particle with small mass should also be emitted besides the electron in the decay, and carries part of the decay energy. The particle is the so called (electron anti-) neutrino (named by Fermi), and was indirectly discovered in 1956 in the β capture experiment.

In 1934, Fermi developed Pauli's hypothesis into a quantitative theory [Fer34]. The theory postulates that the β-decay process can be described by adding an interaction term into the

Hamiltonian:

$$H = H_n^0 + H_p^0 + H_e^0 + H_\nu^0 + H_{int}$$
$$H_{int} = \frac{G_F}{\sqrt{2}} \sum_i C_i \int (\bar{u}_p \hat{O}_i u_n)(\bar{u}_e \hat{O}_i u_\nu) \mathrm{d}^3x + h.c. \tag{2.1}$$

$u_{n,p,e,\nu}$ and $\bar{u}_{n,p,e,\nu}$ denote the wave functions of neutron, proton, electron and neutrino, and their Dirac adjoints. The $\hat{O}_i$ are proper operators to characterize the properties of the interaction, and are weighted by constants C_i. G_F is the Fermi coupling constant. The interaction term follows the current-current coupling, that is used in describing the scattering or radiation processes in electrodynamics. In the currents, neutron transforms into proton, and (electron) neutrino transforms into electron. The four particles interact at the same point of space-time, with their charges and the flavors changed.

From 1938, people found in the experiments, that almost the same coupling constants $G_F \approx 10^{-11}\mathrm{MeV}^{-2}$ appears in different decay processes, e.g. μ decay, π decay, and K decay. Therefore, it was realized that the decay processes are dominated by an individual and universal interaction: the so-called weak interaction.

As it is known now, the weak interaction or the weak nuclear force is one of the four fundamental interactions. It has a strength between the gravitational and the electromagnetic interaction, but has the shortest action range in the four interactions.

	Gravity	Weak Nuclear	Electromagnetic	Strong Nuclear
Relative Strength	10^{-41}	10^{-15}	10^{-2}	1
Action Range	∞	$\ll 1$ fm	∞	≈ 1 fm

Table 2.1: The relative strengths and action ranges of the four fundamental interactions [Gre00].

In contrast to the other interactions, the short action range does not allow the weak interaction to produce bound states. But the weak interaction is the only one to induce the flavor changes of particles, as implied in eqn. 2.1.

From 1950s, the parity problem in the weak interaction arose. It was discovered that the K meson could decay into two pions $\pi^+\pi^0$, also into three pions $\pi^+\pi^+\pi^-$. Since the $\pi^{\pm,0}$ meson has negative (-1) intrinsic parity, the two decay processes result in 1 and -1 intrinsic parity of the initial K. To solve the problem, Lee and Yang proposed in 1956 a revolutionary method: the parity conservation is violated in the weak interaction [LY56]. The parity violation (P-violation) was soon confirmed in 1957 in the famous Wu's experiment [Wu57]. It was discovered in the experiment, in the pure Gamov-Teller transition (see Appendix A.3) of the ^{60}Co decay

$$^{60}Co(5\hbar) \rightarrow {}^{60}Ni(4\hbar) + e^-(\hbar/2) + \bar{\nu}_e(\hbar/2) \tag{2.2}$$

the majority of the electrons are emitted opposite to the nuclear spin, thus also opposite to the electrons spin, namely the electrons predominantly have negative helicities. Under the space inversion (parity transformation), the electron momentum reverses direction,

whereas the nucleus spin remains. Hence the decay process is not conserved under the parity transform, i.e., the parity conservation is violated.

After the Wu's experiments, it was discovered that the neutrino also has negative helicity [Gol58]. Based on these results, the $V-A$ theory was developed from Fermi's theory in 1957-1958. The $V-A$ theory assumes that the P-violation is maximal in the weak interaction processes, namely only leptons of negative helicity (left-handed), and anti-leptons with positive helicity (right-handed) participate in the weak interactions. The projection operators on the states of positive and negative helicities (more accurate: chiralities) are

$$\hat{P}_+ = \frac{1+\gamma_5}{2} \quad , \quad \hat{P}_- = \frac{1-\gamma_5}{2} \tag{2.3}$$

The interaction term in Hamiltonian of the weak interaction is then represented as

$$H_{int}(n,p,e,\nu) = \frac{G_F}{\sqrt{2}} V_{ud} \int [\bar{u}_p \gamma^\mu (g_V + g_A \gamma_5) u_n][\bar{u}_e \gamma_\mu (1-\gamma_5) u_\nu] \mathrm{d}^3 x \tag{2.4}$$

where only the vector (V) current and the axial vector (A) current appear in the interaction. The constants g_V and g_A in the hadronic current denote the strengths of Vector and Axial vector couplings. V_{ud} is the ud element of the CKM matrix, which describes the strengths of the couplings between up-type and down-type quarks in the weak interactions [Cab63, KM73]. A detailed introduction to the $V-A$ theory is given in Appendix A.

In 1960s, Glashow, Weinberg, and Salam developed a gauge-invariant theory of the weak interaction, based on the $SU(2)_L \times U(1)$ gauge symmetry group [Gla61, Wei67, Sal68]. In this theory, the weak process is not contact interaction, but mediated by three gauge bosons W^+, W^-, and Z^0 in the $SU(2)_L$ group, for charged and neutral currents respectively. The propagator that mediates the weak interaction is

$$iG_{\mu\nu}(q^2) = -i\frac{g_{\mu\nu} - \frac{q_\mu q_\nu}{m_W^2}}{q^2 - m_W^2} \tag{2.5}$$

where $g_{\mu\nu}$ is the metric tensor, q denotes the 4 dimensional momentum transfer, and m_W is the mass of the weak boson. The weak coupling constant G_F in the limit of low momentum transfer is then dependent on the mass of W boson

$$\frac{G_F}{\sqrt{2}} = \frac{g^2}{8m_W^2}, \quad \text{when} \quad q \to 0 \tag{2.6}$$

with g the coupling strength between the weak boson and the fermions.

In the gauge theory, the massless photon γ in the electromagnetic interaction appears as the forth boson, which is an admixture of the neutral boson eigenstate W_0 in $SU(2)$ group, and the eigenstate B_0 in $U(1)$ group. Hence the electrical charge has a relation to the weak coupling strength

$$e = g \sin\theta_W \tag{2.7}$$

with θ_W the weak mixing (Weinberg) angle. Therefore, the theory unifies the electromagnetic interaction and the weak interaction into the QFD (Quantum Flavordynamics) or Electroweak theory. In the unified theory, the weak bosons receive masses through the Higgs mechanism due to the spontaneous electroweak symmetry breaking.

In 1970s, the Standard Model (SM) was developed as a framework of QFD ($SU(2)_L \times U(1)$) and QCD (Quantum Chromodynamics, $SU(3)_C$), and refers to the strong and electroweak interactions, as well as their carrier particles.

In Standard Model, the matter of the universe is composed by twelve spin-1/2 elementary particles: six leptons and six quarks in three generations. According to their chiralities, the particles are arranged in left-handed $SU(2)_L$ isospin doublets and right-handed singlets [Don94]

$$\begin{pmatrix} \nu_e \\ e_L^- \end{pmatrix}, \quad \begin{pmatrix} \nu_\mu \\ \mu_L^- \end{pmatrix}, \quad \begin{pmatrix} \nu_\tau \\ \tau_L^- \end{pmatrix}, \quad e_R^-, \quad \mu_R^-, \quad \tau_R^- \tag{2.8}$$

$$\begin{pmatrix} u_L \\ d_L \end{pmatrix}, \quad \begin{pmatrix} c_L \\ s_L \end{pmatrix}, \quad \begin{pmatrix} t_L \\ b_L \end{pmatrix}, \quad u_R, \quad d_R, \quad c_R, \quad s_R, \quad t_R, \quad b_R \tag{2.9}$$

The neutron decay in Standard Model is expressed as the decay of a down quark (d) into an up quark (u) with the emission of a charged W^- boson. The W^- boson then decays into an electron and an anti-neutrino.

Since the W boson is very massive as 75 GeV, it has very short action range in the weak process with low momentum transfer $q \ll m_W$. The weak process thus can be simplified as a current-current interaction at a single point of space-time, as represented by Fermi's theory in eqn. 2.4. Figure 2.1 shows the Feynman diagrams of the mediated interaction and the four-fermion contact interaction in the neutron decay.

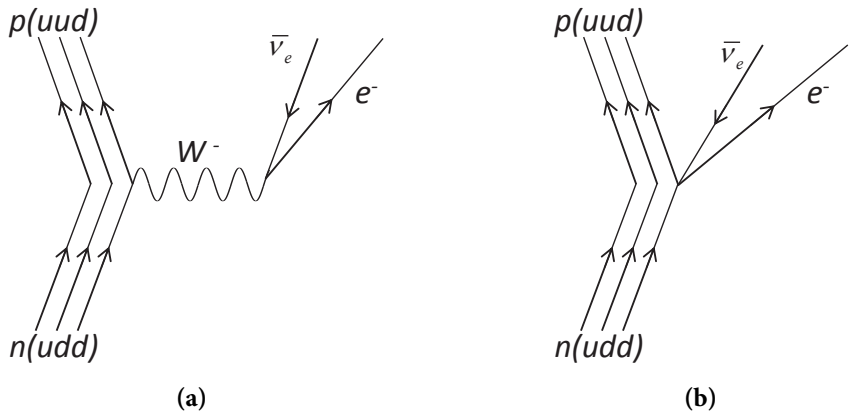

Figure 2.1: (a) Feynman diagram of neutron decay in Standard Model. The interaction is mediated by a charged W^- boson. **(b)** Feynman diagram of neutron decay in Fermi's theory. In the low energy limit $q \ll m_W$, the process is simplified as four-fermion contact interaction at a single vertex.

2.2 Observables in Neutron β-Decay

In the Standard Model, the free neutron decay is governed by four individual parameters: the weak coupling constants G_F, the ud element of the CKM matrix V_{ud}, the ratio of Axial-vector and Vector couplings λ, and the phase angle Φ [Abe08].

Besides, there are a series of quantities can be observed in the decay process. Table 2.2 lists some of the observables in the free neutron decay and the latest measured values.

Observable		Value
β Asymmetry	A	-0.1176(11)
Neutrino Asymmetry	B	0.9807(30)
Proton Asymmetry	C	-0.2377(26)
e^--$\bar{\nu}_e$ Correlation	a	-0.103(4)
Coupling Ratio	λ	-1.2701(25)
Life Time	τ	880.1(11)

Table 2.2: List of the present values of the observables in the free neutron decay. The values are from [PDG12]

2.2.1 Decay rate and angular correlation coefficients

From the Hamiltonian in eqn. 2.4 (more general form as eqn. 2.57), the decay rate of a free neutron can be derived as [Jac57]:

$$W\,\mathrm{d}E_e\mathrm{d}\Omega_e\mathrm{d}\Omega_\nu = \frac{1}{(2\pi)^5}\frac{G_F^2|V_{ud}|^2}{2}F(E)\mathrm{d}E_e\mathrm{d}\Omega_e\mathrm{d}\Omega_\nu\times \\ \xi\left[1+a\frac{\mathbf{p}_e\cdot\mathbf{p}_\nu}{E_eE_\nu}+b_F\frac{m_e}{E_e}+\langle\boldsymbol{\sigma}_n\rangle\left(A\frac{\mathbf{p}_e}{E_e}+B\frac{\mathbf{p}_\nu}{E_\nu}\right)+\cdots\right] \quad (2.10)$$

The $\mathbf{p}_e$, $\mathbf{p}_\nu$, E_e and E_ν are the momenta and total energies of the emitted e^- and $\bar{\nu}_e$, $\langle\boldsymbol{\sigma}_n\rangle$ is the unit vector of the neutron spin state.

$F(E)$ is the phase space factor of electron derived from Fermi's Golden Rule:

$$F(E) = \frac{(2\pi\hbar)^6}{V^2}\frac{\mathrm{d}n}{\mathrm{d}E_0} = (E_0-E_e)^2E_e\sqrt{E_e^2-m_e^2} \quad (2.11)$$

which also describes the energy spectrum of the emitted electrons. E_0 is the end point energy of electron in free neutron decay, when assuming the mass of $\bar{\nu}_e$ is negligible:

$$E_0 = \frac{m_n^2-m_p^2+m_e^2}{2m_n} = 1.2927\ \ \mathrm{MeV} \quad (2.12)$$

The kinetic end point energy of e^- is then

$$E_{k0} = E_0 - m_e = 781.6 \text{ keV} \tag{2.13}$$

The parameters A, B, and a in eqn. 2.10 are the angular correlation coefficients, which describe the distributions of emitted e^-, p^+, and $\bar{\nu}_e$ related to the neutron spin state $\langle \boldsymbol{\sigma}_n \rangle$. Another coefficient C, which represents the proton asymmetry according to neutron spin, is measurable in neutron decay. The coefficient C is related to the β and neutrino asymmetries A and B [Tre58, Glu95]

$$C = -x_C(A + B), \quad \text{with} \quad x_C = 0.27484 \tag{2.14}$$

where x_C is the kinematical factor. Figure 2.2 sketches the angular coefficients in the free neutron decay.

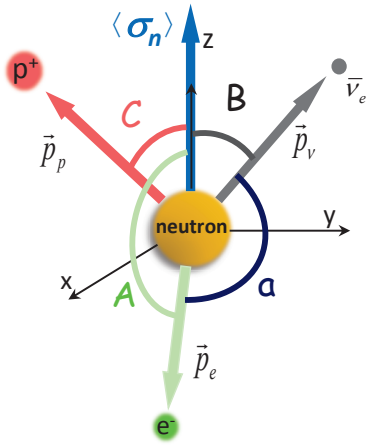

Figure 2.2: A sketch of the angular correlation coefficients in the neutron decay.

The Fierz term b_F indicates the interferences of Scalar and Vector, Tensor and Axial-vector currents as introduced in Section 2.3.3.

2.2.2 Ratio of Axial-vector and Vector couplings

The hadronic transition current in eqn. 2.4 does not show an exact $V-A$ coupling, but has the coupling constants g_V and g_A to weight the V and A contributions. This effect is induced not only by the weak interaction, but also by the strong interactions.

The vector coupling constant g_V equals one, because of the charge conservation in the vector interaction (the hypothesis of Conserved Vector Current, CVC). Whereas the quantity g_A is considerably modified by the p^+-n-$W^\pm$ coupling of the strong interaction, which is induced by simultaneous pion exchanges. Define the ratio of g_A and g_V as

$$\lambda = \frac{g_A}{g_V} = \left|\frac{g_A}{g_V}\right| e^{i\Phi} \tag{2.15}$$

with Φ the phase angle between g_V and g_A, which are complex quantities if the time reversal conservation is violated (T-violation) [1] [2].

Therefore, the λ is an important parameter to represent the strong interactions and the structures inside the nucleon, and the neutrino cross-section calculation. Practically, it has been used in the researches of nuclear theories and cosmology, e.g. the quark models calculations, the neutrino detector calibration, the solar neutrino flux, the supernova physics, and the big bang cosmology.

In the framework of the Standard Model, the S, T couplings are not predicted, and the T-violation in the neutron decay is extremely small (Section 2.3.4). Hence the λ has a real value, and Fierz term b_F equals zero. From eqn. 2.10, λ can be derived with the angular correlation coefficients

$$A = -2\frac{\lambda^2+\lambda}{1+3\lambda^2}, \quad B = 2\frac{\lambda^2-\lambda}{1+3\lambda^2}, \quad a = \frac{1-\lambda^2}{1+3\lambda^2} \tag{2.16}$$

Experimentally, the A, B and a are measured separately, and are used to deduce respective values of λ. The differences of the values may imply new physics excluded by Standard Model (Section 2.3).

2.2.3 Corrections on observables

In the spin-1/2 baryon semi-leptonic decay, the hadronic current in the element of the transition matrix has a general form [CB83]

$$J_H = \bar{u}_f[f_1(q^2)\gamma_\mu + if_2(q^2)\sigma_{\mu\nu}q^\nu + g_1(q^2)\gamma_\mu\gamma_5 + g_3(q^2)\gamma_5 q_\mu]u_i \tag{2.17}$$

$u_{f,i}$ are the spinors of the final and initial baryons, q^μ is the 4-component momentum transfer

$$q^\mu = p_i^\mu - p_f^\mu \tag{2.18}$$

f_1 and f_2 denotes the form factors of the vector current and the induced tensor (weak magnetism) corresponding to the vector matrix element. g_1 and g_3 denotes the form factors of the axial vector current and the induced pseudoscalar corresponding to the axial vector matrix element. [3]

In the limit of low momentum transfer of neutron decay, f_1 and g_1 approach to the Vector and Axial-vector coupling constants

$$g_V = f_1(q^2 \to 0) \quad , \quad g_A = g_1(q^2 \to 0) \tag{2.19}$$

[1] Φ is 180° in Standard Model [Don94].

[2] In some literatures, the absolute values $|g_A|$ and $|\lambda|$ are used, e.g. [Wil82]. In this dissertation, it is always defined $g_A < 0$ and $\lambda < 0$.

[3] In $SU(3)$ limit, the current invariance under G-parity results in the vanishing form factors f_3 and g_2 (a non-zero g_2 can appear due to EM effects and quark mass differences in SM. [Abe08]). Beyond this limit, these factors induce little effects on the spectra on 10^{-4} level [Hol74]. Hence f_3, g_2 are neglected here.

In the transitions with $e^{\pm}$ emissions, the term related to g_3 is proportional to q, thus to m_e. The induced effects on the spectra is negligible as 10^{-4}.

f_2 denotes the difference of the corresponding form factors of p^+ and n, $F_2^{p,n}(q^2)$. In $q^2 \to 0$ limit, F_2 represents the anomalous magnetic momenta of the particles, thus f_2 represents the weak magnetism [PDG12]

$$f_2(q^2) = F_2^p(q^2) - F_2^n(q^2) \xrightarrow{q^2 \to 0} \mu_p^a - \mu_n^a = (2.793 - 1) - (-1.913) = 3.706 = \kappa \quad (2.20)$$

In the precise measurements of neutron decay, we can count in the corrections of angular correlation coefficients from the weak magnetism, the proton recoil, and the radiation on the first order.

With the contributions from the weak magnetism and the proton recoil, the hadronic current becomes [Hol74]

$$J_H = \bar{u}_p \left(g_V \gamma^\mu + g_A \gamma^\mu \gamma_5 - i \frac{\kappa}{2M} \sigma^{\mu\nu} q^\nu \right) u_n \quad (2.21)$$

where M is the average mass of the neutron and the proton

$$M = \frac{m_n + m_p}{2} = 928.92 \ \text{MeV} \quad (2.22)$$

The radiative corrections are induced by the exchanges of γ, $W^{\pm}$ and Z^0 bosons, QCD structures [Sir75] and inner bremsstrahlung [Cza07].

Considering the contributions of proton recoil, weak magnetism and radiative correction, which are related to M, κ and electromagnetic fine structure constant α, the electron asymmetry is expressed as [Wil82]

$$A(E_e) = A_0 \left[1 + A_{\mu M} \left(A_1 E_0 + A_2 E_e + A_3 \frac{m_e^2}{E_e} \right) \right] \left[1 + \frac{\alpha}{\pi} f_n(E_e) \right] \quad (2.23)$$

with

$$A_{\mu M} = \frac{-\lambda + \kappa + 1}{-\lambda(1+\lambda)(1+3\lambda^2)M} \quad (2.24)$$

$$A_1 = \lambda^2 - \frac{2}{3}\lambda - \frac{1}{3} \quad (2.25)$$

$$A_2 = \lambda^3 - 3\lambda^2 + \frac{5}{3}\lambda + \frac{1}{3} \quad (2.26)$$

$$A_3 = 2\lambda^2(1+\lambda) \quad (2.27)$$

A_0 is the original value as shown in eqn. 2.16. The function $f_n(E_e)$ describes the radiative correction to A [Gud06, And04].

The Fermi spectrum is also corrected

$$F(E) = F_0(E) \left(1 + \frac{3E_e - E_0 - 3\mathbf{p}_e \cdot \hat{\mathbf{k}}_\nu}{M} \right) \left(1 + \frac{\alpha\pi}{\beta} \right) \left(1 + \frac{\alpha}{2\pi}\delta \right) \quad (2.28)$$

where $\hat{\mathbf{k}}_\nu$ is the unit vector of neutrino momentum. The three components stand for the corrections from proton recoil, Coulomb force and other radiations [And04].

The three contributions produce the corrections of the correlation coefficients on the order of 10^{-3} [Wil82, GT92]. As predicted in [Ram08], the supersymmetry that beyond Standard Model might have contributions on the order of 10^{-4} to the correlation coefficients. Therefore, to investigate the new physics in the neutron decay, the corrections are necessary to be considered.

2.3 Tests of Standard Model From Neutron Decay

Up to now, the Standard Model is the most successful theory in particle physics. In the past 40 years, it has been excellent in explaining a wide variety of experimental results, also in predicting the existence of many particles. However, in the field of particle physics and cosmology, many properties remain mysterious. Physicists believe the Standard Model is not a complete theory:

- After the unifications of the electromagnetic and the electroweak interactions, physicists are expecting a theory to unify all of the four interactions. In Standard Model, the electroweak and strong interactions are expressed but not unified, moreover the gravity is not incorporated.
- The origin of the left-handness, namely the P-violation in the weak interaction is unclear.
- The origin and the properties of the CP-violation are still open questions. The CP-violation induced by CKM phase angle δ is too weak to result in baryogenesis asymmetry, which might cause the asymmetry between matter and antimatter in the universe.
- Experiments have shown the existence of dark matter and dark energy, which accounts for more than 95% mass-energy in the universe. These cosmological phenomenons are not well explained in Standard Model.

To answer these questions, some extensions of Standard Model are proposed. These extensions aim to explain the open questions by introducing new symmetries, exotic interactions, additional particles or extra dimensions excluded from Standard Model.

In the searching of the new physics beyond Standard Model, the free neutron β-decay provides a clean and advantaged platform. By investigating the observables in neutron decay precisely, the limits of the new physics can be determined. Since there is only one nucleon in the free neutron decay, the process is free of influences from the nuclear and atomic structures. Further, the final state interaction effects, which appears in T-violation quantities, are minimal and can be calculated with high precisions.

In this section, we introduce some theories in the extensions of Standard Model, and the possible tests of the them with free neutron decay investigations. In the frameworks of these

theories, we estimate the limits of the quantities with the observables in neutron decay, by using the method of least square [Kon11]. We fit the quantities to the present values of the observables as listed in table 2.2, also to the expected future values of them with higher accuracies.

As introduced in Section 6 and [Dub08], the coefficient A is expected to be determined by PERC with accuracy

$$\Delta A/A = 3 \times 10^{-4} \tag{2.29}$$

The future projects aSPECT [Kon11], aCORN [Wie09], abBA [abBA07], as well as PERC [Kon12] have plans to measure the coefficients a, B, and C with higher accuracies

$$\Delta B/B = 10^{-3} \quad \Delta a/a = 10^{-3} \quad \Delta C/C = 10^{-3} \tag{2.30}$$

In the future limits estimation, we assume the angular coefficients A, B, C, and a have the relations in the Standard Model. We use the latest measured A from PERKEOII measurement [Mun12] as $A = -0.11996(58)$. With eqn. 2.15 and eqn. 2.14, we calculate the values of other coefficients, and apply the expected errors on them. Hence the angular correlation coefficients in future limits estimations are

$$A = -0.119960(36) \quad B = 0.98700(99) \quad a = -0.10696(11) \quad C = -0.23830(24) \tag{2.31}$$

The neutron life time τ does not change in our estimation. Additionally, we use the value of the average value of the superallowed $0^+ \to 0^+$ nuclear β decays as [HT09]

$$Ft^{0^+\to 0^+} = 3071.81(83)\ \text{s} \tag{2.32}$$

2.3.1 Test of CKM matrix unitarity

In the Standard Model, the strengths of the couplings between up- and down-type quarks in weak interaction are described by the Cabibbo-Kobayashi-Maskawa (CKM) matrix:

$$\begin{pmatrix} d' \\ s' \\ b' \end{pmatrix} = \begin{pmatrix} V_{ud} & V_{us} & V_{ub} \\ V_{cd} & V_{cs} & V_{cb} \\ V_{td} & V_{ts} & V_{tb} \end{pmatrix} \begin{pmatrix} d \\ s \\ b \end{pmatrix} \tag{2.33}$$

The d', s', b' are the weak eigenstates of down-type quarks, which couple with the up-type quarks u, c, t in weak currents. The matrix indicates the weak eigenstates as the admixtures of their mass eigenstates d, s, b. Because of the local gauge invariance and baryon number conservation, the CKM matrix should be a unitary 3×3 matrix.

The content of CKM matrix is not described in Standard Model, but have to be determined from experiments of quark decays. To search for the physics beyond Standard Model, it is of interest to test the unitarity of the CKM matrix. In particular, the deviation of the first row from unity

$$\Delta = 1 - (|V_{ud}|^2 + |V_{us}|^2 + |V_{ub}|^2) \tag{2.34}$$

can be tested.

The elements $|V_{us}|$ and $|V_{ub}|$ can be measured from the decays of K and B mesons. The largest element $|V_{ud}|$ that depends only on the first generation of quarks can be measured most precisely. The most precise results till now indicate the deviation as [PDG12] [4]

$$\Delta = (1 \pm 6) \times 10^{-4} \tag{2.35}$$

In the free neutron decay, the value of $|V_{ud}|$ can be derived by the neutron life time τ_n , the Fermi constant G_F, and the coupling ratio λ [Abe02, Sev06, PDG12]

$$|V_{ud}|^2 = \frac{2\pi^3}{m_e^5 G_F^2 \tau_n (1+3|\lambda|^2) f_n (1+\delta_R)(1+\Delta_R)} = \frac{4908.7(1.9)\ \mathrm{s}}{\tau(1+3|\lambda|^2)} \tag{2.36}$$

where f_n is the phase-space factor [Wil82], δ_R denotes the outer radiative correction [Sir67, Cza04], and Δ_R indicates the inner nucleus-independent radiative corrections [Tow92].

$$f_R = f_n(1+\delta_R) = 1.71385(34) \tag{2.37}$$

Since there is only one nucleon in the n-decay, the determination of $|V_{ud}|$ is free of the corrections of nuclear structures or isospin symmetry-breaking, thus can obtain a clean environment.

With present limits of the A, B, C, a, and τ, additionally with the $Ft^{0^+\to 0^+}$ value and the correction f_R, we have

$$\lambda = -1.2707(28) \quad |V_{ud}| = 0.9769(19) \tag{2.38}$$

Employing present values of $|V_{us}|$=0.2252(9), $|V_{ub}|$=4.15(49)$\times 10^{-3}$ [PDG12], the deviation from unitarity is

$$\Delta = -0.0051(37) \tag{2.39}$$

With future limits, the errors of λ and $|V_{ud}|$ are expected to be

$$\Delta\lambda = 9.4 \times 10^{-5} \quad \Delta|V_{ud}| = 6.1 \times 10^{-4} \tag{2.40}$$

Figure 2.3 shows the estimated present and future limits of $|V_{ud}|$ with λ.

If the CKM matrix does not show a unitary property, it might imply other physics beyond Standard Model, e.g. right-handed current or S, T contributions to the weak interactions [HT05]. Experimentally, the estimation of $|V_{ud}|$ nowadays is limited by the neutron life time τ. To determine the CKM matrix non-unitarity Δ induced by new physics, precise measurements of τ are especially required.

[4] The most precise $|V_{ud}|$ is measured in superallowed nuclear β-decays ($0^+ \to 0^+$ transition), which results in $|V_{ud}|$=0.97425(22).

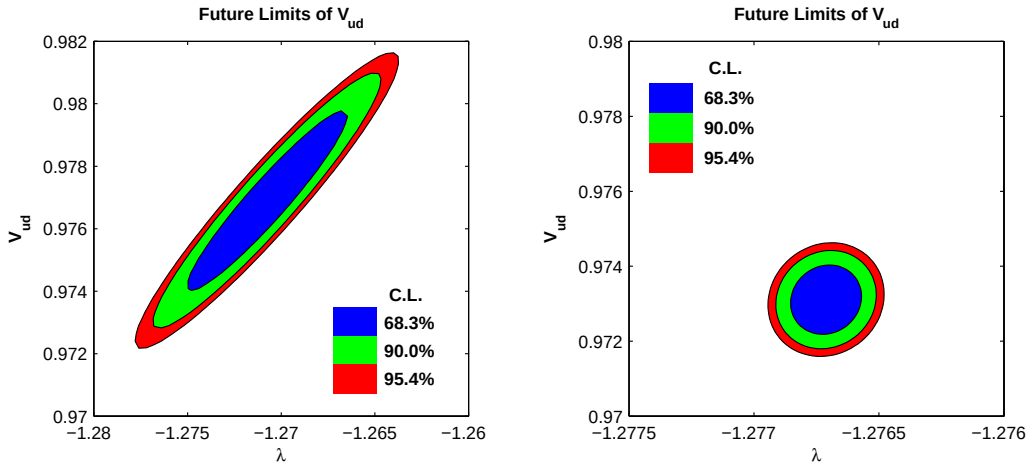

(a) Present Limits **(b)** Future Limits

Figure 2.3: Determination of $|V_{ud}|$ with present and future limits of A, B, C, a, and τ.

2.3.2 Left-right symmetric models

The P-violation in the weak interaction is implied in Standard Model by forcing the left-handed fermions to transform as $SU(2)_L$ doublets, while the right-handed fermions as singlets as shown in eqn. 2.8 and 2.9. However, the reason of the arrangements, namely the origin of the P-violation remains unknown.

In many extensions of Standard Model, the symmetry of left- and right-handness (LR-Symmetry) is proposed to explain the origin of P-violation in weak interaction. It is assumed in these theories, that the LR-Symmetry is conserved at a high energy scale, e.g., in the beginning of the universe, at which time the right-handed boson W_R is also present, and couples to the right-handed particles. When the energy drops below the level of m_{W_R}, the mass of W_R, the symmetry group spontaneously breaks from $SU(2)$ into the left-handed group $SU(2)_L$.

The gauge symmetry group of the simplest LR-Symmetric model is then extended to $SU(2)_R \times SU(2)_L \times U(1)$, in which the left- (right-) handed fermions are in doublets of $SU(2)_L$ ($SU(2)_R$), and in singlets of $SU(2)_R$ ($SU(2)_L$). The coupling of the weak bosons W_L, W_R with the quarks and leptons of the first generation can be given as [Her01]:

$$L_{LR} = \frac{g_L}{\sqrt{2}}(\bar{u}_L \gamma^\mu V^L_{ud} d_L + \bar{\nu}^i_L \gamma_\mu U^L_{ie} e_L) W_L + \frac{g_R}{\sqrt{2}}(\bar{u}_R \gamma^\mu V^R_{ud} d_R + \bar{\nu}^j_R \gamma_\mu U^R_{je} e_R) W_R + h.c. \quad (2.41)$$

g_L and g_R are the $SU(2)_L$ and the $SU(2)_R$ gauge coupling constants, V^L_{ud}, V^R_{ud}, U^L_{ie} and U^R_{je} are the elements of quark and lepton mixing matrices. As shown in eqn. 2.41, there only exist vector currents couplings, and the coupling is invariant under LR-Symmetry.

The weak eigenstates of W_L, W_R bosons in eqn. 2.41 are admixtures of the mass eigenstates W_1, W_2

$$\begin{pmatrix} W_L \\ W_R \end{pmatrix} = \begin{pmatrix} \cos\zeta & \sin\zeta \\ -e^{i\omega}\sin\zeta & e^{i\omega}\cos\zeta \end{pmatrix} \begin{pmatrix} W_1 \\ W_2 \end{pmatrix} \quad (2.42)$$

where ζ is the mixing angle, and ω is a CP-violation phase. In the LR symmetry theories, the mixing of the boson states in eqn. 2.42 is the origin of the P-violation.

In the manifest LR-Symmetric model [Beg77], it is simplified that, the phase angle $\omega = 0$, the coupling strengths for left- and right-handed currents are equal g_L=g_R, the CKM matrix elements V^L_{ud}=V^R_{ud}, and the neutrino is Dirac particle that has three mass eigenstates. There are two free parameters left: the mixing angle ζ and the mass ratio of W_1 and W_2 bosons δ

$$\delta = \left(\frac{m_{W_1}}{m_{W_2}}\right)^2 \tag{2.43}$$

which equal zero in Standard Model: $\zeta, \delta \to 0$.

From eqn. 2.41, the four-fermion interaction of β-decay in the manifest LR-Symmetry is described as [Beg77, Sch07d]:

$$L_{LR} = -\frac{G' V_{ud}}{\sqrt{2}}\left[\bar{u}_p\gamma^\mu u_n(C^V_L J^L_{lep} + C^V_R J^R_{lep}) + \lambda\bar{u}_p\gamma^\mu\gamma_5 u_n(C^A_L J^L_{lep} + C^A_R J^R_{lep})\right] \tag{2.44}$$

with G' the coupling constant, which is transformed by the matrix in eqn. 2.42

$$\frac{G'}{\sqrt{2}} = \frac{g^2}{8m_1^2}(\cos\zeta - \sin\zeta)^2 + \frac{g^2}{8m_2^2}(\cos\zeta + \sin\zeta)^2 \tag{2.45}$$

J^L_{lep} and J^R_{lep} are the left- and right-handed leptonic currents:

$$J^L_{lep} = \bar{u}_e\gamma^\mu(1-\gamma_5)u_\nu, \quad J^R_{lep} = \bar{u}_e\gamma^\mu(1+\gamma_5)u_\nu \tag{2.46}$$

As shown in eqn. 2.44, the hadronic currents remain the same as in $V-A$ theory, whereas the leptonic currents become admixtures of the left- and the right-handed contributions. The ratios of right- and left-handed lepton currents, for Vector and Axial-vector couplings are respectively:

$$r_V = \frac{C^V_R}{C^V_L} = \frac{\delta(1+\tan\zeta) - \tan\zeta(1-\tan\zeta)}{\delta\tan\zeta(1+\tan\zeta) + (1-\tan\zeta)} \approx \frac{\delta - \tan\zeta}{1-\tan\zeta} \approx \delta - \zeta \tag{2.47}$$

$$r_A = \frac{C^A_R}{C^A_L} = \frac{\tan\zeta(1+\tan\zeta) + \delta(1-\tan\zeta)}{(1+\tan\zeta) - \delta\tan\zeta(1-\tan\zeta)} \approx \frac{\delta + \tan\zeta}{1+\tan\zeta} \approx \delta + \zeta \tag{2.48}$$

when assuming δ, ζ are small. The angular correlation coefficients in a free neutron decay become [Abe00]:

$$A = -2\frac{\lambda^2(1+r_V^2 - r_A^2) + \lambda(1+r_V^2 - r_V r_A)}{(1+r_V^2) + 3\lambda^2(1+r_A^2)} \tag{2.49}$$

$$B = 2\frac{\lambda^2(1+r_V^2 - r_A^2) - \lambda^(1+r_V^2 - r_V r_A)}{(1+r_V^2) + 3\lambda^2(1+r_A^2)} \tag{2.50}$$

$$a = \frac{(1+r_V^2) - \lambda^2(1+r_A^2)}{(1+r_V^2) + 3\lambda^2(1+r_A^2)} \tag{2.51}$$

With precise measurements of angular correlation coefficients, we are able to determine the limits on the right-handed boson mass δ and the mixing angle ζ. We fit λ, δ, and ζ to the parameters τ, A, B, C, a, and use the $Ft^{0^+\to 0^+}$ value and the correction f_R. The fitted values with present limits are

$$\lambda = -1.2896(84) \quad \zeta = -0.124(34) \quad \delta = 0.050(16) \tag{2.52}$$

The present measured mass of left-handed boson W_1 is [PDG12]

$$m_{W_1} = 80.385(15)\ \text{GeV} \tag{2.53}$$

with δ, the mass of W_2 boson is then

$$m_{W_2} = 355.95\ \text{GeV} \tag{2.54}$$

Figure 2.4 shows the estimated present and future limits of δ and ζ in the manifest left-right symmetric model.

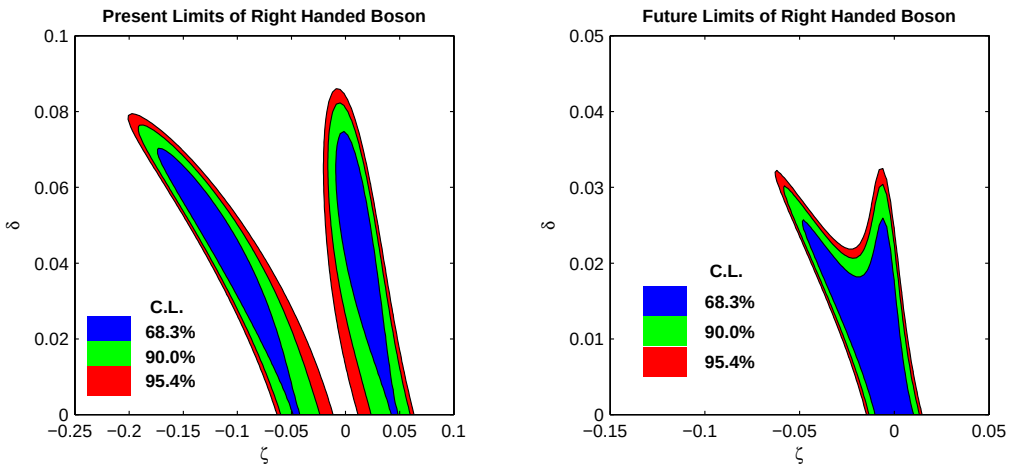

(a) Present Limits **(b)** Future Limits

Figure 2.4: Determination of δ and ζ in the manifest left-right symmetric model with present and future limits of A, B, C, a, and τ.

In the estimation with future limits, the δ approaches 0. In 1σ deviation (68.3% C.L.), we have

$$\delta < 0.026 \tag{2.55}$$

which results in

$$m_{W_2} > 498.52\ \text{GeV} \tag{2.56}$$

2.3.3 Scalar and tensor contributions

As shown in Appendix A, the $V-A$ theory is based on the approximation of maximal P-violation. Beyond this limit, we can also consider the contributions of the scaler S and

the tensor T interactions in table A.1. A general form of the Hamiltonian density of four fermion interaction, involving left- and right-handed neutrino states ν_e^L, ν_e^R, can be expressed as [LY56]: [5]

$$H(x) = \frac{G_F V_{ud}}{\sqrt{2}} \Big\{ [\bar{u}_p \gamma_\mu u_n][\bar{u}_e \gamma^\mu (C_V + \overline{C}_V \gamma_5) u_\nu] + [\bar{u}_p \gamma_\mu \gamma_5 u_n][\bar{u}_e \gamma^\mu \gamma_5 (C_A + \overline{C}_A \gamma_5) u_\nu] + [\bar{u}_p u_n][\bar{u}_e (C_S + \overline{C}_S \gamma_5) u_\nu] + \frac{1}{2}[\bar{u}_p \sigma^{\mu\nu} u_n][\bar{u}_e \sigma_{\mu\nu} (C_T + \overline{C}_T \gamma_5) u_\nu] \Big\} + h.c. \tag{2.57}$$

The four terms in the equ. 2.57 denote the contributions from V, A, S, and T. The contribution from pseudo scalar P is neglected in non-relativistic limit, as stated in Section A.2. The $C_{V,A,S,T}$ and $\overline{C}_{V,A,S,T}$ are coupling constants for V, A, S, T currents, and have contributions from left- and right-handed leptonic currents [Her01]

$$C_i = L_i + R_i, \quad \overline{C}_i = -L_i + R_i, \quad i = V, A, S, T \tag{2.58}$$

If the time reversal conservation is violated, the coupling constants are complex quantities.

In the frame of Standard Model, the coupling constants are [6]

$$C_V = -\overline{C}_V = 1, \quad \overline{C}_A = -C_A = \lambda \ (\lambda < 0), \quad C_S = \overline{C}_S = C_T = \overline{C}_T = 0 \tag{2.60}$$

and we only have the left-handed $V-A$ leptonic current

$$L_V = 1, \quad L_A = -\lambda, \quad L_{S,T} = 0, \quad R_{V,A,S,T} = 0 \tag{2.61}$$

With eqn. 2.57, the angular correlation coefficients can be derived including $C_{V,A,S,T}$ and $\overline{C}_{V,A,S,T}$, as listed in Section A.5. Considering the left- and right-handed leptonic currents in eqn. 2.58, the coefficients can be written as

[5] Because of different conventions of γ matrices, the terms in the equation has dissimilarities from some literatures. In particular, the γ_5 has an opposite signs in the old convention, e.g. in [LY56, Jac57, Sev06]. In this dissertation, the convention of γ matrices is same as [BD64, Her01]. The convention difference also leads the $\overline{C}_{V,S,T}$ and C_A to opposite values.

[6] Please note the relation between C_A and g_A. If we use the conditions $C_V = -\overline{C}_V$, $C_A = -\overline{C}_A$, $C_{S,T} = -\overline{C}_{S,T} = 0$, and $\gamma_5 \gamma_5 = 1$, eqn. 2.57 can be transformed as

$$H(x) = \frac{G_F}{\sqrt{2}} V_{ud} [\bar{u}_p \gamma^\mu (C_V + \overline{C}_A \gamma_5) u_n][\bar{u}_e \gamma_\mu (1 - \gamma_5) u_\nu] + h.c. \tag{2.59}$$

Compare with eqn. 2.4, we have $\overline{C}_A = g_A$, and the coupling ratio in eqn. 2.15 is actually $\lambda = \overline{C}_A / C_V$. Therefore, the L_A and R_A in this dissertation is opposite to that in [Glu95, Kon11].

$$\xi = 2(|L_V|^2 + |L_S|^2 + 3|L_A|^2 + 3|L_T|^2 + |R_V|^2 + |R_S|^2 + 3|R_A|^2 + 3|R_T|^2) \quad (2.62)$$
$$A\xi = 4Re(-|L_A|^2 + L_V L_A^* + |L_T|^2 + L_S L_T^* + |R_A|^2 - R_V R_A^* - |R_T|^2 - R_S R_T^*) \quad (2.63)$$
$$a\xi = 2(|L_V|^2 - |L_A|^2 - |L_S|^2 + |L_T|^2 + |R_V|^2 - |R_A|^2 - |R_S|^2 + |R_T|^2) \quad (2.64)$$
$$B = B_0 + b_\nu \frac{m_e}{E_e} \quad (2.65)$$
$$B_0\xi = 4Re(|L_A|^2 + L_V L_A^* - L_S L_T^* + |L_T|^2 - |R_A|^2 - R_V R_A^* + R_S R_T^* - |R_T|^2) \quad (2.66)$$
$$b_\nu\xi = 4Re(L_S L_A^* - L_V L_T^* - 2L_T L_A^* - R_S R_A^* + R_V R_T^* + 2R_T R_A^*) \quad (2.67)$$
$$b_F\xi = 4Re(L_S L_V^* - 3L_T L_A^* + R_S R_V^* - 3R_T R_A^*) \quad (2.68)$$

And the measured angular correlation coefficients have the contributions from the Fierz interference term b_F

$$A_{eff} = \frac{A}{1 + b_F \frac{m_e}{E_e}} \quad B_{eff} = \frac{B_0 + b_\nu \frac{m_e}{E_e}}{1 + b_F \frac{m_e}{E_e}} \quad C_{eff} = \frac{-x_C(A + B_0) - x'_C b_\nu}{1 + b_F \frac{m_e}{E_e}} \quad a_{eff} = \frac{a}{1 + b_F \frac{m_e}{E_e}} \quad (2.69)$$

with the kinematical factor $x'_C = 0.1978$ [Glu95]. In a precise measurement, the Fierz interference term b_F can be determined from the energy spectrum $F(E)$ of electrons from unpolarized neutrons, which have the average spin state as zero. We integrate the decay rate in eqn. 2.10 over the momentum of $\bar{\nu}_e$, the terms related to $\langle \boldsymbol{\sigma}_n \rangle$ and $\mathbf{p}_\nu$ vanish. The Fierz term b_F can be determined from compare of the theoretic spectrum $F(E)$ and measured spectrum $F_{eff}(E)$ of the electrons

$$F_{eff}(E_e) = F(E_e)\left(1 + b_F \frac{m_e}{E_e}\right) \quad (2.70)$$

With the present and future limits of the observables, we estimate the left- and right-handed S and T contributions separately. We assume the left-handed V, A coupling as $L_V = 1$, $L_A = -\lambda$, and investigate the ratios L_S/L_V, L_T/L_A, R_S/L_V, and R_T/L_A.

As for the left-handed S, T contributions, the λ, the ratios L_S/L_V and L_T/L_A are fitted to A, B, C, and a with present limits

$$\lambda = -1.2731(20) \quad L_S/L_V = -0.063(26) \quad L_T/L_A = 0.0174(47) \quad (2.71)$$

With future limits, we have

$$\Delta\lambda = 2.6 \times 10^{-4} \quad \Delta(L_S/L_V) = 8.6 \times 10^{-3} \quad \Delta(L_T/L_A) = 1.9 \times 10^{-3} \quad (2.72)$$

Figure 2.5 shows the estimated present and future limits of the left-handed S and T contributions.

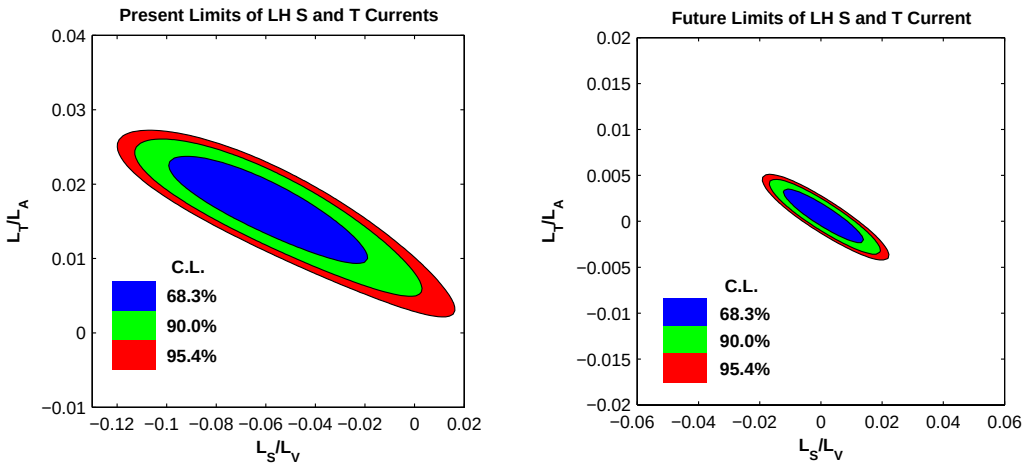

(a) Present Limits **(b)** Future Limits

Figure 2.5: Determination of left-handed S and T contributions with present and future limits of A, B, C, and a.

For right-handed S, T contributions, the free parameters λ, R_S/L_V, and R_T/L_A are fitted to τ, A, B, C, a, and the $Ft^{0^+\to 0^+}$ value and the f_R are referred. With present limits of the observables, we have

$$\lambda = -1.2738(62) \quad R_S/L_V = 0.049(77) \quad R_T/L_A = 0.059(22) \tag{2.73}$$

With future limits, the values are expected as

$$\Delta\lambda = 4.3 \times 10^{-4} \quad \Delta(R_S/L_V) = 1.2 \times 10^{-2} \quad \Delta(R_T/L_A) = 4.4 \times 10^{-3} \tag{2.74}$$

Figure 2.6 shows the estimated present and future limits of the right-handed S and T contributions.

2.3.4 T-violation and transverse polarization of electrons

In Standard Model, the CP-violation, equivalently the T-violation due to CPT conservation theorem, is induced by the phase δ in CKM matrix. However, the CP-violation induced by δ is not sufficient to cause remarkable baryogenesis asymmetry, thus the asymmetry between matter and antimatter in the universe [RT99]. Therefore, it is of considerable interests to search the T-violation that from other sources beyond Standard Model.

In the neutron decay, the CKM phase δ gives a extremely small contribution of $\leqslant 10^{-12}$ [Her01], hence the neutron decay provides a clean environment to search the T-violation from new sources. One of the possible tests is to investigate the polarization of the emitted electrons in the free neutron decay.

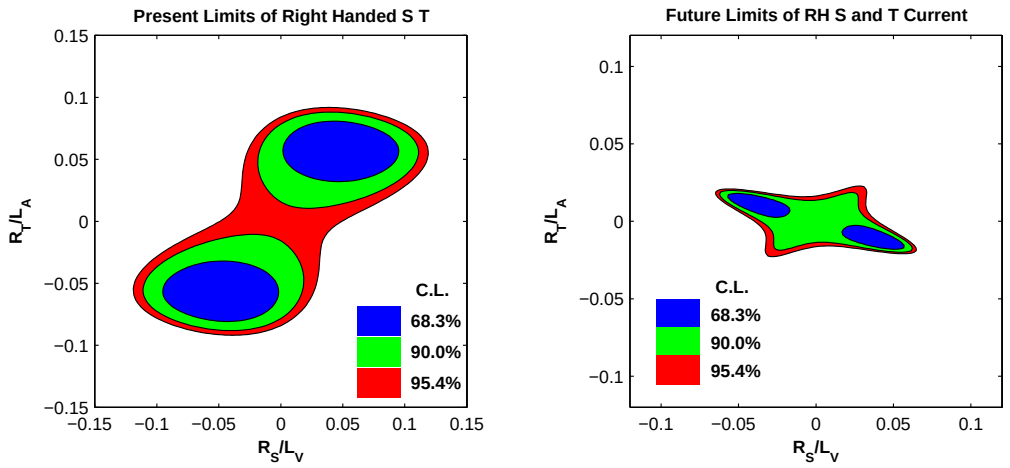

(a) Present Limits **(b)** Future Limits

Figure 2.6: Determination of right-handed S and T contributions with present and future limits of τ, A, B, C, and a.

When we consider the distribution of the electron spin states in the neutron decay, another terms can be included in eqn. 2.10 [Jac57]

$$W \propto 1 + R \cdot \langle \boldsymbol{\sigma}_n \rangle \cdot \frac{\mathbf{p}_e \times \langle \mathbf{J}_e \rangle}{E_e} + \cdots \tag{2.75}$$

where $\langle \mathbf{J}_e \rangle$ is the unit vector of the electron spin state.

The coefficient R is related to three vectors (and axial vectors) in the neutron decay: neutron spin $\langle \boldsymbol{\sigma}_n \rangle$, electron spin $\langle \mathbf{J}_e \rangle$ and electron momentum $\mathbf{p}_e$. All the three vectors change signs under time reversal. Hence the scalar triple product of the three vectors is invariant under spatial rotations, but non-invariant under time reversal, also non-invariant under parity transform. Therefore, the non zero value of R detection (excluding FSI) would indicate the T-violation in neutron decay.

Assume the C_V=$-\overline{C}_V$=1, $\overline{C}_A$=$-C_A$=g_A are real quantities, and consider the S, T contributions to the first order, the R are expressed as [Jac57]

$$R = R_T + R_{FSI} = \frac{\lambda}{1+3\lambda^2} Im(C_S - \overline{C}_S) + \frac{2\lambda+1}{1+3\lambda^2} Im(C_T - \overline{C}_T) - \frac{\alpha m_e}{p_e} A \tag{2.76}$$

The term proportional to fine structure constant α=1/137 is caused by the electromagnetic Final State Interaction (FSI). The parameter R_T is the quantity that indicates scalar and tensor type T-violating interactions.

R can be determined from the measurement of electron transverse polarisations. Assuming neutron spin state $\langle \boldsymbol{\sigma}_n \rangle$ is along z-axis, electron is emitted in x-z plane, the polarization of electron in the y-direction are expressed as [Jac57]

$$P_{trans.} = R \frac{\langle \boldsymbol{\sigma}_n \rangle \times \mathbf{p}_e}{E_e + b_F m_e} \tag{2.77}$$

Experimentally, the polarization of electron can be measured with Mott scattering method. Moreover, by applying polarized neutrons and tracking the electron trajectories, e.g., with multi-wire proportional chamber, R can be determined from the asymmetry of electron transverse polarization [Ban06, Koz09].

2.4 Observables in Free Neutron Decay and Deduced Quantities

As a summary, figure 2.7 lists the observables in free neutron decay, and the physical quantities which can be exported from the them, including the quantities in and beyond the Standard Model.

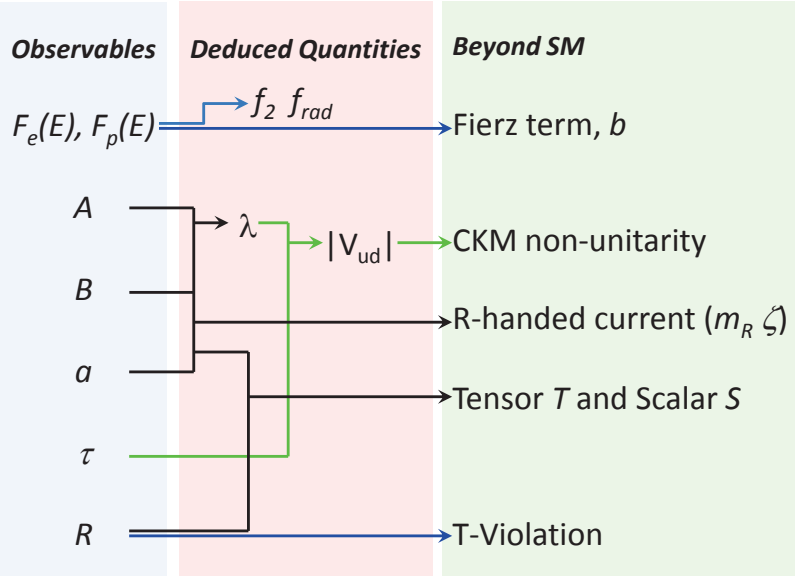

Figure 2.7: Observables in neutron decay and the possible derived quantities, including that in and beyond Standard Model.

Chapter 3

Introduction to PERKEOIII Experiment

The PERKEOIII instrument is the third generation of neutron decay-product spectrometer developed by Physics Institute of University of Heidelberg in 2006 [Mae09]. As a successor of previous PERKEO [Bop86] and PERKEOII/IIB [Abe97, Rei00, Sch07, Sch08, Mun12] instruments, PERKEOIII aims to obtain the statistics increased by up to two orders of magnitude, and perform more precise measurements of the electron energy spectra in the free neutron decays.

From 2008-11 to 2009-08, we performed an experiment with PERKEOIII at the beam facility PF1b of Institute Laue Langevin (ILL) in Grenoble of France. The motivation of the experiment was to measure the β-asymmetry in the free neutron decay, i.e., the electrons angular correlation coefficient A. Further with the value of A, we derive the coupling ratio λ and the CKM matrix element V_{ud} with neutron life time τ as introduced in Chapter 2. Part of the experiment and the results have been introduced and discussed in [Mes11].

The author of this dissertation participated in the installation of PERKEOIII, the measurements, and the preliminary analyses of the data (Chapter 5), in particular worked on the studies of neutron properties (Section 4.1) and the magnetic mirror effect (Section 4.4).

In this chapter, we provide an introduction to the principles of PERKEOIII and the experiment performed at ILL. To study the characters of the neutrons and the neutron beam line, we used the Monte Carlo simulation program *McStas* [McS] to calculate the neutron behaviour in PERKEOIII. For the magnetic field and electron trajectories studies, we used the program *CST Studio* [Cst] for the simulations. Some of the simulated results are compared with the measured values.

3.1 Methods of β-Asymmetry Measurement

As shown in eqn. 2.10, the quantity A governs the probability of the emitted electrons distributions relative to the neutron spin state $\langle \boldsymbol{\sigma}_n \rangle$. We integrate the decay rate over the neutrino momentum $\mathbf{p}_{\bar{\nu}}$, the terms proportional to coefficients a and B vanish. If the Fierz term is not considered, the normalized probability of electron emission has the distribution as:

$$W(E_e, \theta) = \frac{1}{2} F(E_e) \left[1 + A\beta(E) \cos\theta\right] \tag{3.1}$$

where $F(E_e)$ is the Fermi spectrum of electrons, θ is the angle between electron momentum $\mathbf{p}_e$ and neutron spin state $\langle \boldsymbol{\sigma}_n \rangle$, and $\beta(E) = v_e/c$ is the relative velocity of the electron. The electron emission probability distribution is plotted in figure 3.1.

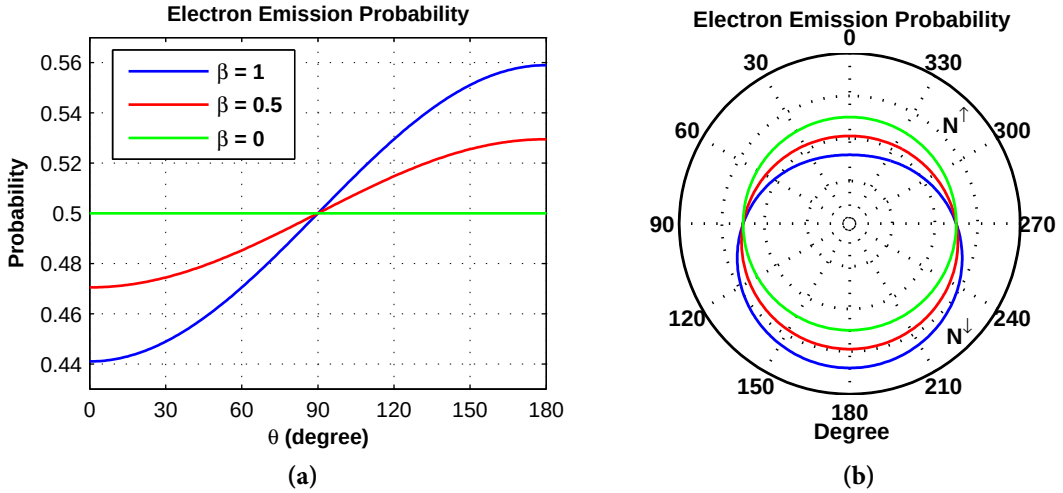

Figure 3.1: (a) Electron emission probabilities versus the emission angle θ relative to $\langle \boldsymbol{\sigma}_n \rangle$, for different velocities β. **(b)** Sketch of the probability in polar coordinates. We integrate the electrons over the two halves of the hemisphere, and obtain the event number $N^{\uparrow}$ and $N^{\downarrow}$ according to the neutron polarization state $\langle \boldsymbol{\sigma}_n \rangle$, which lies in the direction of 0^{o}.

From eqn. 3.1, we integrate the number of emitted electrons over the two half spheres relative to neutron spin $\langle \boldsymbol{\sigma}_n \rangle$, as sketched in figure 3.1 **(b)**, the integrated event rates are

$$N^{\uparrow}(E) = N(E)F(E)\int_0^{\frac{\pi}{2}} W(\theta)\sin\theta\,\mathrm{d}\theta = \frac{1}{2}N(E)F(E)\left[1+\frac{1}{2}A\beta(E)\right] \tag{3.2}$$

$$N^{\downarrow}(E) = N(E)F(E)\int_{\frac{\pi}{2}}^{\pi} W(\theta)\sin\theta\,\mathrm{d}\theta = \frac{1}{2}N(E)F(E)\left[1-\frac{1}{2}A\beta(E)\right] \tag{3.3}$$

with $N(E)$ the total events. Define the experimental asymmetry coefficient A_{exp} as the relative difference of event rates:

$$A_{exp}(E) \equiv \frac{N^{\uparrow}(E)-N^{\downarrow}(E)}{N^{\uparrow}(E)+N^{\downarrow}(E)} = \frac{1}{2}A\beta(E)P \tag{3.4}$$

with P the polarization of the neutrons, when we consider the practical experiment.

It is shown that the relative event rates difference is proportional to A and $\beta(E)$. In PERKEOIII experiment, the electron energy spectra of $N^{\uparrow}(E)$ and $N^{\downarrow}(E)$ are direct observables. With the spectra, the A_{exp} and A are evaluated in further data analyses.

3.2 Principles of PERKEOIII

The PERKEOIII system is mainly composed by four parts: the *neutron beam line*, the *decay volume vessel*, and two *detector vessels*. The geometry and the principles of the PERKEOIII experiment are sketched in Figure 3.2.

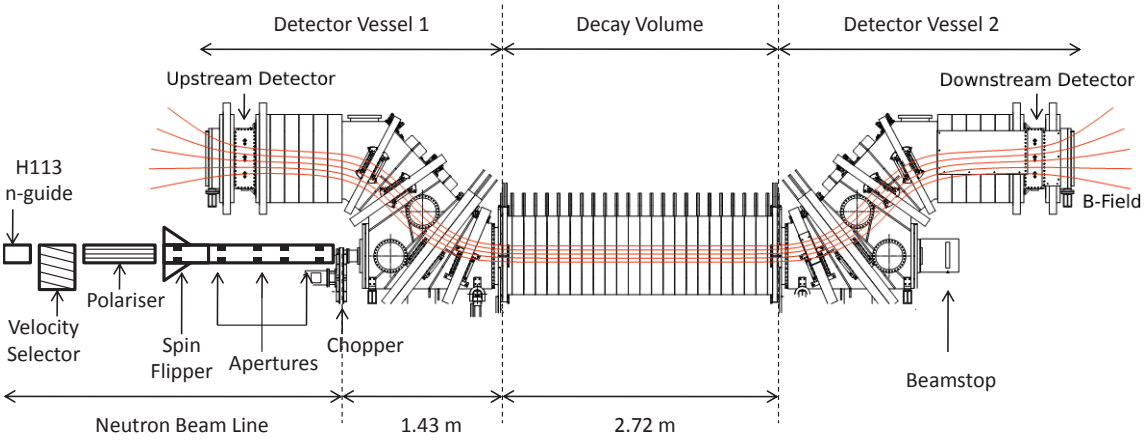

Figure 3.2: Sketch of the geometry and the principles of PERKEOIII experiment. Red curves denote the magnetic lines.

In the experiment, we introduce a beam of cold neutrons from the ILL reactor as the decay source. The neutrons are transported by the H113 guide from the reactor to the PERKEOIII beam line. The elements on the beam line modify the neutron beam (n-beam), and further transport it to the decay volume. During the propagation in the decay volume, part of the neutrons decay into electrons e^-, protons p^+ and electron anti-neutrinos $\bar{\nu}_e$.

To detect the decay electrons, we generate a curved magnetic field in the instrument. The charged electrons from the decay volume spiral along the magnet lines, and are guided to the detectors at upstream and downstream sites. The rest neutrons that have zero charge are not affected by the field. They keep propagating until the end of instrument, where the neutrons are absorbed by the neutron beamstop, or their polarization is measured.

The magnetic field is one of the most important components in the experiment. Besides guiding the electrons, it has additional necessary functions:

- *Keeping the spin state $\langle \boldsymbol{\sigma}_n \rangle$ of neutrons.*

  In the magnetic field, the spin eigenstates $\langle \boldsymbol{\sigma}_n \rangle$ of incoming neutrons are arranged parallel or anti-parallel to the field. With the *neutron polariser* and the *RF spin flipper* on the beam line, we are able to switch $\langle \boldsymbol{\sigma}_n \rangle$ along the $\mathbf{B}$ direction or the reverse. The emission angle θ in eqn. 3.1 is then the angle between the $\mathbf{B}$ and $\mathbf{p}_e$, or its supplementary angle.

- *Integrating electrons over the halves of hemisphere.*

Because of the helical motion, the electrons that have the same sign of $\mathbf{p}\cdot\mathbf{B}$ will spiral along the same direction then reach the same detector. Hence the magnetic field automatically integrates the electrons emission angles over the halves of hemisphere. The spectra $N^{\uparrow}(E)$ and $N^{\downarrow}(E)$ can be directly measured.

- *Defining electron pitch angle range.*

  The pitch angle of electron helical motion, i.e. the angle between **B** and **p**, is dependent on the magnetic field strengths as discussed in Section B.3. The specified field distribution defines the electron pitch angles, then defines the related systematic effects, e.g. backscattering and magnetic mirror effects.

The magnetic field strength inside PERKEOIII is smoothly decreased from decay volume to detectors, the electrons can be adiabatically transported without distortions on their angular distributions.

In the experiment, the spin flipper alternates the neutron spin states every 10 s, the spectra $N^{\uparrow}(E)$ and $N^{\downarrow}(E)$ are measured by each of the detectors.

3.3 Neutron Beam Line and Modification Elements

In the PERKEOIII system, the neutron beam line and the elements on it are used to transport and modify the incoming cold n-beam from the reactor.

During the 2008-2009 beam time of ILL, we used pulsed neutron beam in the measurement. The pulsed n-beam mode can bring beneficial effects on experiment systematics, e.g. background suppression and time structure studies, but reduces the statistics by factor of about 40. In the mean time, the spatial and the temporal properties of the n-beam become important in the measurements and data analyses. Therefore, the neutron beam line is required to supply a bunch of well defined, chromatic, pulsed n-beam in the experiment.

The modification elements on the neutron beam line are sketched in figure 3.2. Since the velocity selector and supermirror polariser on the beam line absorb a lot of neutrons and generate much γ background, they are placed inside the casemate, which is shielded with concrete and Pb walls. Inside the beam line tube, Lithium rubber and Boron glass are attached on the inner wall to absorb scattered neutrons.

3.3.1 Neutron guide H113

The neutrons from ILL reactor are transported by the neutron guide (n-guide) H113 to PERKEOIII beam line.

H113 is the first ballistic supermirror n-guide produced and assembled by ILL in 2000 [Hae02], and is used for the transportation of cold neutrons (5×10^{-5} eV to 0.025 eV) from

the ILL reactor to the PF1b user facility. With specified curvatures and the $m = 2$ supermirror coating on the inner walls, the 72 m long H113 n-guide can export cold neutrons with the capture flux of $\Phi_c = 2\times10^{10}$ cm^{-2}s^{-1}.

Neutron spectrum from H113.

The spectrum and divergence of the n-beam from H113 were measured in 2006 [Abe06]. Figure 3.3 **(a)** shows the measured *Capture Intensity* of the n-beam from H113 guide.

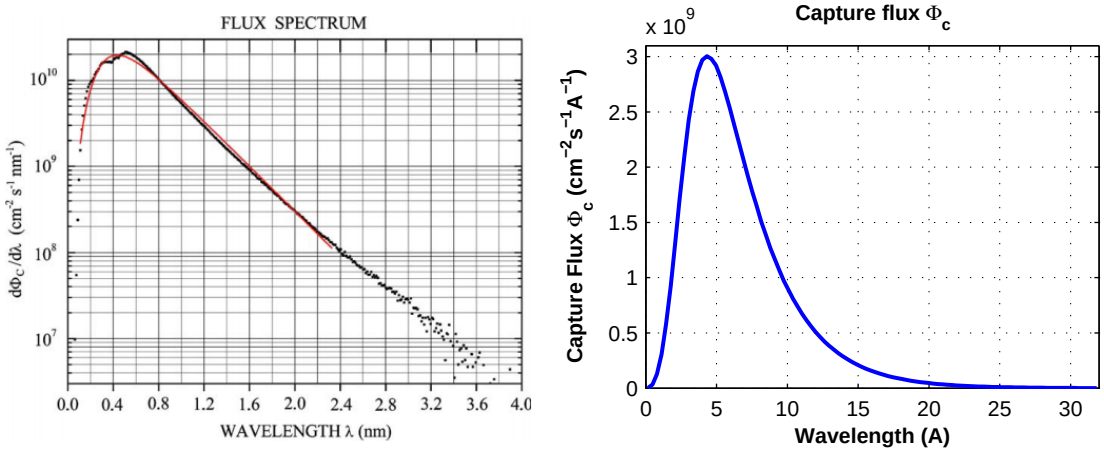

(a) **(b)**

Figure 3.3: (a) The measured capture intensity of the output neutrons from H113 n-guide, with a total capture flux as 1.35×10^{10} cm^{-2}s^{-1}. Figure is from [Abe06]. **(b)** The simulated capture spectrum according to the data from the measurement. The total capture flux is increased to 2×10^{10} cm^{-2}s^{-1}.

The capture intensity (thermal equivalent spectrum) is defined as

$$\frac{\partial\Phi_c}{\partial\lambda} = \frac{\lambda}{\lambda_0}\frac{\partial\Phi}{\partial\lambda} \tag{3.5}$$

which is proportional to the neutron reaction rates in thin detectors. $\lambda_0 = 0.18$ nm is the most probable wavelength of the Maxwellian thermal spectrum of neutrons with 300 K temperature, corresponding to the velocity $v_0 = 2200$ m/s.

In the simulation, we used the neutron source with the same spectrum distribution as the measurement, but with Φ_c increased to 2×10^{10} cm^{-2}s^{-1}, which results the real neutron flux as $\Phi = 7.7\times10^{9}$ cm^{-2}s^{-1}. Figure 3.3 **(b)** plots the assumed neutron spectrum in simulations.

Supermirror and neutron divergence.

The neutron supermirror is a kind of film with multilayers of neutron scattering material. A typical supermirror consists of 100 double layers of Ni/Ti with various thickness, which can reflect the glancing neutrons due to Bragg continuous reflection [Tur67, HM89]. The

neutron reflectivity is a function of the supermirror properties and the momentum transfer $Q = |\mathbf{k}_i - \mathbf{k}_f|$ in the collision, as sketched in figure 3.4 **(a)**.

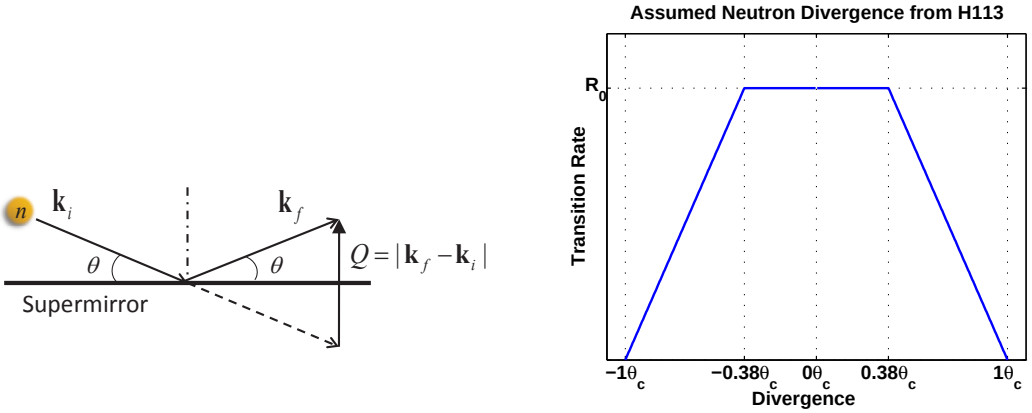

(a) **(b)**

Figure 3.4: (**a**) A sketch of the reflection process of the supermirror. (**b**) The assumed divergence distribution of neutron from H113 in simulation.

An empirical formula of the reflectivity can be expressed as [Cla97]

$$R = \begin{cases} R_0 & Q \leqslant Q_c \\ \frac{1}{2}R_0 \left(1 - \tanh \frac{Q - mQ_c}{W}\right)[1 - \alpha(Q - Q_c)] & Q > Q_c \end{cases} \tag{3.6}$$

where $Q_c = 0.0217$ Å^{-1} is the critical scattering vector for mono Ni layer. When $Q \leqslant Q_c$, the reflectivity keeps as constant R_0. In case of $Q > Q_c$, the reflectivity decreases linearly with a slope of α, and drops to zero at mQ_c. Figure 3.5 plots the neutron reflectivity versus momentum transfer according to eqn. 3.6.

The critical reflection angle θ_c of the incident neutron is then proportional to it's wavelength λ and the value of m

$$\begin{aligned} m \cdot Q_c &= |\mathbf{k}_f - \mathbf{k}_i| = 2k \sin\theta = \frac{4\pi}{\lambda} \sin\theta \approx \frac{4\pi}{\lambda}\theta_c \\ \theta_c(\text{mrad}) &= \frac{Q_c}{4\pi} m\lambda = 1.73 \cdot m\,\lambda(\text{Å}) \end{aligned} \tag{3.7}$$

As stated in [Abe06], the effective m of the long H113 guide is less than 2, since the neutrons with $Q > Q_c$ are considerably absorbed due to many times of collisions. Additionally, we should note, due to the curve structure of H113 guide, the neutrons with $\theta \leqslant 1.73\lambda$ will not have a constant transmission rate. In order to fit the measured neutron divergence in [Abe06] and the n-beam cross-section profile (Section 4.1.1), we assume effective $m = 1.32$, which results in $\theta_c = 2.28\lambda$. The neutrons are uniformly distributed in $-0.38\theta_c < \theta < 0.38\theta_c$ range of divergence angle, and linearly decrease to zero at θ_c, as sketched in figure 3.4 **(b)**. The measured and simulated divergence distributions of the total n-beam are shown in figure 3.6 [1].

[1] Because of the H113 guide curvatures, the neutron divergence distribution in horizontal direction is not

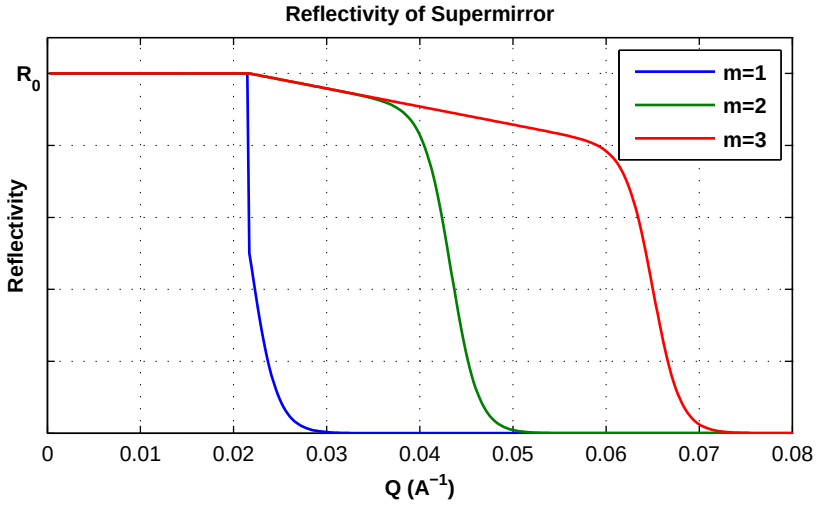

Figure 3.5: Examples of the supermirror reflectivities with different m values.

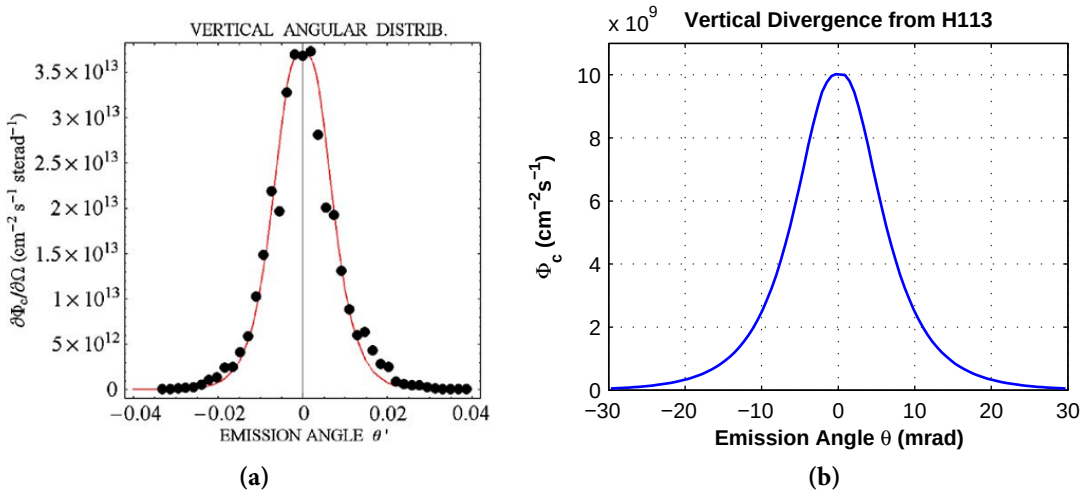

(a) **(b)**

Figure 3.6: **(a)** The measured neutron capture flux versus the neutron divergence in vertical direction [Abe06]. **(b)** The simulated neutron (capture) divergence distribution.

3.3.2 Rotating neutron velocity selector

As shown in figure 3.3, the wavelengths λ, i.e. the velocities of output neutrons from H113 have a wide distribution. The neutron velocity differences will extend the length of the neutron pulse (n-pulse) during its propagation in the decay volume, hence decrease the measurement efficiency (Section 5.2). To limit the λ distribution, we applied a rotating neutron velocity selector after the H113 n-guide.

The velocity selector consists of a rotary turbine, which has helical neutron absorber blades on it, as shown in figure 3.7.

symmetric. In simulations, we do not consider this effect.

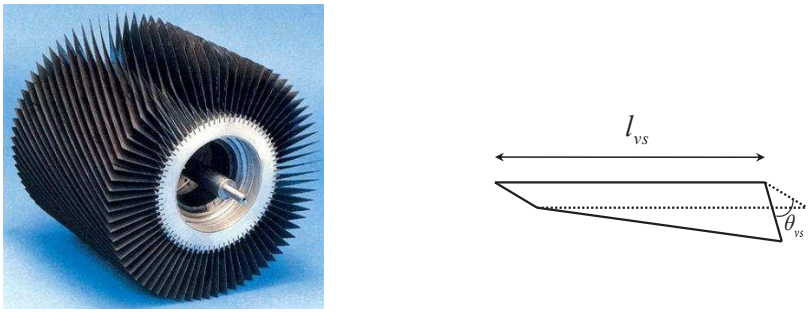

(a) **(b)**

Figure 3.7: (a) Picture of the turbine in velocity selector, and **(b)** a sketch of the selector blade. The photo is from [Dai].

By rotating the turbine, the selector allows the neutrons with the velocities around a nominal value to transmit. The nominal velocity is dependent on the blade structure

$$v_0 = \omega \cdot \frac{l_{vs}}{\theta_{vs}} \tag{3.8}$$

where ω, l_{vs} and θ_{vs} are the rotary angular velocity, the length of the turbine and twist angle of blades. Practically, the divergence distribution of the input neutrons widens the spectrum of output neutrons. Figure 3.8 shows the simulated spectra of the output neutrons with different nominal velocities.

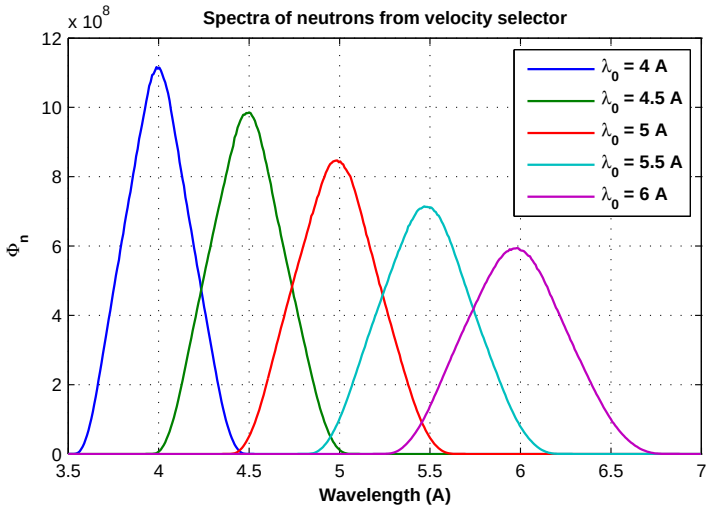

Figure 3.8: The simulated spectrum of output neutrons from velocity selector, with the nominal λ from 4 Å to 6 Å. The input n-beam has the spectrum and divergence as figure 3.3 and figure 3.4.

Because of the turbine structure, the selector also defines the divergence distribution of the output neutrons. Figure 3.9 plots the simulated divergence distributions of the output neutrons from the velocity selector.

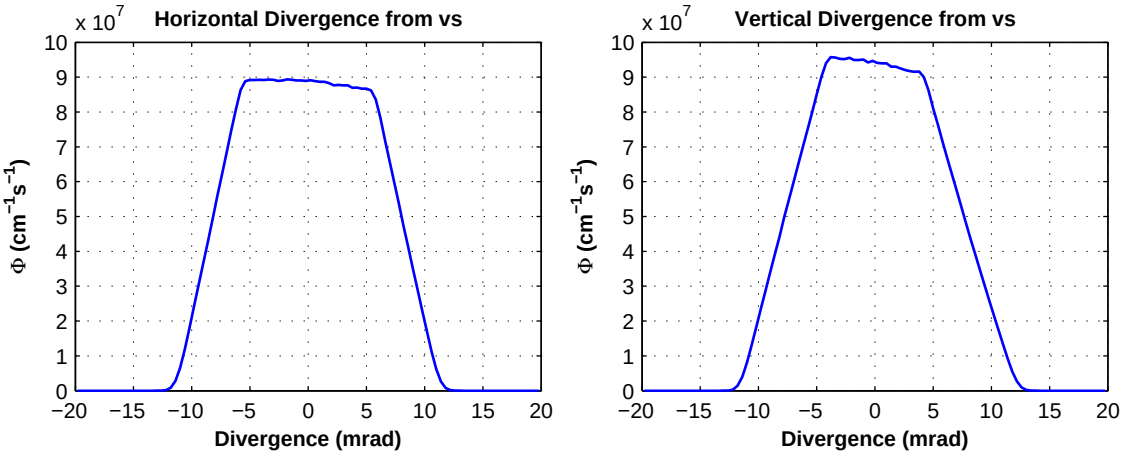

(a) Horizontal direction **(b)** Vertical direction

Figure 3.9: Simulated divergence distribution of output neutrons from velocity selector along horizontal and vertical directions.

The geometry and industrial parameters of the velocity selector are given in [Dai]. In the PERKEOIII experiment, we chose a nominal wavelength as 5 Å, corresponding to the selector rotation speed ω as 25470 rpm.

3.3.3 Supermirror neutron polariser

The polarization of a incident n-beam P directly affects the measured $N^{\uparrow}(E)$ and $N^{\downarrow}(E)$, further the measured A_{exp} as shown in eqn. 3.4.

The polarization of a bunch of neutrons describes the relative difference of neutron fractions with different spin states:

$$P = \frac{X^{\uparrow} - X^{\downarrow}}{X^{\uparrow} + X^{\downarrow}}, \quad P \in [-1, 1] \tag{3.9}$$

$X^{\uparrow}$ denotes the number of neutrons with the designated spin state, and $X^{\downarrow}$ means that with the opposite state. The relative fractions of these neutrons are

$$X^{\uparrow} = \frac{1}{2}(1+P)\cdot(X^{\uparrow} + X^{\downarrow}), \quad X^{\downarrow} = \frac{1}{2}(1-P)\cdot(X^{\uparrow} + X^{\downarrow}) \tag{3.10}$$

The neutron polarization in PERKEOIII is defined by the *supermirror polariser* after the velocity selector. The polariser has a set of pyrex glass plates, which are coated with alternating layers of ferromagnetic material (e.g. Cobalt or Nickel) and neutron absorbing material (e.g. Titanium or Gadolinium). The plates are bended with a 30 m curvature, and stacked together with 2 mm spacing between each. Sketches of the polariser are shown in figure 3.10.

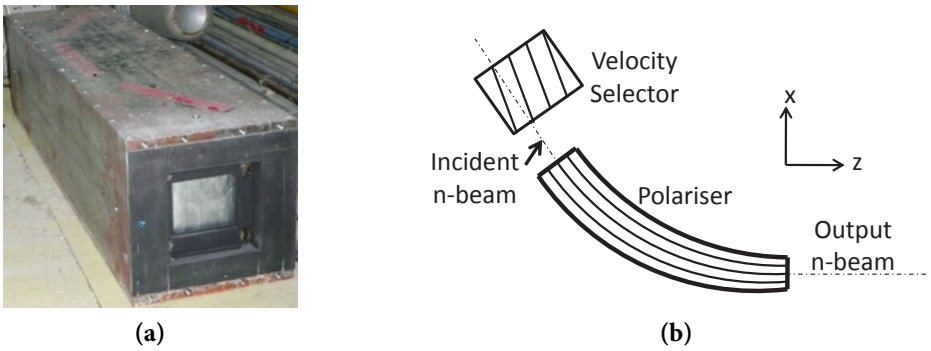

Figure 3.10: Picture of supermirror polariser of PF1b and a sketchy plot. In order to get maximal neutron flux, the H113 and the PERKEOIII beam line are parallel to the tangent of polariser curve at input and output window.

The housing of the polariser supplies a vertical static magnetic field, which is parallel to the supermirror and saturates the ferromagnetic layers. The neutrons in the magnetic field have two eigenstates of spin: parallel or anti-parallel to the magnetic field. In the collisions with the polariser, the neutrons with spin state anti-parallel to the magnetic field transmit through the Ni layers then are absorbed by the Ti layer, while the neutrons with the opposite spin state are reflected [Wil88].

The polariser in PF1b uses m = 2.8 supermirrors on the pyrex glass plates, which have lengths of 80 cm and a curvature of 26.7 mrad. The polarization of the output neutrons can reach the level of P≈98.8%, with n-beam transmission of 24%. More parameters are listed in [Sol02].

The curved structure of polariser can ensure at least one collision of input neutron with the supermirror. Whereas the curvature also considerably changes the angular distribution of n-beam due to several times of collision, as sketched in figure 3.11.

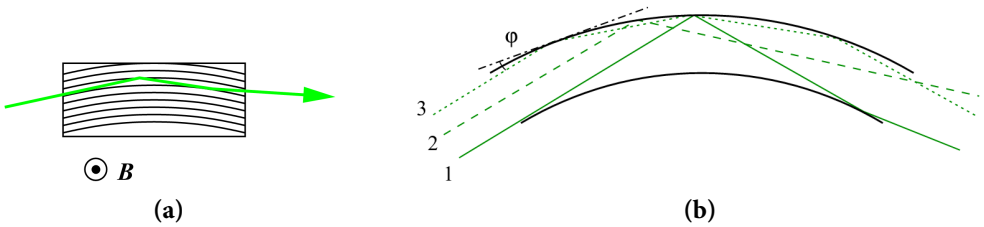

Figure 3.11: Sketches of the neutron collisions in the curved polariser. Due to several times collisions, the n-beam divergence is considerably changed. Figures are from [Kre05].

Figure 3.12 shows the simulated divergence distributions of n-beam from polariser.

As shown in simulation, the maximum horizontal divergence of the output n-beam is extended by 20% compare with the input n-beam in figure 3.9.

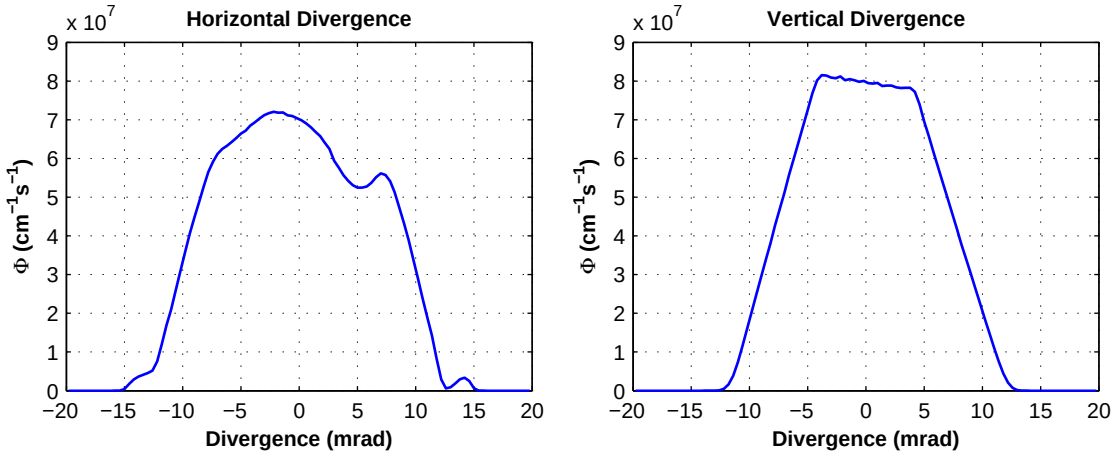

(a) Horizontal direction **(b)** Vertical direction

Figure 3.12: Simulated divergence distribution of output n-beam in horizontal and vertical directions. The peaks in the horizontal distribution denote the neutrons that have different times of collisions with the polariser.

3.3.4 Radio frequency spin-flipper

After the neutron polariser, we applied an adiabatic *radio frequency spin flipper* system [Baz93] to switch the neutrons spin state parallel or anti-parallel to the guiding magnetic field of PERKEOIII.

The spin flipper supplies a static magnetic field $B_s(z)$ in vertical direction, which is the same as the field of the polariser. The strength of $B_s(z)$ has a gradient along the beam line, and drops to a specified $B_s(z_0)$ at the flipping point. An 80 cm long Cu coil powered by AC is used to produce an alternating magnetic field B_{RF} in z-direction. The frequency of B_{RF} is set the same as the Larmor frequency of neutron in the magnetic field $B_s(z_0)$

$$\omega_L = -\gamma B_s(z_0) \tag{3.11}$$

with the neutron gyromagnetic ratio γ [PDG12].

$$\gamma_n = -\frac{g_n \mu_B}{\hbar} = 1.83 \times 10^8 \; s^{-1} T^{-1} \tag{3.12}$$

At position z_0, the neutron spin $\boldsymbol{\sigma}$ is resonant with B_{RF} frequency, and progresses in the horizontal direction. Further after z_0, B_s keeps decreasing and $\boldsymbol{\sigma}$ is reversed to the opposite direction [RK11]. The principle of the spin flipper is sketched in figure 3.13.

Practically, the spin-flipper switches the neutron spin with a efficiency of F

$$F = \frac{X^{\uparrow\Rightarrow\downarrow}}{X^{\uparrow}} = \frac{X^{\downarrow\Rightarrow\uparrow}}{X^{\downarrow}} \tag{3.13}$$

$X^{\uparrow\Rightarrow\downarrow}$ means the number of the neutrons whose spins are flipped from one state to another. If the n-beam out from polariser has the polarization of P_0, the spin-flipper will change the

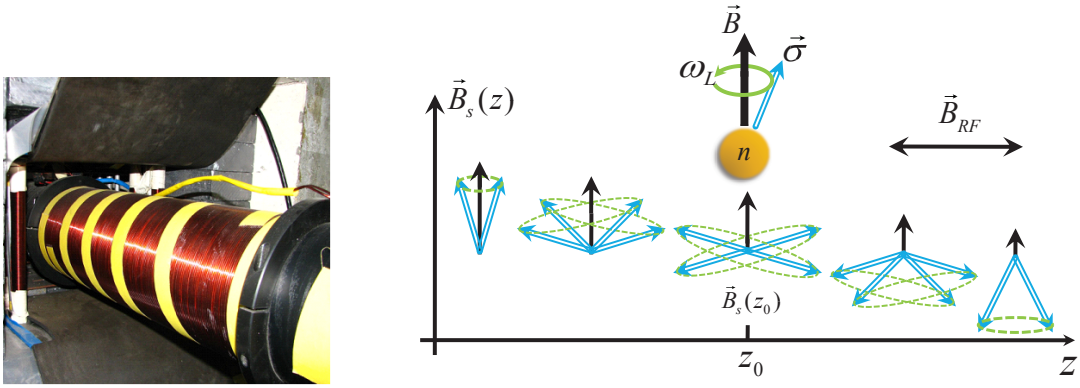

(a) (b)

Figure 3.13: Picture of the RF spin flipper in PERKEOIII, and sketch of the flippering method.

polarization to P_1.

$$P_1 = (1 - 2F)P_0 \tag{3.14}$$

In the experiment, we switch the neutron spin states by turning on and off the spin flipper, namely the flipper only affects one of the spin states.

Define $n^{\uparrow,\downarrow}$ as the e^- spectra from pure polarized neutrons, the ideal A_{exp} is:

$$A_{exp} = \frac{n^{\uparrow} - n^{\downarrow}}{n^{\uparrow} + n^{\downarrow}} = \frac{1}{2}A\beta \tag{3.15}$$

Assuming the spin flipper only act on the $N^{\downarrow}$ measurement, the measured spectra after the operation of polariser and spin-flipper are:

$$\begin{aligned} N^{\uparrow} &= X^{\uparrow}n^{\uparrow} + X^{\downarrow}n^{\downarrow} \\ N^{\downarrow} &= \left[X^{\uparrow}F + X^{\downarrow}(1-F)\right]n^{\downarrow} + \left[X^{\downarrow}F + X^{\uparrow}(1-F)\right]n^{\uparrow} \end{aligned} \tag{3.16}$$

Thus the real measured experimental asymmetry is:

$$\begin{aligned} A'_{exp} &= \frac{N^{\uparrow} - N^{\downarrow}}{N^{\uparrow} + N^{\downarrow}} = \frac{F(X^{\uparrow} - X^{\downarrow})(n^{\uparrow} - n^{\downarrow})}{2(X^{\uparrow}n^{\uparrow} + X^{\downarrow}n^{\downarrow}) - F(X^{\uparrow} - X^{\downarrow})(n^{\uparrow} - n^{\downarrow})} \\ &= \frac{FP}{\frac{1}{A_{exp}} + P(1-F)} = \frac{FP}{\frac{2}{A_0\beta} + P(1-F)} \end{aligned} \tag{3.17}$$

where P is the polarization of n-beam out from polariser. When the flipping efficiency is near unity

$$F \to 1, \quad A'_{exp} \approx \frac{1}{2}PF \cdot A\beta \tag{3.18}$$

From the spin flipper to the detector vessel, a static magnetic field is applied around the beam line. The direction of the static field changes smoothly from vertical to longitudinal

direction of the n-beam, and couples to the PERKEOIII guiding field in the detector vessel. During transportation, the neutron spin states can adiabatically follow the magnetic field without depolarization.

The neutron polarization in the decay volume is a combination of the effects of polariser and spin flipper. As shown in eqn. 3.18, it is an important coefficient for the A_{exp} analyses. In the PERKEOIII experiment, the real time neutron polarization was kept measuring at the end of the instrument during the electron detection.

3.3.5 Neutron apertures

The divergence of the n-beam will extend the n-beam cross-section size during the neutrons propagations in PERKEOIII, and cause systematic errors of measurement (Section 6.2). To limit the n-beam divergence distributions, we applied 5 neutron apertures on the beam line.

The neutron apertures have ^{6}LiF plates attached on the Pb blocks, with open windows of 6×6 cm^2, as shown in figure 3.14.

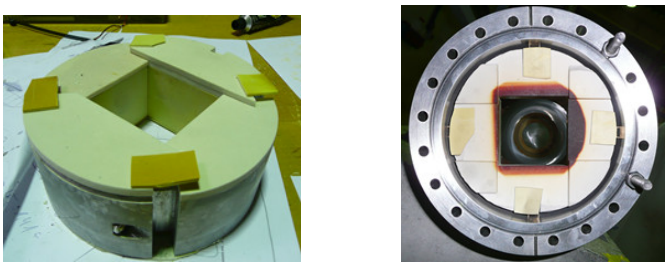

(a) **(b)**

Figure 3.14: Neutron apertures in PERKEOIII beam line.

The distance between the first and the last apertures is 3.23 m, which can limit the n-beam divergence below 1.1°. The divergence distributions of output neutrons are plotted in figure 3.15.

3.3.6 Disk chopper

A disc chopper was applied after the apertures to generate the neutron pulses (n-pulse) in PERKEOIII experiment. The chopper consists of a rotating disc with neutron absorber ^{6}LiF plates attached on one side. An open window with 22.11° is left on the disc [Wer09], and allows the neutrons to pass for a certain time when the chopper is rotating. Figure 3.16 shows the geometry of the disc chopper.

By choosing the rotating speed, the chopper can define the spatial and temporal length of the n-pulse. In the experiment, the nominal rotation frequency was set as 83 Hz and 94 Hz, corresponding to the cycle periods as 12.0 ms and 10.6 ms.

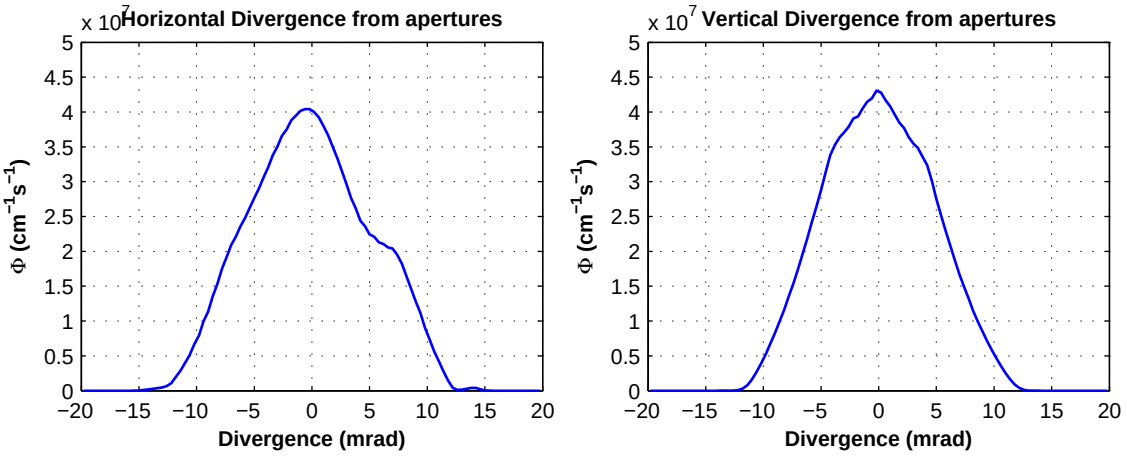

(a) Horizontal direction **(b)** Vertical direction

Figure 3.15: Simulated divergence distribution of neutrons from the apertures.

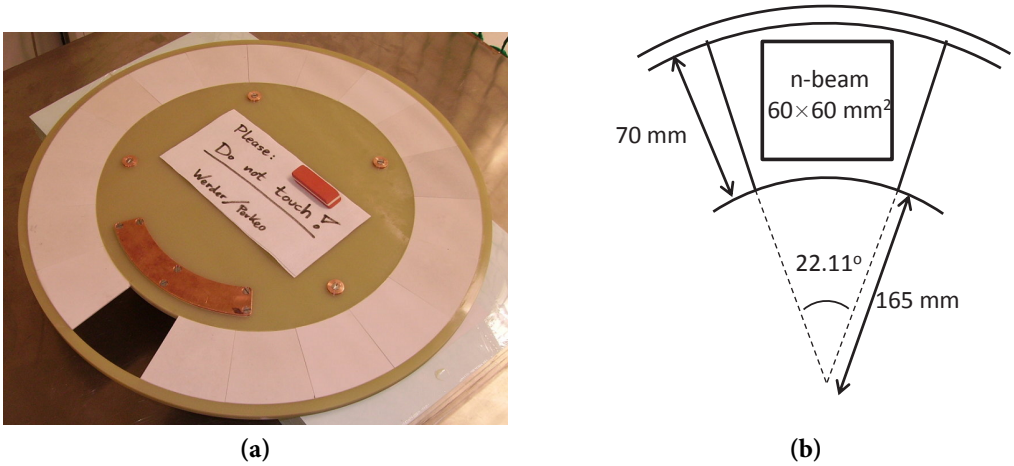

(a) **(b)**

Figure 3.16: **(a)** The picture of the disk chopper of PERKEOIII. **(b)** The geometry sketch of the chopper.

3.3.7 Neutron beamstop

The neutron beamstop was placed at the end of PERKEOIII below the downstream detector to absorb the rest neutrons that passed through the decay volume. In the experiment, we used ^{6}LiF and $^{10}B_4C$ as the absorbing material.

The ^{6}LiF is clean and efficient for neutron absorption, but produces secondary hot neutrons after the neutron absorption. The secondary neutrons can decay after a certain time, and contaminate the background measurement when we applied pulsed n-beam (Section 5.2). The $^{10}B_4C$ produces much less secondary neutrons, whereas generates a large amount of γ radiation during neutron absorption. Moreover, the beamstops have probabilities to scatter neutrons in arbitrary directions. In the experiment, we applied layers of Boron plastic and

(a) ^{6}LiF beamstop. **(b)** $^{10}B_4C$ beamstop

Figure 3.17: ^{6}LiF and $^{10}B_4C$ neutron beamstop of PERKEOIII.

Pd bulks around the beamstop to shield the backgrounds.

3.4 Main Instrument of PERKEOIII

The main instrument of PERKEOIII has a symmetric layout. The decay volume vessel located in the middle has a length of 2.7 m and the inner diameter of 50 cm. With continuous n-beam, the large decay volume can supply a high event rate of 10^3 Hz. Additionally, the long decay volume allows the neutrons to have relative long time passing through. This feature ensures the possibility of the measurements with pulsed n-beam.

At the ends of decay volume, two detector vessels are connected. At the upper ends of the detector vessels, the detector systems are located at the upstream and downstream (Detector 1 and Detector 2) above the n-beam. Around the instrument, a set of coils generate a curved guiding field from the decay volume to the detectors.

3.4.1 Magnets system

The magnetic guiding field in PERKEOIII is supplied by 50 water cooled copper coils outside the non-magnetized stainless vessels.

The magnetic field in decay volume has a relative homogeneous distribution, with the strength of 150 mT. The tilted coils at the detector vessels bend the magnetic lines from the decay volume twice, then project them to the two detectors, where the field is decreased to 80 mT. The two reverse bends minimize the $\mathbf{R}\times\mathbf{B}$ drift effect of electrons in PERKEOIII (Section B.4). The electrons from decay volume will experience one left and one right drift, and the total drifts are roughly counteracted. The entire magnetic field distribution is symmetric according to the center of the decay volume.

The properties of the magnetic field are discussed in Section 4.3

3.4.2 Scintillator detector system

PERKEOIII has two 2π detectors symmetrically located at upstream and downstream of the n-beam for electron energy measurements.

The detector consists of a plastic scintillator in the center of the Al supports. Six photomultiplier tubes (PMT) are located around, and connected to the scintillator with plexiglass light guides. Figure 3.18 shows the construction of the detector system.

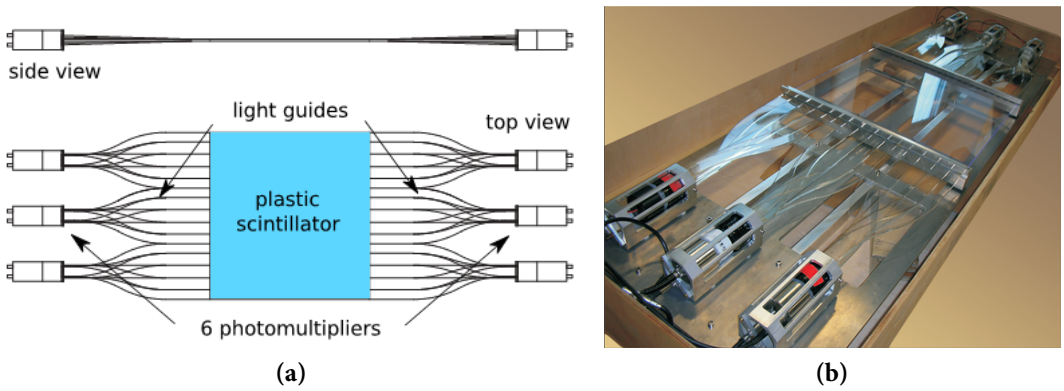

(a) (b)

Figure 3.18: The scintillator detector of PERKEOIII. The plastic scintillator in the center has a size of $43\times45\times0.5$ cm^3.

When the incident electron interacts with the scintillator, its energy is converted into a number of visible photons by several times collisions. A certain fraction of the photons can be transferred via the light guides to the PMT, where the photons are convert into electrical charges. In the electronics system, the Analog to Digital Converter (ADC) modules integrate the charges of the six PMT in a time period of t_{gate}=220 ns, and output one event including the information of the measured time and the integrated charge.

The relation between the measured charge signals (represented by ADC channels) and the electron energies is important to derive the electron energy spectra. During the experiment, the relation is determined by measuring the spectra of different calibration sources, which have different known energy peaks. Figure 3.19 shows the relation between the measured ADC channels and the source energies, and the fittings to the relation.

As it is shown in figure 3.19, in the range of 300 keV$<E_e<$700 keV, the proportionality relation can be applied for converting the channel number to the electron energies.

Because of the characters of scintillator, the detector can record different kinds of radiation, e.g. visible light, γ-rays or other charged particles, as the background of measurements. In the experiment, the instrument is well sealed and evacuated to prevent signals from visible light and ions. Hence the main source of the background is the γ radiation, which are generated by the neutron absorptions at the beam line and the beamstop, as well as the neighbouring experiments.

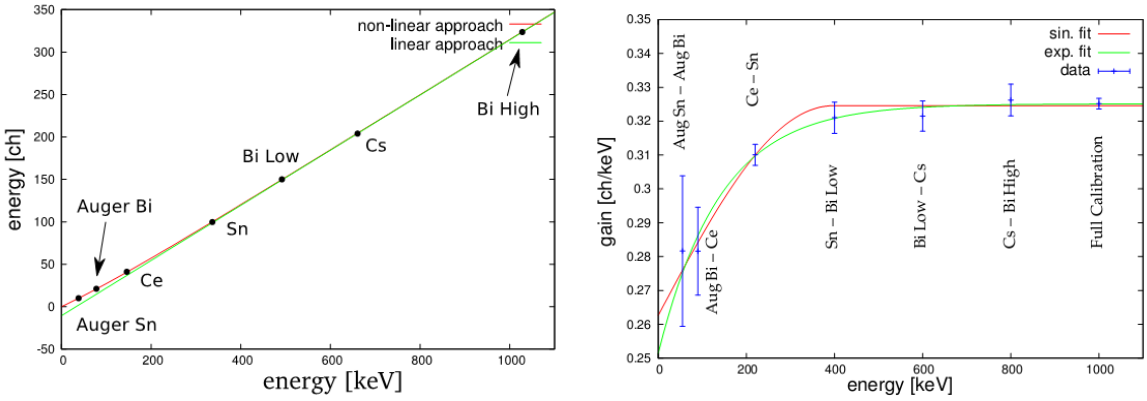

(a) **(b)**

Figure 3.19: (a) The measured peaks of the calibration sources in ADC channels, versus the real energies of them. Green and red curves denote the linear and exponential fittings. **(b)** The channel-energy slope (gain) of every 2 nearest peaks, versus the average energy of the 2 peaks. *Full calibration* means the slope of the linear fitting of the 4 peaks from Sn, Cs and Bi. The values are fitted by sinusoidal and exponential curves. The calculations and the figures are from [Mes11].

With the integration function of the guiding magnetic field, the two detectors are able to realize 4π solid angle measurements. Furthermore, the symmetric geometry of the two detectors brings us merits on systematics, e.g. backscattered electron measurements (Section 5.1), detector trigger function determination, symmetric mirror effect correction etc..

Chapter 4

Properties of Neutron Beam and Magnetic Field of PERKEOIII

The long decay volume and the magnets of PERKEOIII allow the n-pulse to have relative long time passing through the homogeneous magnetic field, where the neutrons can provide stable signals of decay electrons. With this feature, the systematic errors of the measurement can be highly suppressed, and the measurement efficiency can be enhanced.

In the mean time, the properties of the n-pulse and the magnetic field become important. These properties are necessary, e.g. in the selection of data, the determination of the systematic effects and errors. In this chapter, we introduce the spatial and the temporal properties of the n-pulse, and the magnetic field in PERKEOIII instrument.

With the simulations, we are able to investigate these properties in detail, and have better understanding to the system, thus avoid possible defects during experiment and data processing. Some of the simulated results are compared with the results from measurements. As shown in this chapter, the simulated results have well fittings to the measured results.

In addition, we calculate the corrections of the magnetic mirror effect directly in the neutron simulation. In this case, the complicated distribution of the neutrons can be taken into account, and the corrections can reach a high accuracy.

4.1 Properties of Pulsed Neutron Beam in PERKEOIII

4.1.1 Spatial properties of neutron beam

The spatial property of the n-beam which interested us, is the beam cross-section profile, which is expanded by the divergence of the n-beam during neutron propagation. The n-beam cross-section defines the size of the electron beam, which causes the corrections of scintillator detector.

The n-beam cross-section was measured in the experiment by copper foil activations. We expose a piece of 0.2 mm thick Cu foil by the n-beam at the beamstop, then measure the decay β-ray from the activated Cu. The β-ray intensity is proportional to density of the activated Cu, thus proportional to the capture flux of the n-beam that passed the foil. Figure

4.1 shows the measured β intensity along the horizontal and the vertical directions, and the simulated capture flux distribution.

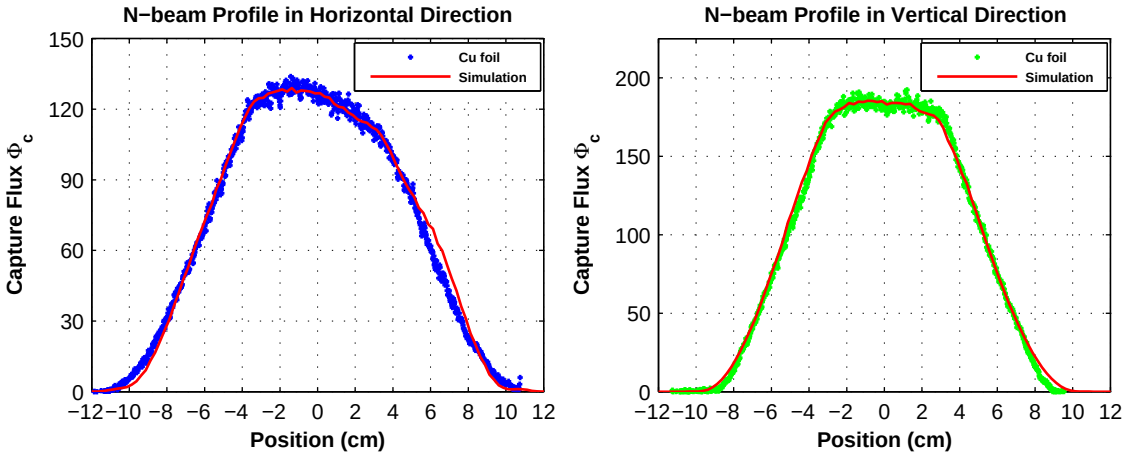

(a) Horizontal direction **(b)** Vertical direction

Figure 4.1: The measured intensity of decay β-ray from activated Cu foil along horizontal and vertical directions. The red curves denote the simulated neutron capture flux at the PERKEOIII beamstop, which is 6 m from the last neutron aperture.

As shown in figure 4.1, the cross-section of n-beam profile is measured as 23×19 cm^2 at the end of PERKEOIII, which is 6 m away from the last aperture. If we don't consider the neutron scattering effect from the apertures, the maximum divergence of the n-beam is then ±14.2 mrad and ±10.8 mrad in horizontal and vertical directions.

The *effective decay volume* (discussed in Section 4.3.2) has a length of 2.5 m, and the center 2.98 m away from the last aperture. Hence the n-beam cross-sections at the beginning and the end of the effective decay volume have the sizes of 11×10 cm^2 and 18×15 cm^2 respectively.

Considering the magnetic field in decay volume is 150 mT, the maximum gyration radius of decay electrons with maximum momentum p_{max}=1.19 MeV/c is then

$$r_{max} = \frac{p_{max}}{qB} = \frac{1.19\ \text{MeV}/c}{e\cdot 150\ \text{mT}} = 2.64\ \text{cm} \tag{4.1}$$

The maximal e-beam cross-section in decay volume is

$$S_e = (W_n + 4r_{max}) \times (H_n + 4r_{max}) = 28.56 \times 25.56\ \text{cm}^2 \tag{4.2}$$

and the e-beam size at the detector with 80 mT is then

$$S_{det} = \frac{150\ \text{mT}}{80\ \text{mT}} S_{decay} = 39.10 \times 35.00\ \text{cm}^2 \tag{4.3}$$

The simulated trajectories of the electrons are shown in Section 4.3.

4.1.2 Time properties of neutron pulse

The temporal length of the n-pulse is defined by the velocity selector and the chopper. However, the operations of these elements only limit the distributions in a range. Figure 4.2 shows the simulated spectrum of n-beam output from the chopper, and the corresponding velocity distributions.

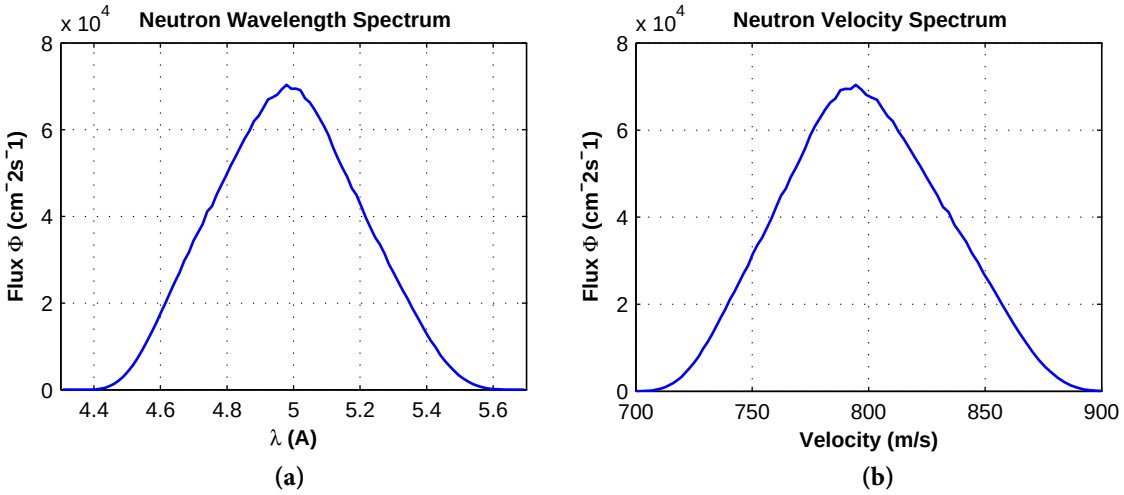

Figure 4.2: (a) Simulated spectrum of neutrons inside PERKEOIII, with the nominal wavelength λ_0=5Å. The neutron spectrum after chopper has slight changes from that after the velocity selector in figure 3.8, because the apertures limit the n-beam divergence, whose distribution is related to the λ. **(b)** The corresponding velocity distributions of neutrons.

As shown in figure 4.2, the neutron wavelengths in PERKEOIII are in a range of 4.4 Å<λ<5.6 Å, corresponding to the velocities in 706 m/s<v< 899 m/s. During the neutron propagation from the chopper to the beamstop (11 ms), the n-pulse length will be elongated by 2.1 m due to the velocity deviations.

To determine the temporal properties of the n-pulse, we measured the neutron TOF in experiment. Inside the decay volume, we placed two 1 mm thick Al foils with 2 m distance. When the n-pulse passes through the foils, fractions of the neutrons have (n, γ) reactions with Al and emit instantaneous γ-rays. Outside the vessel, two detectors are placed directly below the Al foils to measure the TOF of γ signals. Since the (n, γ) reaction rate is proportional to the neutron capture flux Φ_c, the γ events from detectors directly represent the TOF of the n-pulse in the decay volume. Figure 4.3 shows the measured TOF diagram from γ detectors, and the simulated capture flux Φ_c at the positions of the Al foils.

4.2 Measurement with Pulsed Neutron Beam

The pulsed neutron beam can provide us an additional time scale in the measurement. With the time scale, we are able to choose the events in specific time ranges, which stand for the

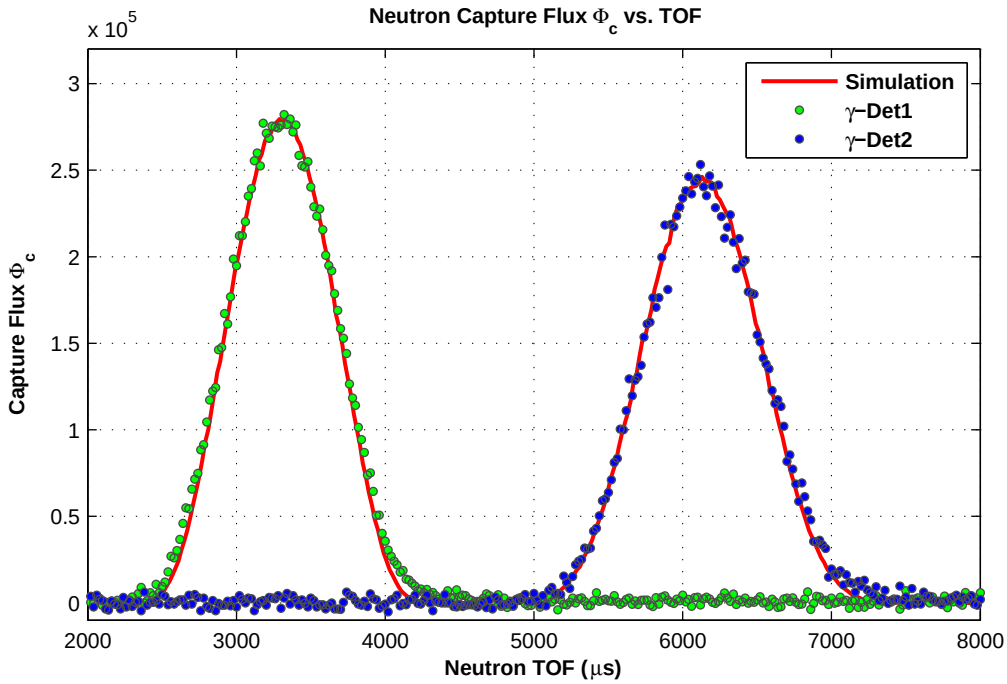

Figure 4.3: The measured TOF diagram from two γ detectors, and the simulated TOF of neutron capture flux Φ_c at the positions of the Al foils (red curve). Chopper frequency is f=75 Hz, velocity selector speed is ω=23155 rpm. The velocity selector was 7.6 mrad tilted during the measurement, so the equivalent nominal wavelength is λ_0=5.6 Å. Since the γ detectors have different efficiencies, the measured even rates from the two detectors are rescaled to fit the simulated results.

n-pulse at the specific positions. Figure 4.4 shows a sketch of the space-time diagram of a n-pulse propagation inside PERKEOIII during one chopper cycle.

The decay electrons (in keV) have speeds almost as light, which is much higher than the cold neutrons. Thus the TOF diagram of electron signals at the two scintillator detectors can indicate the instantaneous TOF of the n-pulse. Figure 4.5 shows the TOF diagram of measured signals from both detectors, corresponding to the time scale of figure 4.4.

When the n-pulse is in the detector vessel (0 ms~2 ms), the decay electrons cannot be totally projected to detectors by magnetic lines, as shown in figure 3.2. The detectors see low event rates during this time period. In the time range of 3 ms~5 ms, the whole n-pulse is inside the decay volume. The neutrons are in a homogeneous magnetic field, and all decay electrons can be guided to the detectors. Hence the sum of the event rates from two detectors are unchanged during this time [1]. The events rates of the individual detectors have symmetric slopes, which are caused by magnetic mirror effect as discussed in Section 4.4. From 6.5 ms to 9 ms, the neutrons are being absorbed by the beamstop, and much γ-rays are created. Detector 2 is nearer to the beamstop, hence receives more signals. From

[1] Free neutron has a life time of 880.1 s, the decay probability during 10 ms is about 10^{-5}. The number of neutrons and the decay rate can be considered as constants in the measurement.

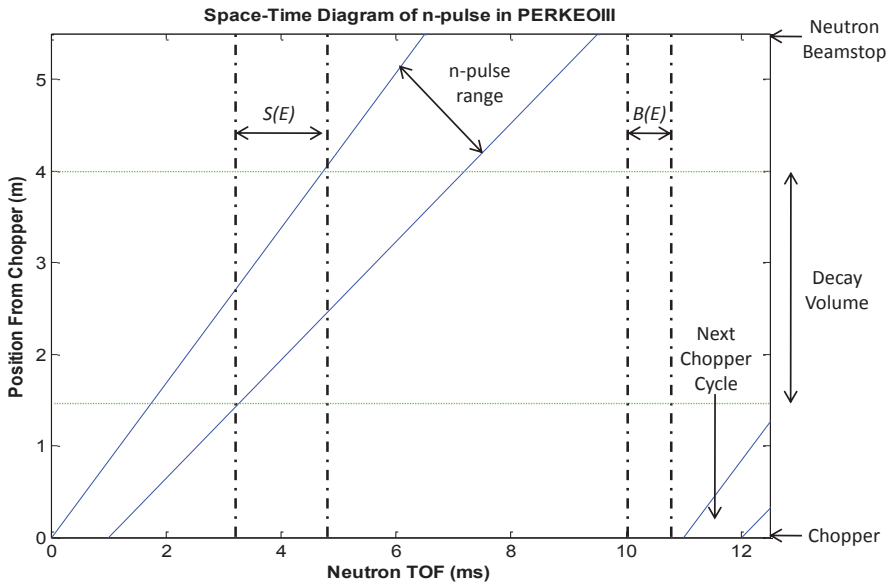

Figure 4.4: Space-time diagram of n-beam pulse in PERKEOIII. The horizontal and longitudinal axes indicate the neutron TOF and the position relative to the chopper. The area inside the blue lines denotes the neutrons in the pulse, which elongates during propagation because of the neutron velocity distribution. Chopper frequency is set as 94 Hz, the chopper window opens at t=0, closes at t=1.3 ms. One cycle lasts for 10.6 ms.

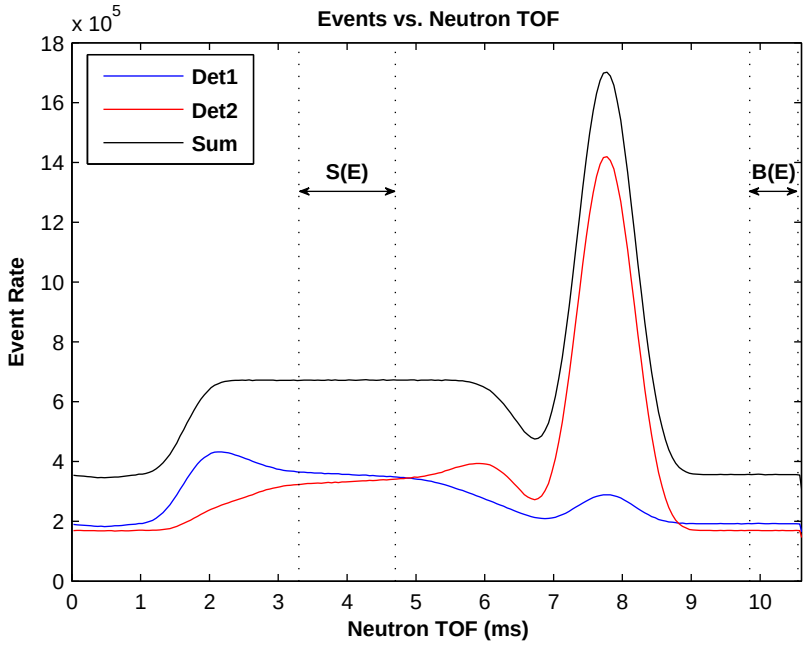

Figure 4.5: The TOF diagram of electron signals measured by two scintillator detectors in one chopper cycle. The curves denote the signals from detector 1 (blue), detector 2 (red) and the sum (black) of them. The time scale is comparable to figure 4.4. The electronic clocks are able to record the events with resolution of 1 μs.

9 ms to the end of cycle, the neutrons are totally absorbed, and the detectors only receive the background from the beam line and the external sources.

In data processing, we select the events when the n-pulse is totally inside the 2.5 m homogeneous *effective decay volume* (Section 4.3.2) as the signal spectrum $S(E)$. The events after the neutrons are all absorbed by beamstop, are chosen as the background spectrum $B(E)$, as marked in figure 4.5. The selections of time windows for $S(E)$ and $B(E)$ are discussed in Section 5.2.

To obtain a pure spectrum of decay electrons, we subtract the signal $S(E)$ by the background $B(E)$ in each chopper cycle

$$N(E) = S(E) - \frac{T_s}{T_{bg}} B(E) \tag{4.4}$$

T_s/T_{bg} is the ratio of the time window lengths of the signal and background. Figure 4.6 shows the measured spectra of the signal, the background and the evaluated pure electron spectrum.

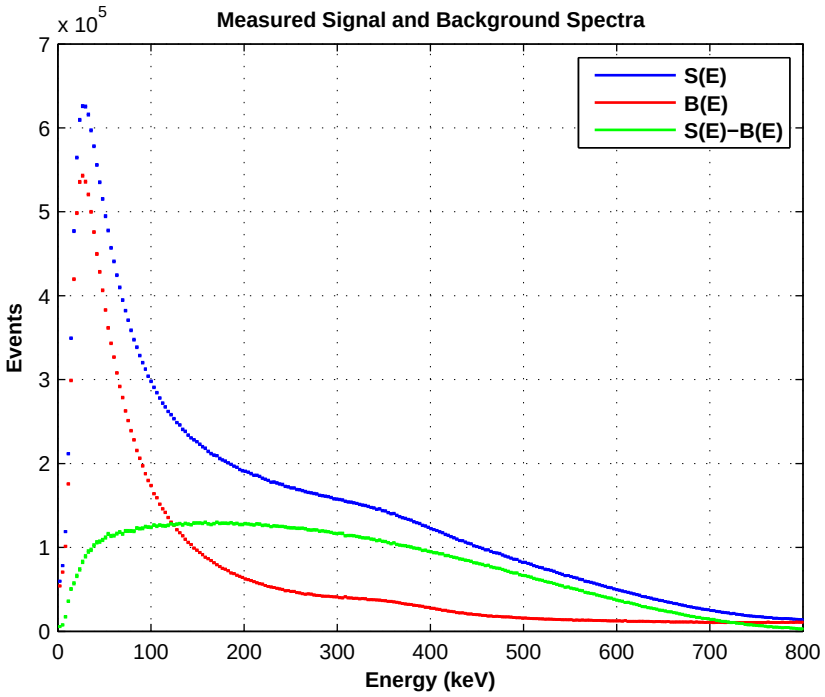

Figure 4.6: Measured energy spectra from Detector 2. Blue and red curves show the spectra of $S(E)$ and $B(E)$. The green curve is the difference of these two spectra, and denotes the net energy spectrum $N(E)$ of decay electrons.

By selecting the events with specific time ranges, we are able to suppress the systematic errors related to:

- *Edge effect.*

When the neutrons are not in decay volume, part of the decay electrons cannot be projected to the detectors, but have collisions with the inner wall of the instrument. The collisions may cause the absorptions or changes on electron energies, so-called as *edge effect*, which leads to the distortion of measured spectrum. The edge effect is prevented by selecting a specific $S(E)$ measuring time, when the decay electrons are totally guided to the detectors.

- *Beamstop background.*

  During the time period of $S(E)$ and $B(E)$, the n-pulse has no interactions with the instrument. The background generated by neutron beamstop can be prevented.

- *Slowly varied environment.*

  Both $S(E)$ and $B(E)$ are measured in each chopper cycle, only with a time difference $\Delta t \approx 7$ ms. Hence the resulted $N(E)$ are maximally independent on the slow variation of the environment, e.g. the γ background from neighbouring experiments, neutron flux variation etc.

- *Correction of magnetic mirror effect.*

  The $S(E)$ events are selected when the neutrons are in a homogeneous field, hence the corrections of magnetic mirror effect are relative small.

To obtain an optimized measurement efficiency, the length and the velocity of the n-pulse need to be selected well. In the experiment, the velocity selector speed was set as ω=25470 rpm, and the chopper frequency as 83 Hz and 94 Hz .

4.3 Properties of Magnetic Field of PERKEOIII

4.3.1 Pitch angle distribution

From the decay volume to the detectors, the magnetic field is gradually decreased from 150 mT to 80 mT. During the adiabatic transport in the gradient field, the pitch angles of electrons are smoothly changed.

The maximal emission angle of electrons in decay volume is 90° to the magnetic lines. According to eqn. B.6, the maximal pitch angle is decreased to

$$\theta_c = \arcsin\left(\sqrt{\frac{80\ \mathrm{mT}}{150\ \mathrm{mT}}} \cdot \sin 90^\mathrm{o}\right) = 47^\mathrm{o} \tag{4.5}$$

at the detector. If we assume the electrons are isotropically emitted in the decay volume, the distribution of electron pitch angles is

$$\frac{\mathrm{d}N}{\mathrm{d}\theta_0} = W_{iso}(\theta)\sin\theta_0 = \frac{1}{2}\sin\theta_0, \quad 0^\mathrm{o} \leqslant \theta_0 \leqslant 90^\mathrm{o} \tag{4.6}$$

When the electrons reach the detector, the pitch angles of them are changed to θ_1

$$\frac{\sin\theta_1}{\sin\theta_0} = \sqrt{\frac{B_1}{B_0}} = \sin 47^o \tag{4.7}$$

The pitch angle distribution at detector is then

$$\frac{dN}{d\theta_1} = \frac{1}{2}\frac{1}{\sin 47^o}\frac{\sin\theta_1\cos\theta_1}{\sqrt{\sin^2 47^o - \sin^2\theta_1}}, \quad 0^o \leqslant \theta_1 \leqslant 47^o \tag{4.8}$$

Figure 4.7 plots the probability distribution of electron pitch angles in the decay volume and the detector.

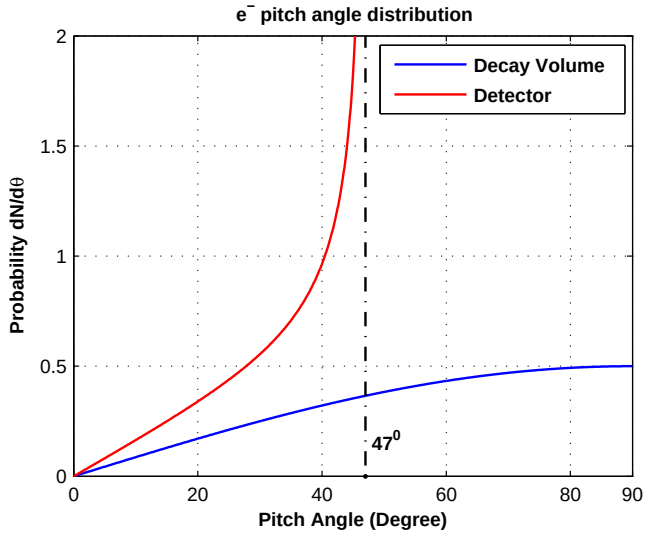

Figure 4.7: The electron pitch angle distribution in the decay volume (blue) and at the detector (red). Assuming the electrons are isotropically emitted in decay volume.

The electron pitch angle at the detectors can be considered same as its incident angle into the scintillator. The decreases of pitch angles can efficiently suppress the backscattering effect off the detector, as discussed in Section 5.1.

4.3.2 Magnetic field in the decay volume

In the experiment, the magnetic fields in the $20\times20\times270$ cm^3 space of decay volume were measured. The results are shown in figure 4.8.

As plotted in figure 4.8, the magnetic field in the decay volume has a symmetric distribution. The maximal magnetic field is B_{max}=152 mT, which is located in the middle of the decay volume, and 2.78 m from the chopper.

The 2.5 m middle range of the decay volume has the most homogeneous magnetic field, hence is chosen as the *effective decay volume*. The period when the n-pulse is totally in this range is selected as the time window for the signal spectra $S(E)$ measurements.

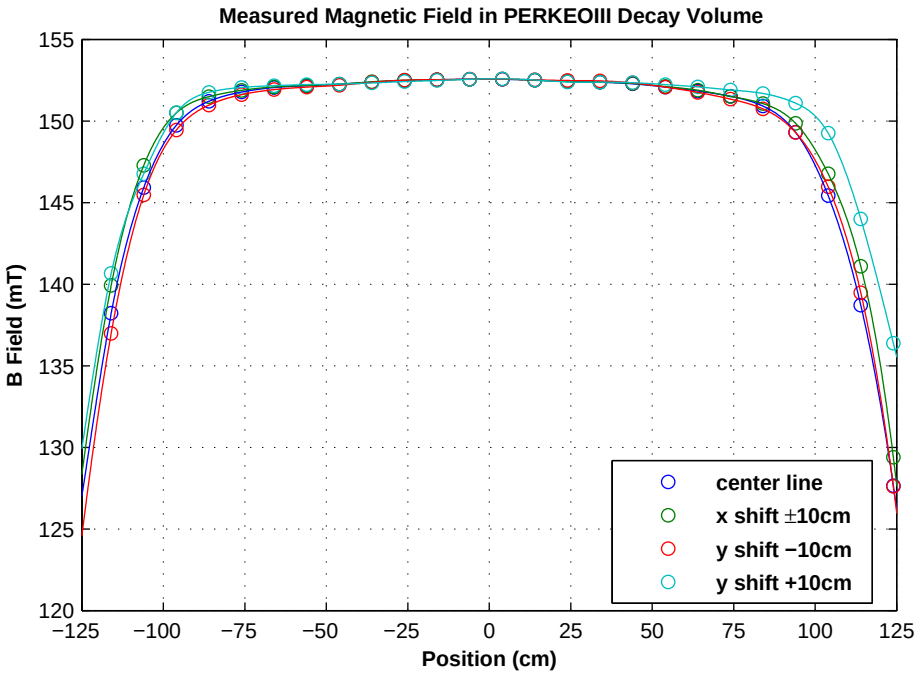

Figure 4.8: The measured magnetic field along z-direction in the decay volume (circles) and fitting curves. Different curves denote the magnetic field along the central and 10 cm shifted lines in x and y direction. z=0 point denotes the decay volume center, which is 2.78 m from the chopper.

4.3.3 Electrons trajectories simulation

With the program CST Studio, we calculate the trajectories of the electrons emitted from the effective decay volume, where the spectrum $S(E)$ is chosen. Figure 4.9 and 4.10 show the simulated electron trajectories in PERKEOIII and the distributions at the detectors.

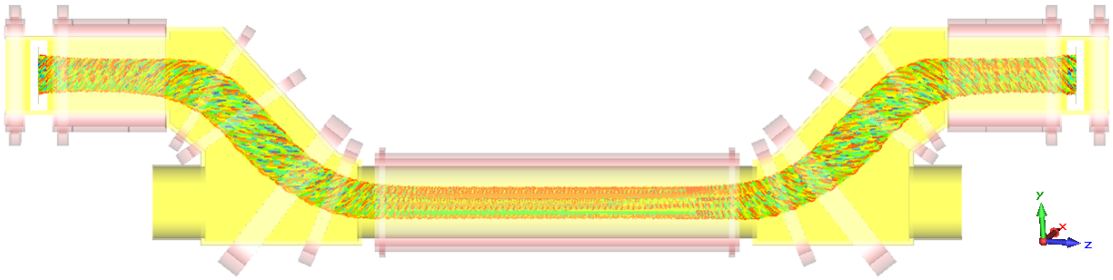

Figure 4.9: The simulated electrons trajectories in PERKEOIII.The electrons are emitted from the neutrons in the effective decay volume, with the dimensions as calculated in Section 4.1.1. The simulation file is supplied by Dr. B. Märkisch of University of Heidelberg.

In the simulation, the electrons are emitted from the neutron source in the 2.5 m long effective decay volume. The dimensions of the neutron source are same as that calculated in Section 4.1.1.

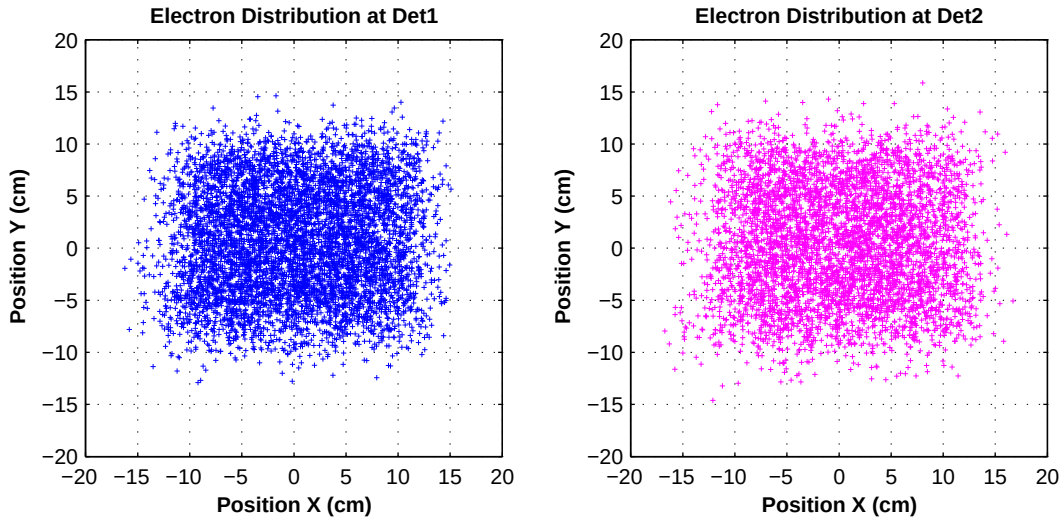

(a) Detector 1 **(b)** Detector 2

Figure 4.10: The simulated electron distributions at the two detectors.

The cross-sections of the electron beam at the detectors as shown in figure 4.10, have the maximal size as 34×30 cm^2. The e-beam sizes need to be considered for the corrections on the scintillators, e.g. the calibrations and deposition position dependencies.

4.4 Corrections of magnetic mirror effects

As discussed in Section B.3, the high magnetic field can reflect the electron from low magnetic field, if its pitch angle θ is smaller than the critical angle θ_c, so called as *magnetic mirror effect*. In the decay volume of PERKEOIII, if the electron is emitted in a low field with emission angle larger than θ_c, it will be reflected by B_{max} in the middle, then guided to the opposite detector. Depends on the n-pulse position, the two detectors will receive electrons with different emission solid angles, as sketched in 4.11.

Since the magnetic mirror effect changes the electron emission angle distribution, it also causes variations of the measured event rates $N(E)$ and experimental asymmetry A_{exp}. In order to derive the corrections on A_{exp}, we need to consider both the magnetic field and the neutron properties in PERKEOIII.

Define the position of maximal magnetic field B_{max} as z_0, and the space with $z < z_0$ and $z > z_0$ as S_L and S_R. For the electrons emitted in S_L with the field $B(\mathbf{r})$, the critical angle is

$$\theta_c = \arcsin\sqrt{\frac{B(\mathbf{r})}{B_{max}}}, \quad B(\mathbf{r}) \leqslant B_{max}, \quad 0 \leqslant \theta_c \leqslant \frac{\pi}{2} \tag{4.9}$$

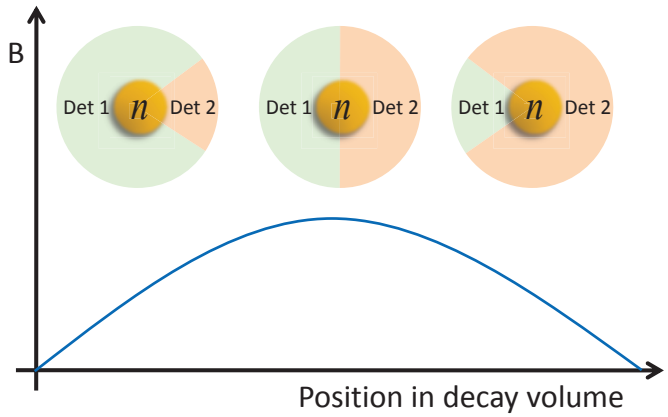

Figure 4.11: A sketch of the magnetic mirror effect in PERKEOIII decay volume. The green and red areas indicate the emission solid angles, in which the emitted electrons will be guided to Detector 1 and Detector 2. The solid angles vary with the experienced magnetic fields, thus the position of neutrons.

The relative event rates received by Detector 1 for spin-up and spin-down neutrons are

$$N^{\uparrow S_L}_{Det1} = \int_0^{\pi-\theta_c} W(\theta)\sin\theta \mathrm{d}\theta, \quad N^{\downarrow S_L}_{Det1} = \int_{\theta_c}^{\pi} W(\theta)\sin\theta \mathrm{d}\theta \tag{4.10}$$

And for electrons emitted in S_R

$$N^{\uparrow S_R}_{Det1} = \int_0^{\theta_c} W(\theta)\sin\theta \mathrm{d}\theta, \quad N^{\downarrow S_R}_{Det1} = \int_{\pi-\theta_c}^{\pi} W(\theta)\sin\theta \mathrm{d}\theta \tag{4.11}$$

Considering the neutron density distribution in the decay volume $\rho(\mathbf{r})$, the total event rate of Detector 1 is then

$$\begin{aligned} N_{Det1} &= N^{\uparrow}{}_{Det1} + N^{\downarrow}{}_{Det1} \\ &= C\left\{\int_{S_L}\rho(\mathbf{r})\left[N^{\uparrow}(\mathbf{r})_{S_L} + N^{\downarrow}(\mathbf{r})_{S_L}\right]\mathrm{d}^3\mathbf{r} + \int_{S_R}\rho(\mathbf{r})\left[N^{\uparrow}(\mathbf{r})_{S_R} + N^{\downarrow}(\mathbf{r})_{S_R}\right]\mathrm{d}^3\mathbf{r}\right\} \\ &= \frac{C}{2}\left[\int_{S_L+S_R}\rho(\mathbf{r})\mathrm{d}^3\mathbf{r} + \int_{S_L}\rho(\mathbf{r})\cos\theta_c(\mathbf{r})\mathrm{d}^3\mathbf{r} - \int_{S_R}\rho(\mathbf{r})\cos\theta_c(\mathbf{r})\mathrm{d}^3\mathbf{r}\right] \end{aligned} \tag{4.12}$$

where C is a constant that denotes the decay rate. The critical pitch angle $\theta_c(\mathbf{r})$ depends on the magnetic field $B(\mathbf{r})$. Same integration can be done on Detector 2:

$$N_{Det2} = N^{\uparrow}{}_{Det2} + N^{\downarrow}{}_{Det2} = \frac{C}{2}\left[\int_{S_L+S_R}\rho(\mathbf{r})\mathrm{d}^3\mathbf{r} - \int_{S_L}\rho(\mathbf{r})\cos\theta_c(\mathbf{r})\mathrm{d}^3\mathbf{r} + \int_{S_R}\rho(\mathbf{r})\cos\theta_c(\mathbf{r})\mathrm{d}^3\mathbf{r}\right] \tag{4.13}$$

The sum of the event rates is

$$N = N_{Det1} + N_{Det2} = C\int_{S_L+S_R}\rho(\mathbf{r})\mathrm{d}^3\mathbf{r} \tag{4.14}$$

as a constant.

Therefore, the two detectors receive different event rates when the n-pulse is in low field. When the n-pulse passes through the decay volume, the event rates of two detectors change symmetrically due to the $\rho(\mathbf{r})$ changes, as shown in figure 4.3. Since the two detectors have similar efficiencies, the sum of the event rates from both detectors remains unchanged when the n-pulse is in decay volume.

The neutron density $\rho(\mathbf{r})$ is dependent on the TOF and velocities of the neutrons, whereas the neutrons in PERKEOIII have complicated spatial and velocity distributions. Therefore, we used McStas to calculate the neutron densities, further directly derive the relative event rates $N_{Det1,2}$ in the program, with the measured B field as input parameters.

In figure 4.12, the measured electron TOF and the simulated relative event rates ($1 \pm k$, as defined below) are plotted.

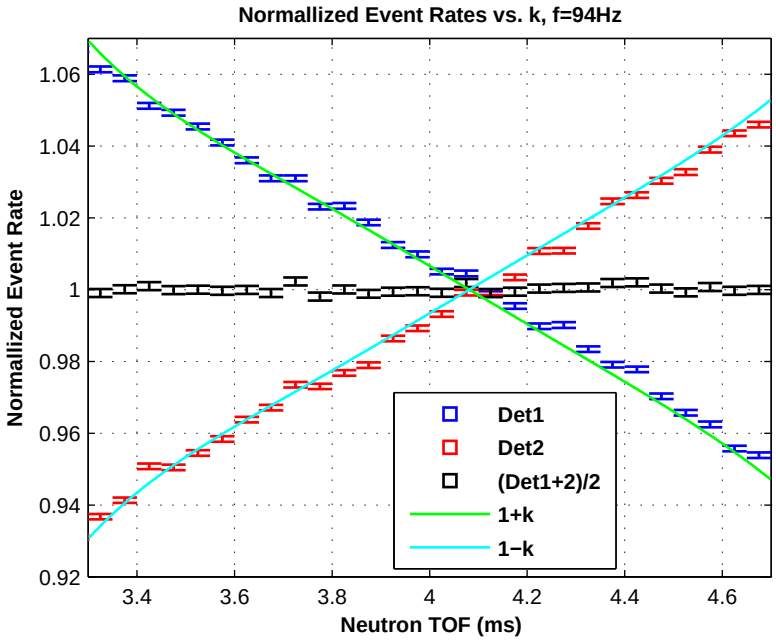

Figure 4.12: The measured TOF diagram of the relative electron event rate, and the simulated event rates of detector 1 and 2 ($1 \pm k$, see below). Chopper frequency is 94 Hz. The signals are subtracted by the background events in 9.85 ms to 10.55 ms. Since the two detectors have not exactly the same efficiencies, the detector 1 event rate is multiplied by 1.06 to keep N_{det1}+N_{det2} as a constant in the 3.3 ms to 4.7 ms range (when the n-pulse is in effect decay volume, see Section 5.2).

The difference of the event rates $N^{\uparrow}(E) - N^{\downarrow}(E)$ is

$$
\begin{aligned}
N^{\uparrow}{}_{Det1} - N^{\downarrow}{}_{Det1} &= C\left\{\int_{S_L}\rho(\mathbf{r})\left[N^{\uparrow}(\mathbf{r})_{S_L} - N^{\downarrow}(\mathbf{r})_{S_L}\right]\mathrm{d}^3\mathbf{r} + \int_{S_R}\rho(\mathbf{r})\left[N^{\uparrow}(\mathbf{r})_{S_R} - N^{\downarrow}(\mathbf{r})_{S_R}\right]\mathrm{d}^3\mathbf{r}\right\} \\
&= \frac{C}{2}A\beta\int_{S_L+S_R}\rho(\mathbf{r})\sin^2\theta_c(\mathbf{r})\mathrm{d}^3\mathbf{r} = \frac{C}{2}A\beta\int_{S_L+S_R}\rho(\mathbf{r})\frac{B(\mathbf{r})}{B_{max}}\mathrm{d}^3\mathbf{r} \\
&= N^{\uparrow}{}_{Det2} - N^{\downarrow}{}_{Det2}
\end{aligned}
\tag{4.15}
$$

which is independent on the space S_L or S_R, and same for Detector 1 and Detector 2. The measured experimental asymmetry is then

$$
\begin{aligned}
A_{exp}^{Det1} &= \frac{N^{\uparrow}{}_{Det1} - N^{\downarrow}{}_{Det1}}{N^{\uparrow}{}_{Det1} + N^{\downarrow}{}_{Det1}} \\
&= \frac{A\beta}{2}\frac{\displaystyle\int_{S_L+S_R}\rho(\mathbf{r})\sin^2\theta_c(\mathbf{r})\mathrm{d}^3\mathbf{r}}{\displaystyle\int_{S_L+S_R}\rho(\mathbf{r})\mathrm{d}^3\mathbf{r} + \int_{S_L}\rho(\mathbf{r})\cos\theta_c(\mathbf{r})\mathrm{d}^3\mathbf{r} - \int_{S_R}\rho(\mathbf{r})\cos\theta_c(\mathbf{r})\mathrm{d}^3\mathbf{r}}
\end{aligned}
\tag{4.16}
$$

Define the factors M and k [Rav95] as

$$
M = \frac{N^{\uparrow} - N^{\downarrow}}{N} = \frac{\displaystyle\int_{S_L+S_R}\rho(\mathbf{r})\sin^2\theta_c(\mathbf{r})\mathrm{d}^3\mathbf{r}}{\displaystyle\int_{S_L+S_R}\rho(\mathbf{r})\mathrm{d}^3\mathbf{r}} = \frac{\displaystyle\int_{S_L+S_R}\rho(\mathbf{r})\frac{B(\mathbf{r})}{B_{max}}\mathrm{d}^3\mathbf{r}}{\displaystyle\int_{S_L+S_R}\rho(\mathbf{r})\mathrm{d}^3\mathbf{r}} \tag{4.17}
$$

$$
k = \frac{N_{Det1} - N_{Det2}}{N} = \frac{\displaystyle\int_{S_L}\rho(\mathbf{r})\cos\theta_c(\mathbf{r})\mathrm{d}^3\mathbf{r} - \int_{S_R}\rho(\mathbf{r})\cos\theta_c(\mathbf{r})\mathrm{d}^3\mathbf{r}}{\displaystyle\int_{S_L+S_R}\rho(\mathbf{r})\mathrm{d}^3\mathbf{r}} \tag{4.18}
$$

The experimental asymmetry can be written as

$$
A_{exp}^{Det1}(E) = \frac{1}{2}A\beta(E)\frac{M}{1+k} \quad , \quad A_{exp}^{Det2}(E) = \frac{1}{2}A\beta(E)\frac{M}{1-k} \tag{4.19}
$$

for two detectors respectively.

Same as the event rates calculation in figure 4.12, we calculate the $M(t)$ and $k(t)$ in McStas simulation. Figure 4.13 plots the simulated $M(t)$, $1 + k(t)$, and the corrections on A_{exp} versus the TOF of the n-pulse in decay volume.

The factor M indicates the magnetic field homogeneity over the n-pulse, and the factor k indicates the field deviations from B_{max}. In the data processing, the corrections of the mirror effect, which are related to the neutron and the magnetic field distributions, need to be considered (Section 5.3).

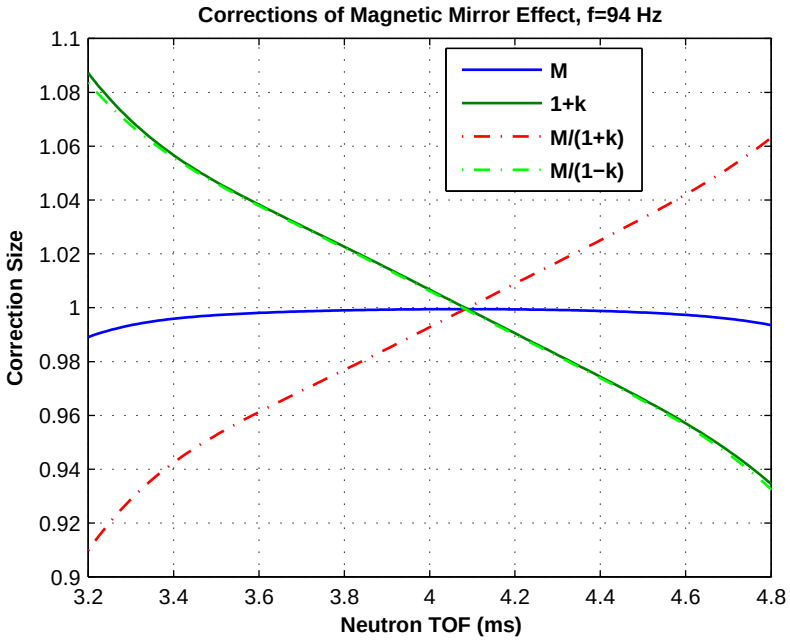

Figure 4.13: Simulated quantities of M and $1 + k$, and the corrections $M/(1 \pm k)$ versus the TOF of the n-pulse in decay volume.

Chapter 5

Data Analyses and Preliminary Results

In this chapter, we introduce the analyses of the experimental data, and the physical effects in the measurement, including the backscattering effect, time structure of signals and magnetic mirror effect.

The practical and technical effects and systematic errors of the experiment are not discussed in this dissertation. These effects include that from n-beam, background, detector and electronics system, as listed in table 5.1.

Category	Source of Error	Category	Source of Error
Neutron	Neutron Polarization P	Detector	Detector Calibration
	Spin Flipper Efficiency F		e^- Position Dependency
	Neutron Flux Φ Fluctuation	Electronics	Electronics Dead Time
Background	Beam Line Background		Measuring Gate Time
	Beamstop 2nd Background		Electronics Time Drift
	External Background	Systematic	B-field Measurement

Table 5.1: List of the technical and systematic errors.

In the last section, we provide a preliminary result of the correlation A from the PERKEOIII experiment in 2008-2009, and derive the Axial-vector Vector coupling ratio λ. The systematic effects and errors are not considered in the analyses, and the results only include the statistic errors. For more information and detailed data analyses, please refer to the Ph.D. dissertation of Dr. Holger Mest [Mes11] and later publications.

5.1 Backscattering Effect off Scintillator Detector

During the interactions with the scintillator, the electrons have probabilities to be scattered out from the scintillator after several times collisions, so called as the *backscattering effect*. The backscattered electrons only deposit parts of their energies on the detector, hence distort the measured spectrum.

The probability of backscattering is a function of the electron energy and the incident angle, as shown in figure 5.1.

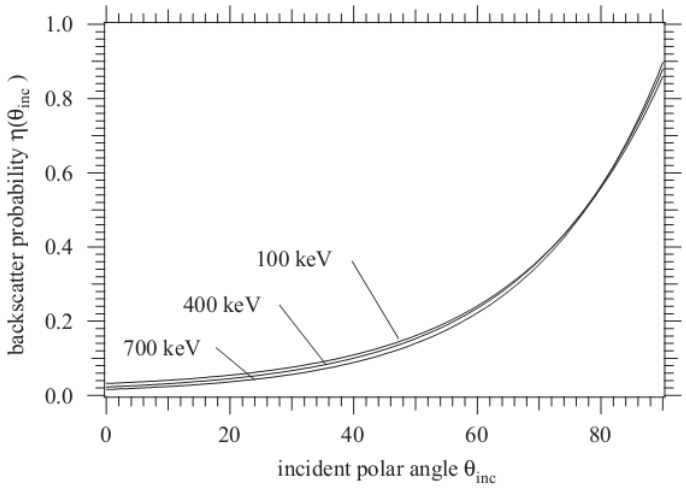

Figure 5.1: The backscattering probability of electron off scintillator as a function of energy and incident angle. Figure is from [Wie05].

As discussed in Section 4.3.1, the magnetic field of PERKEOIII can limit the electron incident angles below 47° at the detectors, hence reduces the backscattering probability below 18%.

A beneficial property of PERKEOIII is the symmetric layout of the two detectors. If the backscattered electrons are emitted from one detector with emergence angles larger than 47°, they will be reflected by the magnetic field in decay volume back to the original detector. The energies of the first incoming and the reflected backscattered signals will be summed up and recorded as one event. If the scattered electrons have the emergence angle less than 47°, they can be guided by the magnetic field to the opposite detector.

In the electronics system, if one of the two detectors is triggered by an incoming electron, both detectors will be activated. Each detector will integrate the energies of all received signals during a time period of t_{gate}=220 ns. If the electron is backscattered from one detector then reach another one, its energy can be measured by the other detector. Figure 5.2 plots the TOF diagram of the backscattered electrons from one detector to the opposite one, and the energy spectrum of them.

The energies of the backscattered electrons should be considered in the derivation of electron spectra. Figure 5.3 shows the electron energy spectra with and without the energy contribution from the opposite detector.

5.2 Time Windows Selection

The time window for $S(E)$ is chosen when the n-pulse is inside the effective decay volume. The neutron density distributions versus time are determined in simulation. Figure 5.4 plots the simulated neutron distributions at different time, with chopper frequency as 83 Hz and 94 Hz.

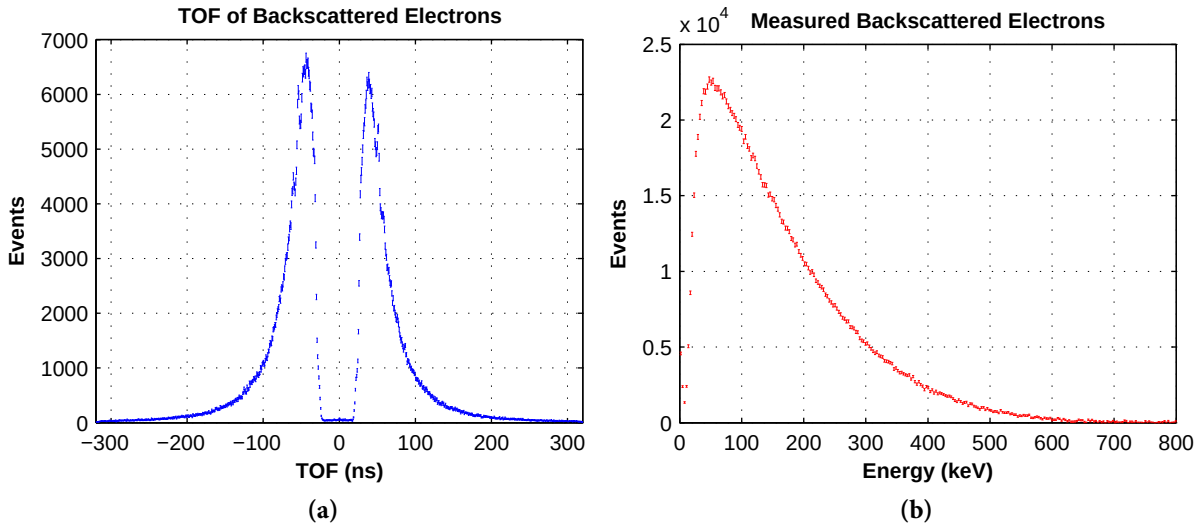

Figure 5.2: **(a)** The TOF diagram of the backscattered electrons from one detector to the other. The original detector is triggered at t=0, the diagram represents the time when the opposite detector receives the backscattered electrons. The positive time denotes the electron scattered from Detector 1 to Detector 2, and negative time denotes the reverse direction. **(b)** Energy spectrum of the backscattered electrons which reach the opposite detector.

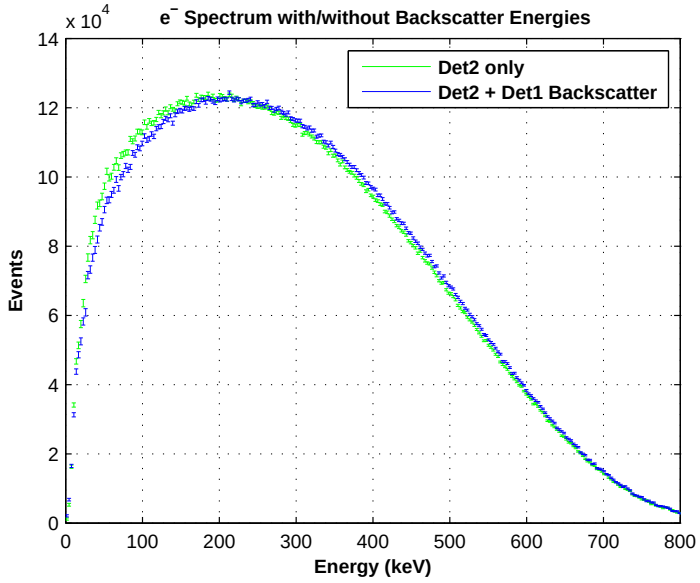

Figure 5.3: The electron energy spectrum measured by a single detector (green), and the spectrum including the backscatter energy contribution from the other detector (blue).

As shown in figure 5.4, the neutron are completely in the 2.5 m effective decay volume during a period of 1.4 ms, which can be chosen for $S(E)$ time windows. The centers of the time windows are 4.1 ms and 4.0 ms for 83 Hz and 94 Hz chopper frequencies respectively.

The time windows for $B(E)$ are chosen after the neutrons are totally absorbed. Whereas

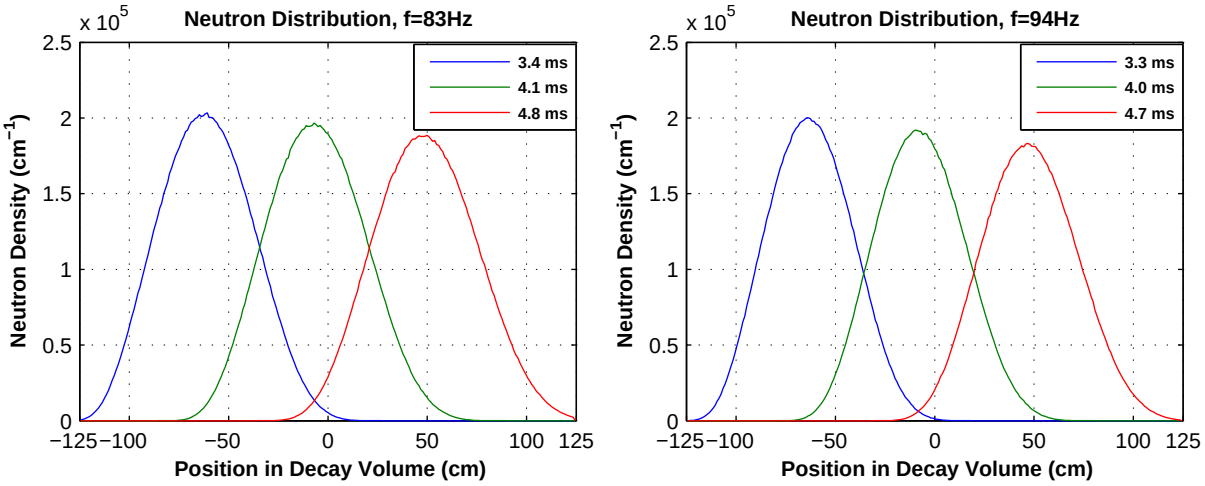

(a) 83 Hz **(b)** 94 Hz

Figure 5.4: The simulated neutron distribution in the decay volume at different time, for 83 Hz and 94 Hz chopper frequencies. The zero position means the center of the decay volume. Please note the length of the n-pulse expands during propagation.

the neutron beamstop can generate secondary neutrons, which will decay and contribute signals to the background measurements, as introduced in Section 3.3.7. To suppress this influence, the $B(E)$ time windows in the cycle are chosen as late as possible.

Since the event rate of $S(E)$ is about twice as that of $B(E)$, the time period of $S(E)$ is also chosen twice as $B(E)$ to get the lowest error [Kno10]. Table 5.2 summarizes the time windows for the $S(E)$ and $B(E)$ selections.

	$S(E)$	$B(E)$
83 Hz	3.4 ms~4.8 ms	11.2 ms~11.9 ms
94 Hz	3.3 ms~4.7 ms	9.85 ms~10.55 ms

Table 5.2: The selections of the time windows for $S(E)$ and $B(E)$, with chopper frequency as 83 Hz and 94 Hz.

5.3 Determination of Magnetic Mirror Effect Corrections

For a measurement in a time interval Δt, the corrections of magnetic mirror effect should be integrated

$$A_{exp}^{Det1,2} = \frac{\int_t^{t+\Delta t}\int_V \left[N^{\uparrow}(t,\mathbf{r}) - N^{\downarrow}(t,\mathbf{r})\right] \mathrm{d}\mathbf{r}^3\mathrm{d}t}{\int_t^{t+\Delta t}\int_V \left[N^{\uparrow}(t,\mathbf{r}) + N^{\downarrow}(t,\mathbf{r})\right] \mathrm{d}\mathbf{r}^3\mathrm{d}t} = \frac{A\beta}{2}\frac{\int_t^{t+\Delta t} M(t)\mathrm{d}t}{\int_t^{t+\Delta t}\left[1 \pm k(t)\right]\mathrm{d}t} \tag{5.1}$$

The total corrections on Detector 1 and Detector 2 during the $S(E)$ measurement can be calculated:

$$f^{83Hz}_{Det1,2} = \frac{\int_{3.4\text{ ms}}^{4.8\text{ ms}} M(t)_{83Hz}\mathrm{d}t}{\int_{3.4\text{ ms}}^{4.8\text{ ms}} [1 \pm k(t)_{83Hz}]\,\mathrm{d}t}, \quad f^{94Hz}_{Det1,2} = \frac{\int_{3.3\text{ ms}}^{4.7\text{ ms}} M(t)_{94Hz}\mathrm{d}t}{\int_{3.3\text{ ms}}^{4.7\text{ ms}} [1 \pm k(t)_{94Hz}]\,\mathrm{d}t} \tag{5.2}$$

The values of the integrated corrections are listed in table 5.3. As shown in the table, the $(1-f)$ is less than 10^{-2}.

5.4 Electron Asymmetry Derivation and Preliminary Results

With the time windows in table 5.2, we select the events for signal $S(E)$ and background spectra $B(E)$, with the ratio of time windows as T_s/T_{bg}=2. In the derivation of spectra, the energies of backscattered electrons E_{bs} are included. The pure electron energy spectra $N(E)$ are given as

$$N^{\uparrow,\downarrow}(E) = S^{\uparrow,\downarrow}(E + E_{bs}) - 2B^{\uparrow,\downarrow}(E) \tag{5.3}$$

The measured $S(E)$ and $B(E)$ spectra are shown in figure 4.6. The resulted $N^{\uparrow,\downarrow}(E)$, as well as the sum and difference of the spectra are plotted in figure 5.5.

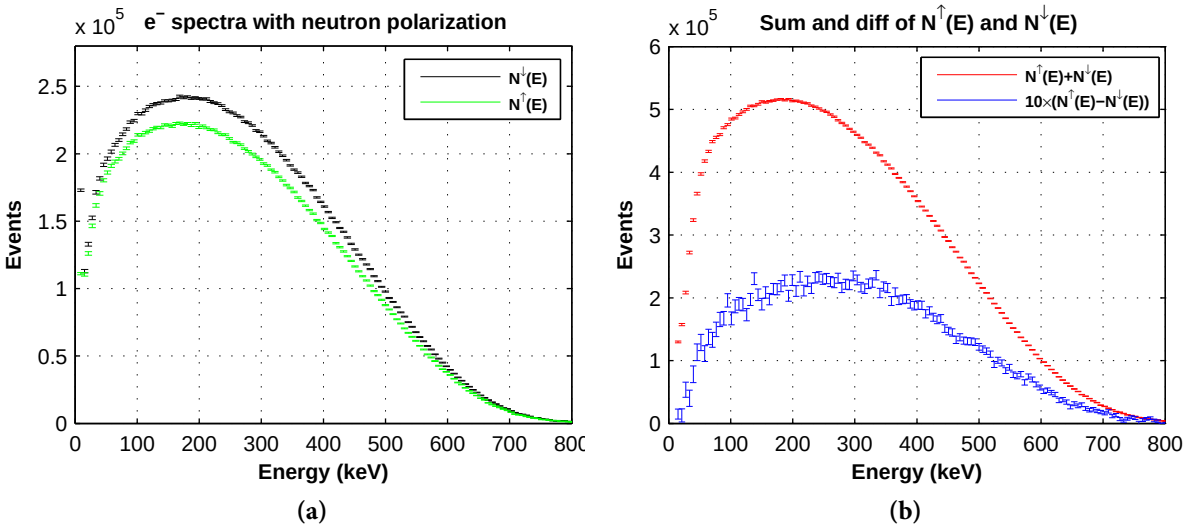

Figure 5.5: (a) The electron energy spectra $N^{\uparrow}(E)$ and $N^{\downarrow}(E)$. **(b)** The sum $N^{\uparrow}(E)$+$N^{\downarrow}(E)$ and the difference $N^{\uparrow}(E)$-$N^{\downarrow}(E)$ of the spectra. Data are measured by Detector 2, with chopper frequency as 94 Hz.

The experimental asymmetry A_{exp} can be derived

$$A_{exp}(E) = \frac{N^{\uparrow}(E) - N^{\downarrow}(E)}{N^{\uparrow}(E) + N^{\downarrow}(E)} = \frac{1}{2} A\beta f \tag{5.4}$$

with f the mirror effect correction, which depends on the neutron properties and $S(E)$ time window. The relative velocity β can be represented by the electron kinetic energy E_k

$$\beta = \frac{v}{c} = \sqrt{1 - \frac{E_0}{E_k + E_0}}, \quad \text{with} \quad E_0 = m_0 c^2 = 511 \text{ keV} \tag{5.5}$$

To obtain the value of A, we apply eqn. 5.4 and 5.5 to fit the measured $A_{exp}(E)$. Figure 5.6 shows the derived $A_{exp}(E)$ and the fitting curve [1].

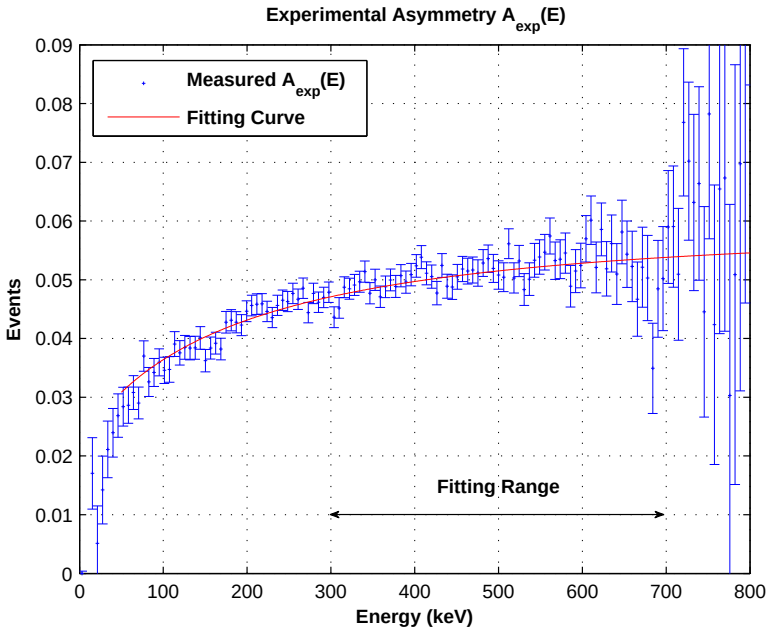

Figure 5.6: The measured A_{exp} from Detector 2, and the fitting curve (red) according to eqn. 5.4 and 5.5.

The fitting range is chosen in 300 keV~700 keV, in which the relation between the ADC channels and the real energies can be considered as linear, as shown in figure 3.19. The detector *gain* and *offset* are chosen as 32.6 keV/ch and 1255 ch, that are obtained from the calibrations with three β sources [Mes11].

The results of A, and the mirror corrections f are listed in table 5.3.

Take the average of the results, the A has a value of

$$A = -0.12132(19) \tag{5.6}$$

[1] The values of $N^{\uparrow}(E)$-$N^{\downarrow}(E)$ and A_{exp} are negative. Here we use their absolute values for convenience.

Frequency	Detector	$A \cdot f$	χ^2	Correction f	A
83Hz	Det1	-0.12156(41)	6.64	0.99319	-0.12239(42)
83Hz	Det2	-0.12068(37)	5.54	1.00292	-0.12033(37)
94Hz	Det1	-0.11933(39)	4.75	0.99172	-0.12032(39)
94Hz	Det2	-0.12281(37)	6.08	1.00487	-0.12222(37)

Table 5.3: Preliminary results of the β-asymmetry A and mirror effect corrections f.

According to eqn. 2.16, the derived λ is

$$\lambda = \frac{-1 - \sqrt{1 - 3A^2 - 2A}}{3A + 2} = -1.28037(51) \tag{5.7}$$

This results are only preliminarily analysed. The polarization of the neutrons P, as a blind factor, is not considered. Additionally, most of the systematic errors are not included, and the background estimation is not optimized. But solely from the statistic point of view, the value of A is 5.8 times more precise, and the value of λ is 4.9 times more precise than the latest value as shown in table 2.2.

Chapter 6

PERC: A Clean, Bright and Versatile Source of Neutron Decay Products

PERKEOIII experiment has been successfully performed in the 2008-2009 beam time of ILL. The final results of electron angular correlation coefficient A, as well as the ratio of Axial-vector and Vector coupling strengths λ, are expected to be 5 times more precise than the latest results (Section 5.4). However, from the experience in working with PERKEOIII, we also see the opportunities of improving the system in later experiments. After PERKEOIII was performed for the first time in 2007, the design of a new system for neutron β-decay measurement was initiated, named as PERC (Proton and Electron Radiation Channel), and firstly proposed in [Dub08].

The motivation of PERC is to investigate the spectra of electrons and protons (e^-/p^+) and the angular correlation coefficients in the β-decays of free cold neutrons, also to perform measurements of different kinds of observables. In order to achieve expected systematic effects, the PERC instrument needs to be well and delicately designed.

The main part of the author's doctoral work, is designing the PERC magnet system, studying the behaviours of the magnetic field and the e^-/p^+particles, investigating and optimizing the systematic effects of the instrument.

The instrument of PERC is going to have an unprecedented 8 m long decay volume, which can supply the event rate of decay e^-/p^+on the order of 10^5. A series of superconducting magnets will be used to generate a well designed magnetic field for guiding and processing the charged e^-/p^+particles. With the well defined field distribution and detection system, the distortions of the measured e^-/p^+spectra and the angular coefficients are expected to be suppressed on the level of 10^{-4}.

In addition, the PERC system is designed not only as a spectrometer, but also a beam station of neutron decay products. The PERC instrument is able to export an intense e^-/p^+-beam, which can be used in different measurements with various physical motivations. Depending on the desired observables, it is possible to apply types of the detectors or spectrometers for post processing and measurements at the end of PERC (Section 6.5). The high statistics and the magnetic field system of PERC can realize the measurements of the observables with high precisions.

The precise measurements of the neutron decay in low energy scales are complementary to the researches in high energy experiments, and supply us the opportunities to test the

Standard Model and its extensions. As introduced in Section 2.3, some of the new symmetry concepts and the physical quantities that are excluded from the Standard Model are able to be derived from the neutron decay observables. These possible new physics may indicate the supersymmetries, the exotic particles and interactions, and unification of the forces, which are at the forefront area of the particle physics and cosmology.

The experiments of PERC will be performed at the neutron beam facility *Mephisto* of the Forschungs-Neutronenquelle Heinz Maier-Leibnitz (FRMII) in Munich of Germany [Zei06]. With the supermirror n-guide, Mephisto can supply neutrons with capture flux of 2×10^{10} $cm^{-2}s^{-1}$ [Bae08].

The PERC project is developed by an international collaboration of the University of Heidelberg, the Vienna University of Technology, the Institute of Laue-Langevin, the University of Mainz, and the Technical University of Munich.

In this chapter, we provide an overview of PERC, including its principles, properties, and possible systematic problems.

6.1 Principles of PERC System

The PERC instrument mainly consists of three parts: the 8 m long *decay volume vessel* for the neutron decay and e^-/p^+ collection, the *selector vessel* for e^-/p^+ decoupling and the pitch angle selection, and the *detector vessel* for magnetic field reduction and e^-/p^+ detection. A set of superconducting coils are located in the three vessels and supply a high magnetic field. A sketch of the PERC instrument is shown in figure 6.1.

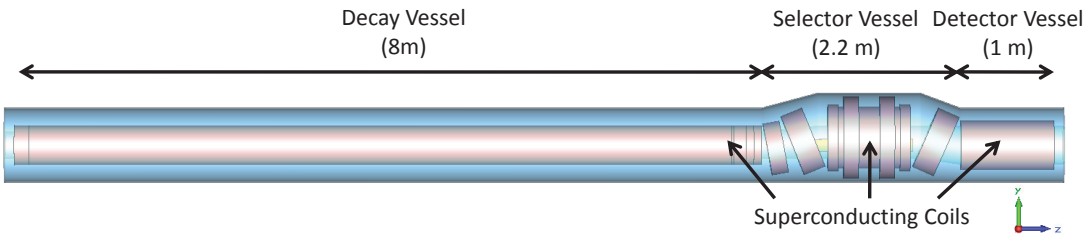

Figure 6.1: Plot of PERC instrument. The red parts denote the superconducting coils between the inner bore and outer wall.

The decay volume vessel and the detector vessel, as well as the coils inside them are located coaxially, assumed along the z-axis. The selector vessel has a larger diameter, and the vessel center is 8 cm higher than the other two vessels. The whole instrument shows a dromedary geometry, with a total length of 11.2 m.

The main mechanisms of PERC have similarities as the PERKEOIII and previous PERKEO instruments. The cold neutrons from the reactor are imported to the decay volume, and part of them decay into charged e^-, p^+ and $\bar{\nu}_e$. The magnetic field inside the decay volume holds the neutron spin states and collects the decay e^-/p^+ due to their gyration motions.

The rest neutrons propagate through the decay volume, then are absorbed by the beamstop located in the selector vessel.

In the selector vessel, there are three tilted coils on both sides to provide a curved magnetic field from the decay volume to the detector vessel. The e^-/p^+-beam from the decay volume are decoupled from the n-beam, and guided by the curved magnetic lines to fly over the neutron beamstop. After the beamstop, they are guided back to the central axis, then projected to the detectors. Figure 6.2 shows the principle of PERC, and the trajectories of $e^-/p^+$and neutrons.

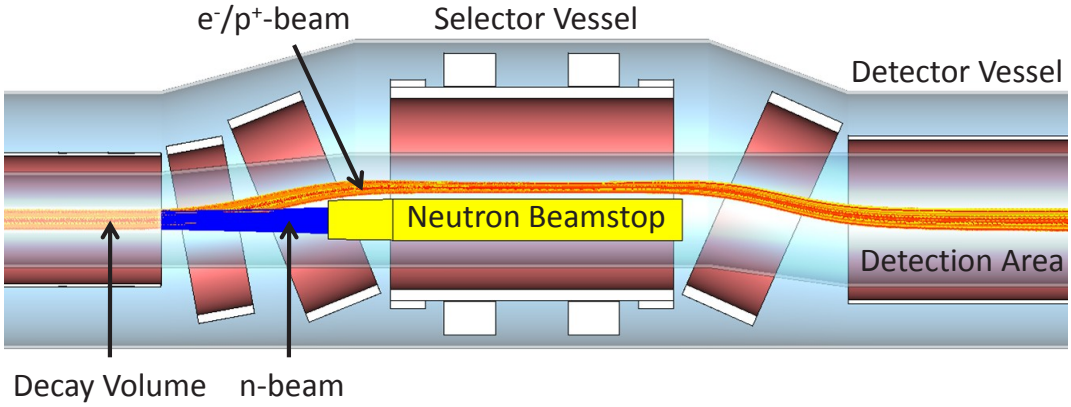

Figure 6.2: Sketch of the PERC principle, and the simulated trajectories of $e^-/p^+$and neutrons.

In the detector vessel, the analysing apparatuses and detection systems can be applied for the processing and measurements of e^-/p^+particles.

Compare with the precursor instruments, PERC has new features which enhance the systematic effects, including the defined decay volume in the neutron guide and the specified magnetic field distribution.

6.2 Active Decay Volume Inside Neutron Guide

To apply a long decay volume as in PERC, the n-beam cross-section expansion caused by the beam divergence need to be avoided.

The large n-beam cross-section may lead to problems in the experiments:

- The too large n-beam profile may cause the collisions of neutrons or $e^-/p^+$with the inner wall of the instrument, which can generate long-term background signals or distortion of e^-/p^+spectra.
- In the large n-beam, the magnetic fields experienced by neutrons have larger deviations. The calculations of the magnetic mirror effect will be less accurate (Section 4.4).

- The e^-/p^+-beam size is enlarged by the n-beam. To obtain high statistics, large e^-/p^+ detectors are required, which then cause systematic errors, e.g. the position dependences of the scintillator detector.

In case of PERC that has 8 m long decay volume, we will apply a non-depolarizing neutron guide (n-guide) inside the superconducting solenoid as the active decay volume. The n-guide has $m = 2$ supermirrors coated on the inner walls. When the neutrons from the reactor are introduced into the n-guide, they can be confined in the n-guide with little loses (Section 3.3.1). Therefore, the systematic errors related to the n-beam cross-section are minimized, and the neutrons in the decay volume experiences a homogeneous magnetic field, which can suppress the magnetic mirror correction to 10^{-3} (Section 7.3.3).

The n-guide in PERC supplies an active decay volume of $6\times6\times800$ cm^3, which can supply extremely high decay rates as 10^6 s^{-1} (Section 6.6, [Dub08]).

Practically, the supermirror can absorb a little fraction of the incident neutron. Figure 6.3 shows the simulated neutron flux along the $m = 2$ n-guide. After the 8 m long n-guide, totally 3.86×10^9 neutrons are absorbed per second, that account for 1.4% of all input neutrons.

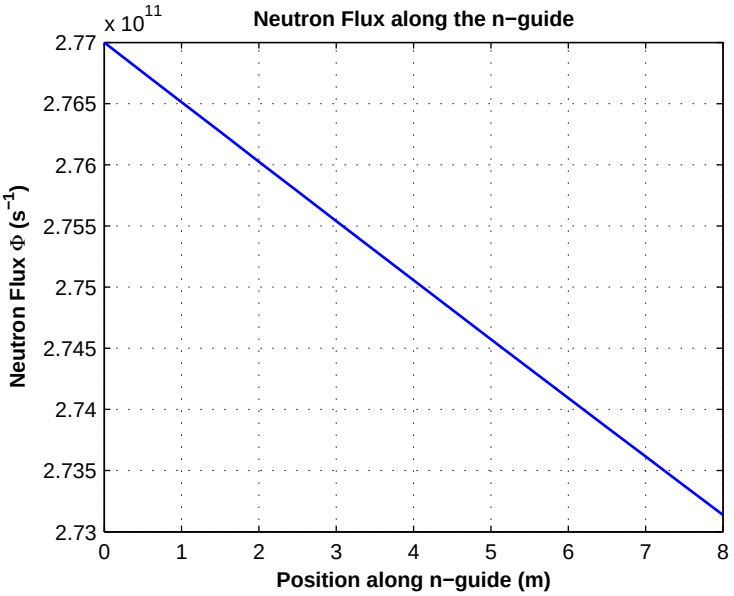

Figure 6.3: The simulated neutron (real) flux along the z-direction of n-guide. The n-guide has $m = 2$ supermirrors, and the reflectivity R_0 is assumed as 99%. The neutron source is same as introduced in Section 3.3.1. Assuming there are no neutron losses between the source and the n-guide.

Besides the advantages, the n-guide also causes systematic problems:

- *Neutron absorption and related background.*

  The neutron absorption of n-guide does not significantly influence the neutron density or the decay rate, but will generate considerable 3.86×10^9 Hz γ background. The

γ-rays from the n-guide normally have 0.5 MeV and 6~9 MeV energies, that are emitted from Boron glass and Ni layer respectively. For a 100% efficient detector with the size of 10×10 cm^2, and located 3.18 m distant from n-guide, the γ-ray background of 8.64×10^4 Hz will be received.

- *N-beam background in time scale.*

  The n-beam related background is always present during the collection of signals. We cannot compare the signal and the background for every cycle in the pulsed beam mode, as it was done in PERKEOIII experiment.

- *Edge effect.*

  The decay e^-/p^+ in the n-guide may have collisions with the guide when they are emitted close to the inner wall of the n-guide, so called as the *edge effect*. The collisions will cause the absorption of e^-/p^+, or changes on their energies or emission angles, thus lead to the distortion of the measured e^-/p^+ spectra and angular distributions.

The first and the second background problems can be highly suppressed by the specific dromedary geometry and the neutron beamstop. As shown in figure 6.2, the neutron beamstop is located in the 2.1 m long selector vessel. The selector vessel can accommodate pieces of thick Pb bulks behind the neutron absorber sheets, to attenuate the γ-rays from the reactor site, the decay volume, and the neutron absorption sheet. The detector directly behind the neutron beamstop thus can be well shielded. Assuming the Pb bulk has a thickness of 1 m, the 0.5 MeV and 6~9 MeV γ-rays can be suppressed by 10^{60} and 10^{20} respectively [HS95]. Theoretically, the total γ background including that from the beamstop can be reduced below 10^{-10} Hz.

To reduce the errors from the edge effect, we decrease the collision probability by applying a high magnetic field, further use an e^-/p^+-window at the detection area to absorb the distorted signals (Section 7.3.2).

Since the coated suppermirror on the Boron glass substrate of the n-guide cannot surfer low temperature, the warm bore will be applied inside PERC.

6.3 High Magnetic Field Supported by Superconducting Magnets

The PERC instrument will apply a high magnetic guiding field supported by a series of superconducting magnets. The application of high magnetic field can suppress the systematic errors of the aspects:

- *e^-/p^+ gyration radius and n-guide edge effect.*

  The probability of the collision between the e^-/p^+ and the n-guide is related to the gyration radii, the pitch angles and the emission positions of e^-/p^+ particles. The high

magnetic field can efficiently decrease the e^-/p^+ gyration radii, thus can suppress the n-guide edge effect.

- *e^-/p^+-beam size.*

  The e^-/p^+-beam cross-section is also decreased with the gyration radii. Together with the n-guide, the profile of the e^-/p^+-beam is kept smaller than 10×10 cm^{-2} at the detection area. Small detectors can be applied for measurements, thus the errors e.g. caused by detector position dependencies can be minimized.

- *Non-adiabatic transport.*

  As shown in eqn. B.2, the adiabatic condition of particle transports is easier to be fulfilled in high magnetic field. The large magnetic field gradient around the field barrier B_1 (figure 6.4) will not distort the pitch angles of e^-/p^+.

- *Drift effects.*

  According to eqn. B.11, the drift effects caused by field curvatures can be suppressed in high magnetic field.

6.4 Specified Magnetic Field Distribution

The geometry and the strength of the magnetic guiding field in PERC are specifically designed with a functional distribution, which can realize more efficient and accurate measurements.

From eqn. 3.1 and figure 3.1, it is seen that the β-asymmetry is more obvious around the direction of neutron spin state $\langle\boldsymbol{\sigma}_n\rangle$ and the opposite direction. Namely the electrons emitted with small pitch angles according to the magnetic lines have more information of the correlation A. By choosing the signals with emission angle ranges, the measurements can obtain a higher efficiency.

In PERC, the selection of e^-/p^+ emission angles is realized by the magnetic mirror effect, which is achieved by the specified magnetic field distribution. Figure 6.4 shows the magnetic field strength along the e^-/p^+-beam in PERC.

The 8 m long solenoid outside the n-guide can supply a homogeneous magnetic field of B_0 = 1.5 T. Behind the decay volume, the coils in the selector vessel generate a high magnetic field barrier of B_1 = 6 T. When the decay electrons propagate from B_0 to B_1, both the e^-/p^+ gyration radii and the e^-/p^+-beam cross-section shrink according to the adiabatic invariant in eqn. B.4. Besides, the longitudinal momenta of e^-/p^+ are converted to the transverse component, and the particles will be reflected back when their pitch angles increase to 90°.

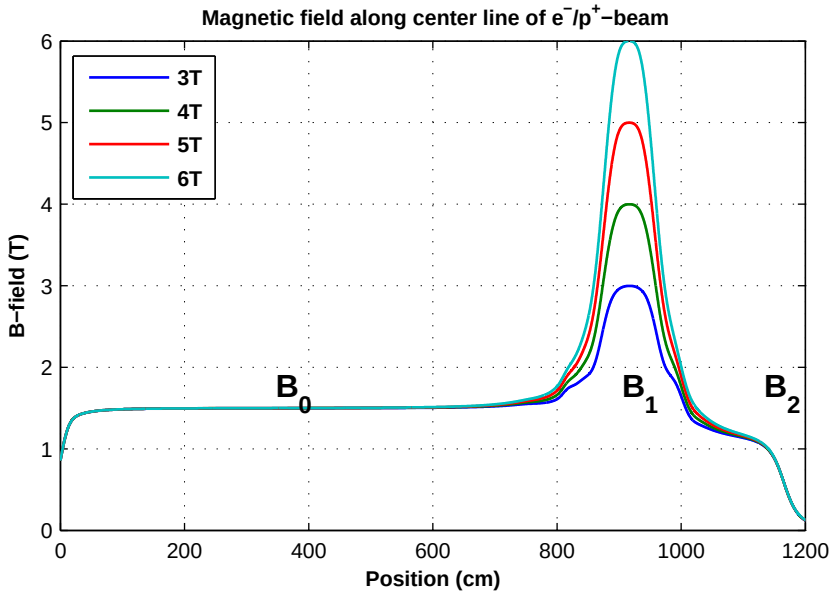

Figure 6.4: The magnetic field strength along the e^-/p^+-beam in PERC. The decay volume has a homogeneous magnetic field of B_0 = 1.5 T. The coils in the selector vessel generate a high magnetic field barrier B_1 between 3 T and 6 T. After the selector coil, the field is decreased to B_2 = 0.5 T at the detection area.

Thus the high magnetic field B_1 acts as a magnetic mirror, that allows only the electron with emission angle θ_0 smaller than the critical angle θ_c at B_0 to pass. The critical angle from eqn. B.7 is written as:

$$\theta_0 \leqslant \theta_c = \arcsin\sqrt{\frac{B_0}{B_1}} = \arcsin\sqrt{\frac{1.5\ \mathrm{T}}{6\ \mathrm{T}}} = 30^{\mathrm{o}} \tag{6.1}$$

After the selector vessel, the field decreases adiabatically to B_2 = 0.5 T at the detection area. The pitch angles of electrons are then decreased below

$$\theta_{det} \leqslant \arcsin\sqrt{\frac{B_2}{B_1}} = \arcsin\sqrt{\frac{0.5\ \mathrm{T}}{6\ \mathrm{T}}} = 16.8^{\mathrm{o}} \tag{6.2}$$

and the e^-/p^+-beam cross-section is increased to

$$S_{det} = S_{dec} \cdot \frac{B_0}{B_2} = 6 \times 6\ \mathrm{cm}^2 \cdot \frac{1.5\ \mathrm{T}}{0.5\ \mathrm{T}} = 10.4 \times 10.4\ \mathrm{cm}^2 \tag{6.3}$$

With the angle selection, the received signals are defined by θ_c

$$N^{\uparrow} = \int_0^{\theta_c} W(\theta)\sin\theta \mathrm{d}\theta \qquad N^{\downarrow} = \int_{\pi-\theta_c}^{\pi} W(\theta)\sin\theta \mathrm{d}\theta \tag{6.4}$$

and the experimental β-asymmetry A_{exp} becomes

$$A_{exp}(E) \equiv \frac{N^{\uparrow}(E) - N^{\downarrow}(E)}{N^{\uparrow}(E) + N^{\downarrow}(E)} = \frac{1}{2}A\beta(E)P(1+\cos\theta_c) = \frac{1}{2}A\beta(E)P\left(1+\sqrt{1-\frac{B_0}{B_1}}\right) \tag{6.5}$$

with $\beta = v_e/c$, and P the polarization of the neutrons. Compare with eqn. 3.4, the value of A_{exp} can be increased by a factor of $(1 + \cos\theta_c)$, while the event rate is decreased by $(1 - \cos\theta_c)$. This effect is also valid for the proton asymmetry measurement.

Additionally, the selector field B_1 is designed to be variable between 3 T to 6 T, hence θ_c and the related effects are able to be tuned in the experiment. Figure 6.5 shows the systematic effects as functions of the magnetic field ratio B_0/B_1 and B_2. [1]

With the specified magnetic field distribution, we are able to gain the benefits in the measurements:

- *More efficient events.*

  The collected signals with small emission angles have more information about e^-/p^+ asymmetry. We can obtain more efficient events in the measurement.

- *Suppressed backscattering effect.*

  The maximal e^-/p^+pitch angles at the detector are less than 25°. As shown in figure 5.1, the backscattering probabilities of the electrons are less than 6%, which is 2.5 times smaller than that in PERKEOIII.

- *Backscattered signal measurement.*

  Since $B_2/B_1 \ll 1$, most of the backscattered particles off the detector can be reflected by B_1 back to detector, and their rest energies can be measured. The backscattered e^-/p^+which can pass B_1 account for 8.7% and 4.3% of the total backscattered signals, corresponding to 3 T and 6 T selector field.

- *Less sensitivity to field homogeneity.*

  The magnetic mirror makes the A_{exp} less sensitive to the deviations of the fields B_0, B_1, compare to the case without the mirror $B_0/B_1 = 1$, in which case the sensitivity diverges to infinity, as shown in figure 6.5 **(e)** and eqn. 7.2. The B_0 and B_1 inhomogeneity will induce less errors.

- *Event rate limitation.*

  PERC can supply a large decay rate on 10^6 s^{-1} order, but the electronics for detection nowadays can hardly reach this level. Further, the event rate is too large for the measurements with single-count mode. The selection of emission angle can keep the event rates under an acceptable limit.

- *Adjustable pitch angle selection.*

  With different selector field B_1 between 3 T and 6 T, we are able to investigate the dependencies of the observables with the e^-/p^+emission angles.

Table 6.1 summarizes some parameters with B_1 from 3 T to 6 T.

[1] The merit of a measurement NA_{exp}^2 is a quantity inversely proportional to the statistic error for a certain measuring time, hence also inversely proportional to the measuring time to reach a certain error [Kno10].

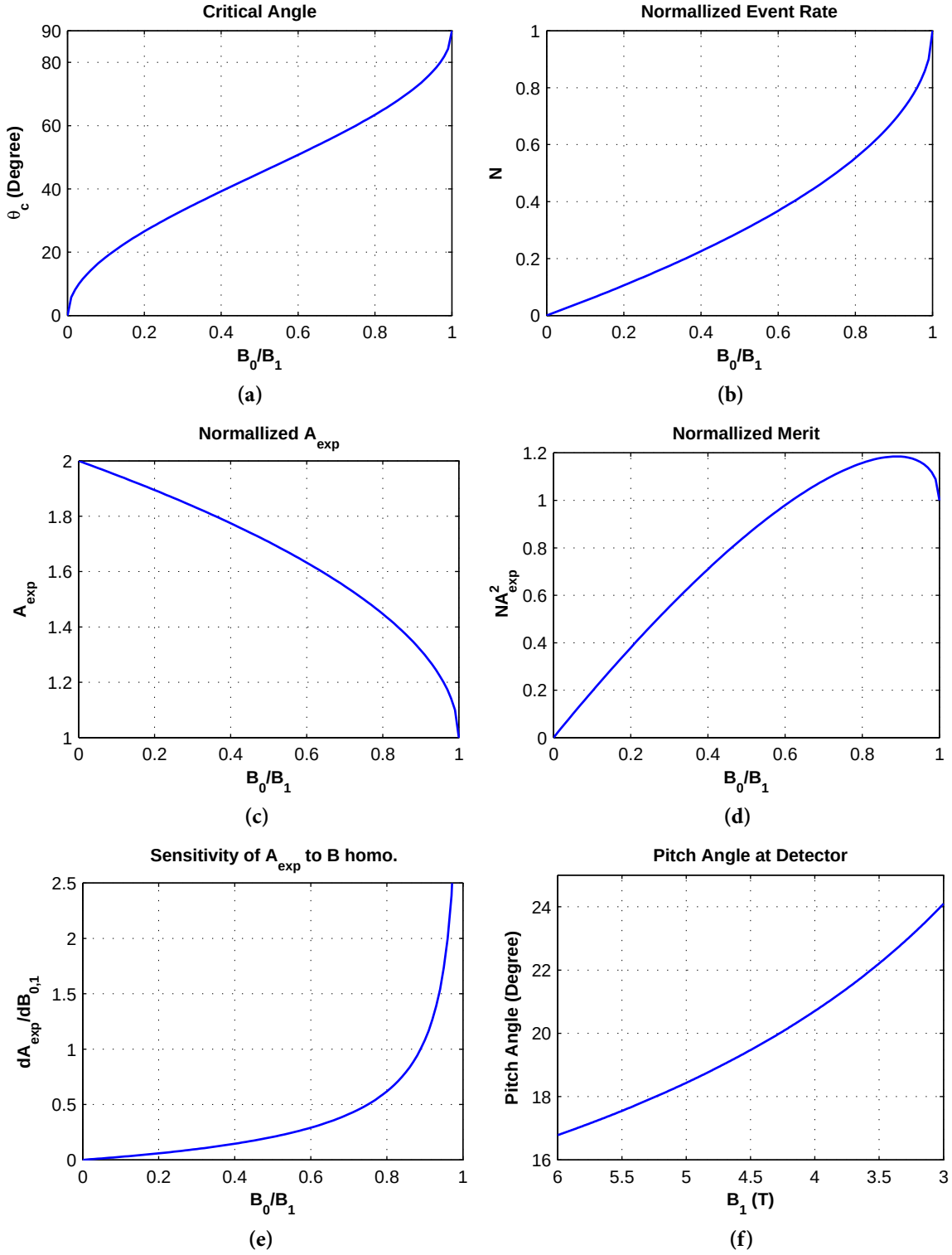

Figure 6.5: The effects of the magnetic mirror on the measurements. The plots show the dependencies of magnetic field ratio B_0/B_1 with **(a)** the critical angle θ_c; **(b)** the event rate N received by the detector; **(c)** the experimental asymmetry A_{exp}; **(d)** the measurement merit NA^2_{exp}; **(e)** the sensitivity of A_{exp} to B_0, B_1 homogeneity. **(f)** The maximal pitch angle at the detector vs. B_1 field. The values of N and A_{exp} are normalized by the case with no mirror effect, i.e. $B_0/B_1 = 1$.

B_1	Critical Angle θ_c	Pitch Angle at Detector θ_{det}	A_{exp} Magnification	Relative Event Rate	Loss of Backscat. e^-/p^+
3 T	45.0°	24.1°	1.71	29.3%	8.7%
4 T	37.8°	20.7°	1.79	20.9%	6.5%
5 T	33.2°	18.4°	1.84	16.3%	5.1%
6 T	30.0°	16.8°	1.87	13.4%	4.3%

Table 6.1: Some parameters with B_1 variation. The *Relative Event Rate* is the event rate relative to the case without magnetic mirror B_0/B_1=1. The *Loss of Backscat.* e^-/p^+ denotes the fraction of the backscattered e^-/p^+ that pass B_1 barrier, assuming the backscattered signals are isotropically emitted from the detector.

6.5 Detection Methods and Measurable Quantities

At the end of PERC system, various spectrometers for electron and proton measurements can be applied. Figure 6.6 sketches some possible spectrometers, the measurable observables, and the derived quantities.

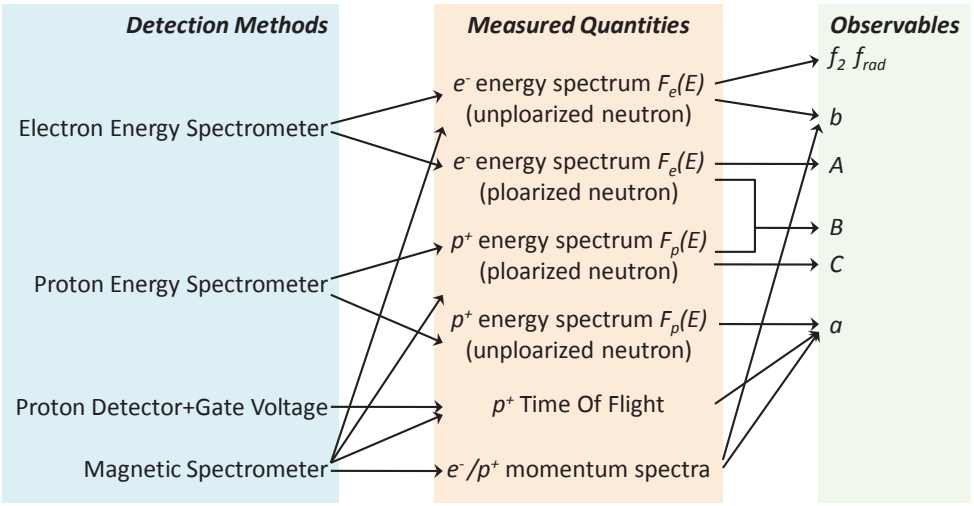

Figure 6.6: Sketch of the detection methods, the measurable and derivable observables.

With the direct observed e^-/p^+ spectra and other observables, the coefficients a, b, A, B and R can be derived, further more quantities can be deduced from them, as introduced in Chapter 2.

6.6 Event Rate Estimation

If assume the neutron source has the capture flux of $\Phi_c = 2\times10^{10}$ cm^{-2}s^{-1}, and 20% of the neutrons are lost between the source and the n-guide [Dub08], the total decay rate inside

the n-guide is

$$N_{decay} = \frac{L_{decay}}{v_0 \tau} \cdot \Phi_c \cdot S_{n\text{-}guide} \cdot 80\% = 2.38 \times 10^6 s^{-1} \tag{6.6}$$

with the length of the decay volume L_{decay} = 8 m, the most probable velocity v_0 = 2200 m/s, the neutron life time τ = 880.1 s, and the n-guide cross-section $S_{n\text{-}guide}$ = 6×6 cm^2. By applying the selector field B_1, and the e^-/p^+-window that has the projection of 5×5 cm^2 in n-guide (Section 7.3.2), the event rate received by the detector is

$$N = N_{decay} \cdot \frac{1}{2} \frac{S_{e^-/p^+\text{-}window}}{S_{n\text{-}guide}} \left(1 - \sqrt{1 - \frac{B_0}{B_1}}\right) \tag{6.7}$$

Table 6.2 lists the expected event rates of e^-/p^+signals with continuous (Cont.) and pulsed (Pulse.) n-beam, unpolarized (Unpol.) and polarized (Pol.) n-beam

B_1	Cont. Unpol.	Cont. Pol.	Pulse. Unpol.	Pulse. Pol.
3 T	2.42×10^5	4.84×10^4	1.21×10^4	2.42×10^3
4 T	1.73×10^5	3.46×10^4	8.65×10^3	1.73×10^3
5 T	1.35×10^5	2.70×10^4	6.75×10^3	1.35×10^3
6 T	1.11×10^5	2.21×10^4	5.54×10^3	1.11×10^3

Table 6.2: Estimation of the event rates in PERC with continuous and pulsed, polarized and unpolarized n-beam, and with various B_1 field.

In the pulse n-beam mode, we assumed the $S(E)$ time window is 1/3 of one cycle period. Together with the operations of the velocity selector and the chopper, the event rate is reduced by about 20 (Section 3.3). One supermirror polariser can reduce rate by factor of 5 (Section 3.3.3, additionally considering the polariser window as 8×8 cm^2, and the PERC n-guide cross-section 6×6 cm^2).

Chapter 7

Magnetic Field System of PERC

The magnetic field inside PERC is the essential and the main element of the experiment. As introduced in Chapter 6, the magnetic field has functions of holding the neutron spins, collecting and guiding the e^-/p^+ particles to the detectors, selecting and adjusting the e^-/p^+ pitch angles. Hence the properties of the magnetic field in PERC are strongly related to the systematic effects and errors. In order to obtain optimized experiment performance, the magnetic field system and the e^-/p^+ trajectories in PERC are carefully designed and studied with different kinds of simulations (Appendix C).

7.1 Requirements to Magnetic Field System

Generally, the magnetic field system of PERC should satisfy requirements from physics, mechanics and systematics points of view:

- The systematic errors of the experiment should be reduced as small as possible. The field system should limit the distortion of e^-/p^+ properties on the level of 10^{-4}.
- The system should be available for different kinds of post spectrometers with various physical motivations. And the post spectrometers should not cause defects of system functions.
- To avoid possible defects of the instrument in practice, the functional magnetic fields B_0, B_1, B_2 should be variable to some extend from the nominal values, without causing systematic defects.
- The properties of the magnetic field should have tolerances on some unexpected factors, e.g. errors in manufacturing, external magnetic field, influences from non-linear magnetic shielding material.
- The instrument should be mechanically stable under the strong magnetic forces from the coils and the magnetic shielding.
- The geometry of the system should fit the related elements, e.g. n-guide, vacuum pump, mechanical supports, thermal insulation of cryostat and the hall of Mephisto beam line.

- The superconducting coil system is expected for a long term use without quenching of magnets, leakages of cryogen or failure of cooling.

The PERC collaboration has taken the aspects listed above into the consideration, and determined the dromedary geometry of the magnets, as introduced in Chapter 6. Compare with other designs, the dromedary geometry has the advantages and the disadvantages:

Advantages:

- *Background shielding.*
  The γ background from n-beam can be well shielded by the beamstop in the selector vessel (Section 6.2).
- *Easier construction.*
  The system has a relative simple structure, which is easier for construction and causes less possible problems in cryogenics.
- *Mechanical stability.*
  The magnetic forces between coils are mainly in the z-direction. The system can be more stable under the strong forces.
- $\boldsymbol{R}\times\boldsymbol{B}$ *drift effect.*
  The symmetric layout relative to the selector coil minimizes the $\mathbf{R}\times\mathbf{B}$ drifts of e^-/p^+.

Disadvantage:

- *Real time neutron polarization.*
  The real time neutron polarization measurement during e^-/p^+ detection is difficult to be realized since the e^-/p^+-beam is coaxial to the n-beam in the detection area.
- *Field influences.*
  The selector coils have large diameters, hence the high magnetic field B_1 significantly influences the field of decay volume B_0, the detection area B_2 and the post spectrometers. The influences cause inhomogeneities of the other fields, and induce relative larger corrections of the magnetic mirror effect.
- B_1 *homogeneity.*
  Since the coils in selector vessel are located higher than other coils, it is difficult to control the homogeneity of B_1, and
- e^-/p^+*-beam shifts.*
  The vertical positions of the e^-/p^+ beam changes with B_1.

Under the frame of dromedary geometry, we need to define the configurations of the coils in detail, as well as minimize the adverse effects. To ensure the expected performances of PERC, the technical characters of the magnetic field are required:

- *Prevention of magnetic local minima.*
  The local minima of the magnetic field along the e^-/p^+-beam and n-beam must be avoided as far as possible. The field minima can trap the charged particles and contribute continuous distorted signals, as presented in Section B.3.

- *Enough separation distance.*
  The e^-/p^+-beam in the selector vessel should be separated with enough distances from the n-beam to place the neutron beamstop. Considering the beam profiles and room for shielding, the distance between e^-/p^+-beam and n-beam centers is required larger than 10 cm.

- *Minimized e^-/p^+ collisions.*
  The e^-/p^+-beam should have no collisions with the inner walls of the warm bore. The collisions between $e^-/p^+$and n-guide, i.e. the edge effect should be minimized and well studied.

- *Field homogeneity.*
  The fields B_0 and B_1 for the e^-/p^+pitch angle selections must be homogeneous. The corrections caused by field ratio B_0/B_1 need to be lower than 1.4×10^{-2} for continuous n-beam mode.

- *Variable selector field.*
  The selector field B_1 should be variable between 3 T and 6 T to adjust the critical angle θ_c, without influencing the functions of the system.

- *Adiabatic transport*
  The non-adiabatic transport that changes the e^-/p^+pitch angles should be minimized.

- *Mechanic and geometry requirements.*
  The coils need enough space between each other for necessary mechanic supports and cooling system.

Taking all factors above into consideration, we provide a design of the magnets system with 13 coils.

7.2 Magnets System of PERC

7.2.1 Decay coil

The 8 m long *decay coil* outside the n-guide supplies the magnetic field B_0 for the decay volume.

The n-guide has outer cross-section of 8×8 cm^2. In the radial direction outside the n-guide, we need around 10 cm for the mechanic supports of the guide, and 5 cm for the thermal insulation of the cryostat. Taking these factors, we set the radius of decay coil as 20 cm. The geometry and the cross-section of the decay vessel are plotted in figure 7.1.

At the end of the decay volume, the magnetic field decreases and the field local minimum can appear. On the decay coil, we apply three correction coils with positive and negative currents to adjust the field in small ranges, hence avoid the local minima on the n-beam and e^-/p^+-beam, also homogenize the B_0 field over the decay volume. Technically, these

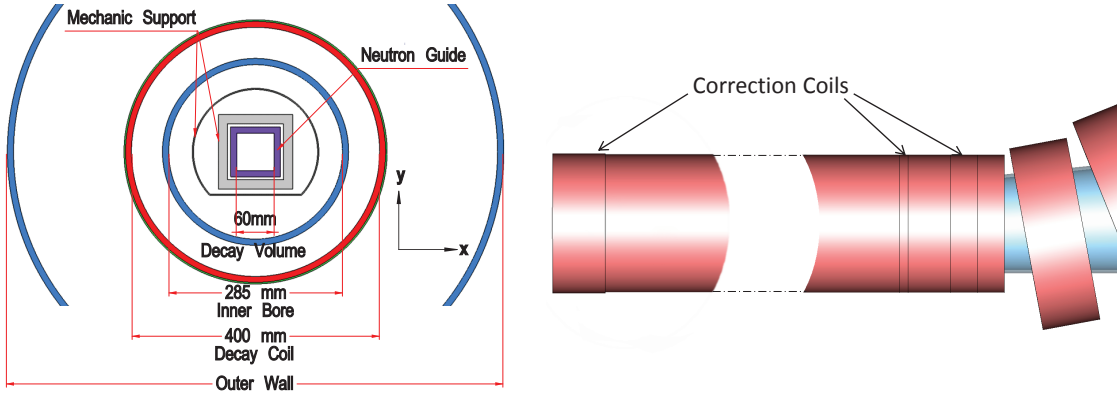

(a) n-beam **(b)** e^-/p^+-beam

Figure 7.1: (a) The plot of the cross-section of the decay volume vessel. **(b)** Sketch of the side view of the decay coil.

correction coils can be realized by simply adding or removing some winding layer from the solenoid.

7.2.2 Bending coils

After the decay volume, we use two tilted *bending coils* to curve the magnetic lines and decouple the e^-/p^+-beam from the n-beam.

To reduce the overlapped area of e^-/p^+- and n-beam (Section 7.3.1), the bending coils should separate the e^-/p^+-beam efficiently, i.e. have large tilt angles. On the other hand, the discrete tilted coils can cause field minima between them. We delicately adjust the geometry and parameters of the coils, and apply the correction coils both on decay coil and selector coil. The magnetic field on the e^-/p^+- and n-beams can be smoothly increased from the decay volume to the selector vessel, as plotted in figure 7.2.

7.2.3 Selector coils

The coils in the selector vessel are used to generate the magnetic field barrier B_1, that filters e^-/p^+according to their emission angles. Figure 7.3 sketches the geometry of these coils.

The 88 cm long solenoid in the vessel named as *selector coil* can supply a field of 3 T. The two correction coils at both ends of selector coil are used to avoid the field minima at the joints of the coils, also to homogenize the B_1 field.

The variation of B_1 is achieved by the two coils outside the selector coil, named as *filter coils*, which are supplied by an individual power. By adjusting their current from 0 A to 612 A, B_1 can be tuned between 3 T and 6 T. The filter coils also act as a pair of Helmholtz coils, which can keep the B_1 homogeneity below 1.6×10^{-4} level in the e^-/p^+-beam cross-section (Section 7.3.3).

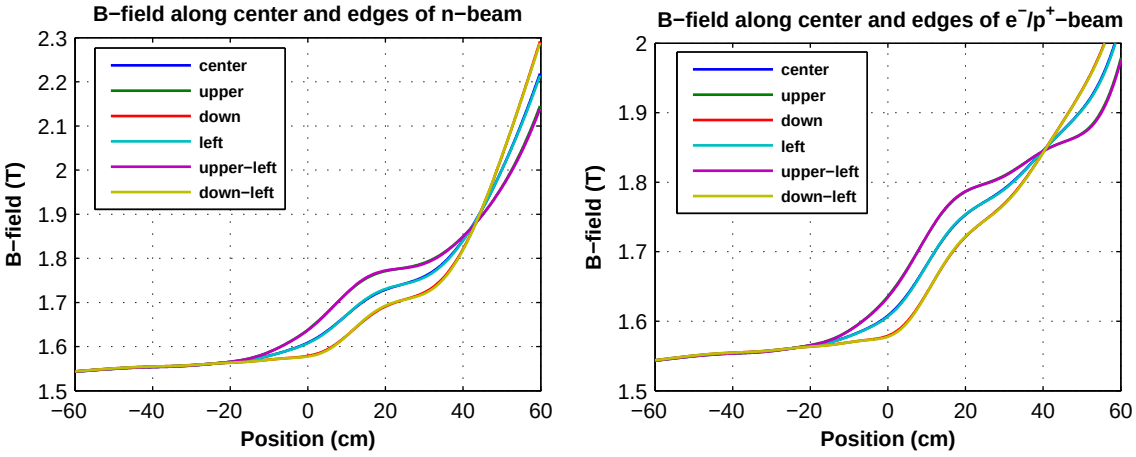

(a) n-beam **(b)** e^-/p^+-beam

Figure 7.2: The magnetic field strength along the **(a)** n-beam and **(b)** the e^-/p^+-beam in the bending coils. Different curves denote the field strengths along the central lines and the edges of the beams. The zero point means the end of the n-guide. B_1 is set as 3 T, the n-beam is assumed to have 2° divergence.

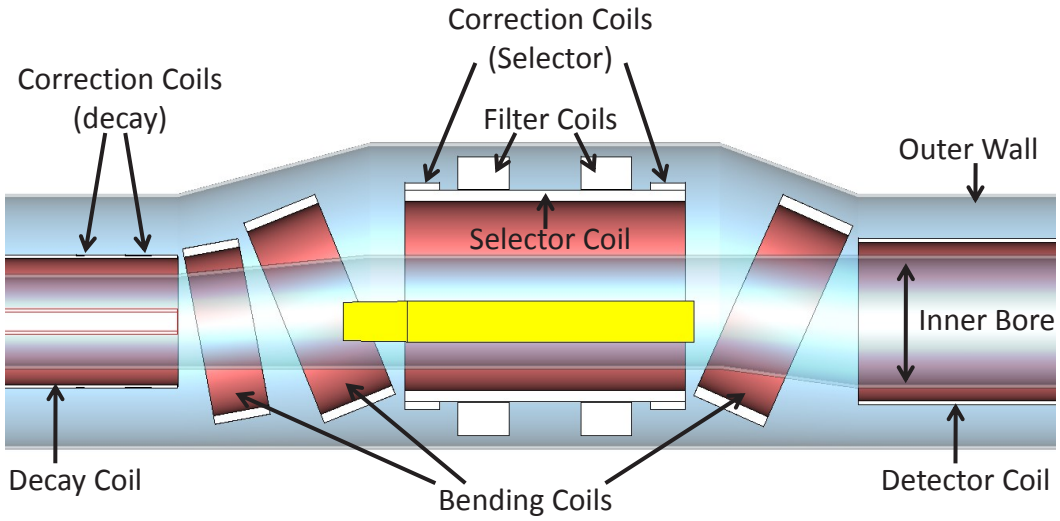

Figure 7.3: Sketch of the coils inside the selector vessel.

7.2.4 Detector coil

After the selector coil, the third bending coil guides the e^-/p^+-beam back to central axis of decay coil, behind the beamstop. A 1 m long *detector coil* is then applied to decrease the magnetic field gradually to the low field B_2. In the detector coil, the processing apparatuses e.g. the static electrodes, and the spectrometers e.g. election scintillator or silicon detectors, proton detectors can be applied.

For an easy and reliable industrial manufacture, we firstly build up the superconducting magnets system, as well as the related mechanic supports and the cooling system. The

inner warm bore can be produced separately, and afterwards inserted into the magnets from the open end at the detector coil. This procedure requires that the cross-section of the inner bore in detector vessel must be larger than that in selector vessel and decay vessel, as sketched in figure 7.3. In order to avoid the interactions between the e^-/p^+ and the inner bore, enough space between them has to be left.

As discussed in Section 7.3.1, the maximal distance of e^-/p^+ is 14 cm from the n-beam center. We set the radius of detector coil as 25 cm, and the inner radius of the warm bore inside detector vessel can be 20 cm. In this case, at least 5 cm distance between e^-/p^+ and the bore can be assured. Additionally, the inner wall of the warm bore will be polished and coated with gold to minimize the electrical forces on the protons.

7.2.5 Parameters of coils

Altogether, there are 13 coils in the magnets system, including 6 solenoids and 7 correction coils outside of them. The detailed technical parameters of the magnets are summarized in Appendix D and table D.1.

For the reasons of manufacture, experiment and security, we use 4 power supplies for the magnet system.

The decay coil has a large length, and supplies a relative low magnetic field. The current of it can be high to reduce the superconductor windings. The bending coils and the selector coil produce and experience high magnetic fields, hence the current of these coils is set lower to avoid magnetic quenching (Section 8.1.2). The filter coils are used to tune B_1 between 3 T and 6 T, thus need an individual power supply with variable current. The detector coil can also use an adjustable power supply to vary B_2 field and the e^-/p^+ pitch angles at the detector.

With the 4 individual power supplies, we are able to change the functional magnetic fields separately to fulfill different measurements. Also, they are sufficient to avoid the unexpected magnetic field defects during the experiment, e.g. field minima and external field influences. Every power supply has an individual security system to damp the currents when quenching occurs (Section 8.1.2).

7.3 Properties of Magnetic Field and e^-/p^+ Trajectories in PERC

7.3.1 Properties of e^-/p^+ trajectories with B_1 variation

The coils in selector vessel are located 8 cm higher than the decay and detector coil, so the trajectories of e^-/p^+ particles also change with the B_1 variation.

Decoupling distance.

The e^-/p^+-beam is decoupled from the n-beam in the bending coils. The distance from the end of the n-guide to the *separation point* where the e^-/p^+-beam is totally separated from the n-beam, is defined as the *decoupling distance*, as sketched in figure 7.4.

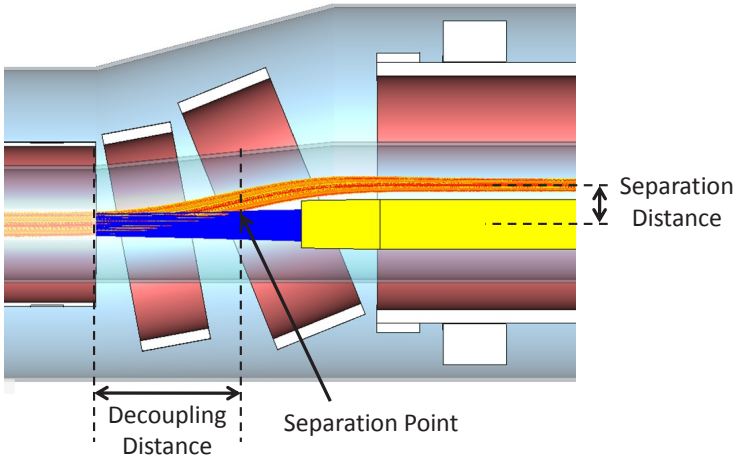

Figure 7.4: Trajectories of e^-/p^+ and neutrons in the bending coils. The e^-/p^+ are emitted from the middle of the decay volume.

The decoupling distance is necessary for the parameter determinations:

- *The corrections on B_0.*

  The decay signals from the overlapped area of e^-/p^+-beam and n-beam in the decoupling distance also contribute to the measurements (in continuous n-beam mode). Whereas the magnetic field in bending coils is higher than 1.5 T, hence the correction of decay field B_0 gets large when decoupling distance is long.

- *The geometry of the neutron beamstop.*

  The beamstop and the connected γ shielding have to be placed after the separation point. And the beamstop should fit the size of the n-beam, which is enlarged outside the n-guide due to the beam divergence.

Systematically, the decoupling distance should be as short as possible. Besides, as discussed in Section 7.2, the field local minima on the e^-/p^+-beam and n-beam need to be avoided.

The decoupling distances as shown in table 7.1 are from 41.21 cm to 41.53 cm. If assume the divergence of the n-beam out from the n-guide is 2°, the resulted n-beam cross-section is 8.9×8.9 cm^2 at the separation point.

Separation distance.

The distance from the e^-/p^+-beam center to the n-beam center in the selector coil is defined as *separation distance*, as shown in figure 7.4. The separation distances are required to be larger than 10 cm to accommodate the neutron beamstop and the related γ shielding.

In the dromedary layout, the variation of B_1 changes the vertical position of e^-/p^+-beam in the selector coil. Figure 7.5 shows the simulated distributions of the electrons in the cross-section of the selector coil, when B_1 is set as 3 T and 6 T.

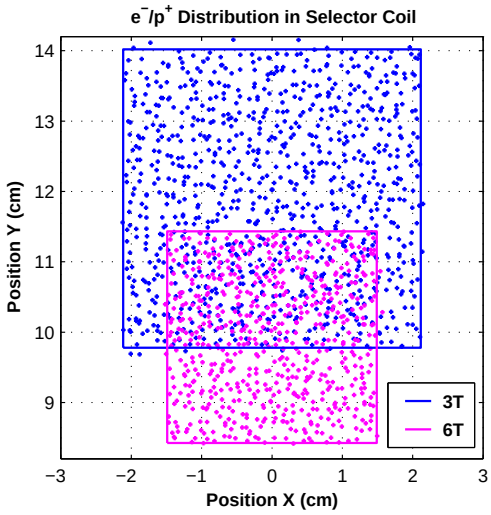

Figure 7.5: The profiles of the e^-/p^+-beams in the cross-section of the middle of the selector coil, with the B_1 field as 3 T and 6 T. The spots denote the e^-/p^+distribution simulated by CST Studio, and the frames denote the profiles of magnetic lines initiated from decay volume simulated by magfield.c. The zero point is the central axis of the decay coil.

From the simulation, the e^-/p^+-beam center is in the range from 9.93 cm to 11.90 cm, and total beam is in the range from 8.43 cm to 14.02 cm relative to the n-beam central line. The separation distances are needed for the calculation and the optimization of the B_1 homogeneity (Section 7.3.3).

e^-/p^+ trajectories at the n-guide end.

Beside the position in the selector coil, the e^-/p^+-beam in the n-guide is also influenced by the B_1 field. Figure 7.6 shows the magnetic line distributions at the end of the n-guide.

As shown in figure 7.6, the e^-/p^+-beam center is shifted by -0.8 mm and +2.8 mm at the end of n-guide, for B_1 as 3 T and 6 T. The overlaps of the magnetic lines and the n-guide indicate the collisions of e^-/p^+particles, which lead to the edge effect.

Table 7.1 summarizes the e^-/p^+-beam properties relative to different selector field B_1.

7.3.2 Edge effect of n-guide and active e^-/p^+window

Active e^-/p^+-window.

As introduced in Section 6.2, the n-guide edge effect, i.e. the collision of e^-/p^+particles with the n-guide inner wall will cause absorption and distortion of the signals. To shield the

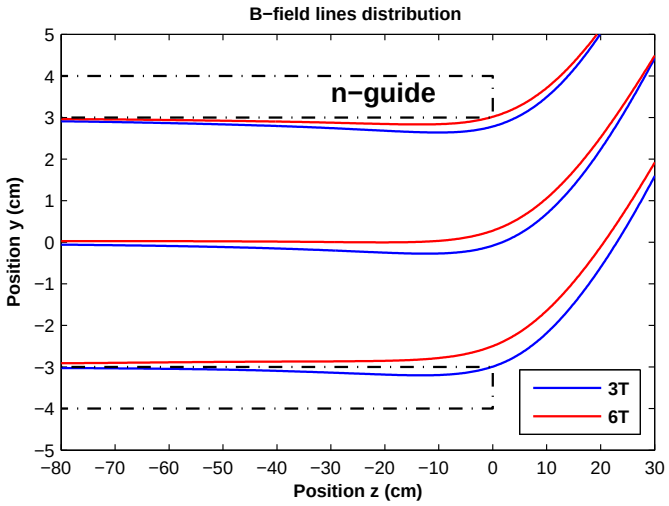

Figure 7.6: The side view of the magnetic line distributions at the end of n-guide, for the selector field B_1 as 3 T and 6 T. The magnetic lines are initiated from the middle of n-guide, and stand for the profile of the e^-/p^+-beam.

B_1	Decoupling Distance	Max. B-field in Decoupling	e^-/p^+ Position at Guide End	Separation Distance	e^-/p^+ Size at Selector
3 T	41.21 cm	1.83 T	-0.8 mm	11.90 cm	4.23×4.24 cm^2
4 T	41.26 cm	1.99 T	0.5 mm	10.99 cm	3.66×3.68 cm^2
5 T	41.49 cm	2.16 T	1.7 mm	10.37 cm	3.27×3.30 cm^2
6 T	41.53 cm	2.32 T	2.8 mm	9.93 cm	2.98×3.01 cm^2

Table 7.1: Properties of the e^-/p^+-beam in PERC with B_1 variation. The third column denotes the maximal magnetic field in the overlapped area.

distorted signals, we apply an e^-/p^+-window at the detection area, as sketched in figure 7.7 **(a)** [1].

However, the application of the e^-/p^+-window will cause the signal distortions on the second order:

- *e^-/p^+ penetration.*

  To avoid the collisions with the window edges, the thickness of the e^-/p^+-window has to be much smaller than the helical pitches of the charged particles. Whereas the e^-/p^+ then have probabilities to penetrate the window, and reach the detector.

- *Backscattering off the e^-/p^+-window.*

  When the e^-/p^+ hit the window, they have probabilities to be backscattered, and most of them can be reflected back by B_1. Due to the helical motion, the reflected e^-/p^+ have probabilities to fly over the window and reach the detector.

[1] If the e^-/p^+-window is sufficiently thin, it does not change the angular distributions of the particles.

- *Backscattering off the detector.*

  The backscattered $e^-/p^+$from the detector have probabilities to hit the e^-/p^+-window from outer side, or be reflected by B_1 then hit the window from inner side. The backscattered energies are lost.

The second order effects will contribute 10^{-2} to 10^{-3} events relative to the total signals [Dub08]. To suppress the distortions, we can use the *active* e^-/p^+-window with the single-count mode measurements. The active e^-/p^+-window can be made by plastic scintillator material, and connected with photomultiplier tubes, as sketched in figure 7.7 **(a)**.

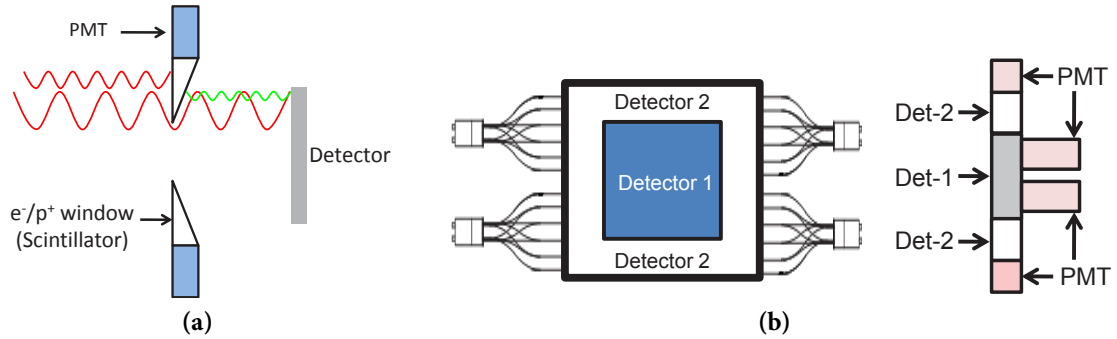

Figure 7.7: (a) Principle of the active e^-/p^+-window. The window is made by scintillator material, and connected with photomultiplier tubes (PMT). The signals from active window are set anti-coincident to the measurement. **(b)** A method of the composited detector system. Both of the detectors can be Silicon or scintillator detectors.

When the electrons hit the e^-/p^+-window, it can output signals, which are set anti-coincident to the measurements of the detectors. Once there is an event from the window, the measured results from e^-/p^+-detector in a time period are abandoned.

Another easier solution could be combining the active e^-/p^+-window and the detector together, as shown in figure 7.7 **(b)**. The *Detector-1* in the center is used for signal measurement, the *Detector-2* outside measures the abandoned signals. Both of the detectors can be Silicon or Scintillator detectors. In the composite detector system, the e^-/p^+penetration problem and the direct cross talk between the two detectors can be avoided. Furthermore, this structure should be more easier for construction. With the same principle, the specialized Silicon detector with position resolution can also be used.

By applying active e^-/p^+-window, the second order distortion can be suppressed by factor of 5 [Dub08].

Determination of e^-/p^+-window size.

In the 1.5 T decay volume, the maximal gyration radius of e^-/p^+which can pass through the B_1 field is

$$r_{max} = \frac{p_{max}}{eB_0} \sin\theta_c = \frac{p_{max}}{eB_0}\sqrt{\frac{B_0}{B_1}} = 1.87 \text{ mm} \tag{7.1}$$

considering the critical angle $\theta_c = 45^o$ caused by the lowest selector field $B_1 = 3$ T.

To avoid the distorted signals, all of the e^-/p^+ particles whose gyration centers have distances less than r_{max} from the n-guide inner wall should be shielded. Therefore the e^-/p^+-window projection at the decay volume should be at least d = $2r_{max}$ = 3.73 mm distant from the n-guide. Taking a security factor, we take the distance as d = 5 mm, which results in the 5×5 cm^{-2} projection in decay volume, and should be sufficient for 3 T to 6 T B_1 field.

To determine the e^-/p^+ window, we study the magnetic lines distributions inside PERC. The magnetic lines can stand for the tracks of the gyration centers of the charged particles, if the particles are transported adiabatically, and the drift effects are negligible (Appendix B). In the calculation, we count in the critical magnetic lines, whose nearest distance to the n-guide inner wall is 5 mm. The critical magnetic lines thus can denote the projections of the e^-/p^+ window.

As introduced above, the B_1 field variation influences the e^-/p^+-beam in the n-guide and detector, hence also changes the positions and the sizes of the e^-/p^+ window. Table 7.2 lists the dimensions of the areas defined by the critical magnetic lines in n-guide and detector, with the selector field B_1 in 3 T to 6 T range. The detector is 318 cm from the n-guide end, and has a B_2 field as 0.5 T.

B_1	Dimension in Decay	y-Pos. in Decay	Dimension in Detector	y-Pos. in Detector	Event Loss	Event Loss Common
3T	49.8×47.5 mm^2	1.2 mm	87.3×83.0 mm^2	-0.3 mm	5.5%	8.8%
4T	49.8×48.7 mm^2	0.6 mm	86.5×84.3 mm^2	-0.6 mm	3.0%	7.0%
5T	49.8×49.8 mm^2	0.1 mm	85.7×85.3 mm^2	-0.8 mm	1.0%	5.2%
6T	49.8×49.0 mm^2	-0.3 mm	84.9×83.1 mm^2	-0.9 mm	2.5%	3.4%

Table 7.2: Dimensions of the e^-/p^+-window projection in decay volume and the detector. *y-Pos.* denotes the vertical positions of the window centers from the central axis of decay coil. *Event Loss* means the relative data losses compare to the ideal 5×5 cm^2 window. *Event Loss Common* denotes the relative losses when using a common e^-/p^+-window.

If we do not change the e^-/p^+-window when applying different B_1 fields, we need a *common e^-/p^+ window* for all B_1 cases. The common window should be the overlaps of all windows listed in the table. As a result, the common window at the detector has the size of 84.9×82.4 cm^2, and the vertical position of -0.6 mm. The *Event Loss 2* in the table 7.2 denotes the data losses when applying the common window, relative to the ideal 5×5 cm^2 window.

It is necessary to note that, the d⩾5 mm criterion is only taken in the range between -4 m to 0 m relative to n-guide end in the calculation, since edge effect caused by the beginning of the n-guide is more difficult to be shielded.

As shown in figure 6.4, the magnetic field at the beginning of decay volume is low, hence the magnetic lines spread in this range. Figure 7.8 plots the magnetic line distributions at the beginning of the n-guide.

The distorted e^-/p^+ from the beginning part of n-guide will be condensed and guided by the magnetic lines to the central region of the e^-/p^+-beam. The signals from the *contamination*

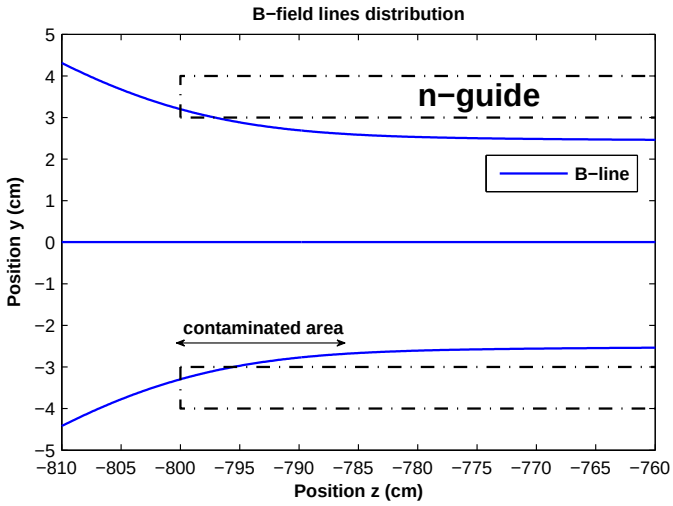

Figure 7.8: The distribution of the magnetic lines at the beginning of the decay volume. The e^-/p^+particles distorted by the n-guide can be guided to the central region of the e^-/p^+-beam.

area as shown in figure 7.8 are difficult to be shielded by the e^-/p^+-window. In continuous n-beam mode, the contributions of the distorted signals account for 4.3×10^{-3} and 2.1×10^{-3} of the total events for 3 T and 6 T B_1 respectively.

The magnetic field at the guide beginning is 0.85 T. If we shield all distorted signals, the e^-/p^+window needs to be at least 3.25×3.25 cm^2 in the n-guide, and the event rates will be further decreased by a factor of 2.4. Another solution to achieve a better shielding is using pulse n-beam mode, with which the signals can be selected in the time scale.

7.3.3 Magnetic field homogeneity

The homogeneities of the magnetic fields B_0 and B_1, which are used for the e^-/p^+selection due to their emission angles, directly influence the measurements related to the angular distribution. In this section, we discuss the influences of B_0 and B_1 homogeneities on β-asymmetry measurement. For other angular distribution measurements, the effects will show the same or similar properties.

By applying the magnetic mirror B_0/B_1, the sensitivities of the measured asymmetries to the field homogeneity is efficiently decreased, as shown in figure 6.5 **(e)**. From eqn. 6.5, the deviations of A_{exp} induced by B_0 and B_1 deviations are

$$\left.\frac{\Delta A_{exp}}{A_{exp}}\right|_{B_1} = -\frac{\sin^2\theta_c}{2\cos\theta_c(1+\cos\theta_c)}\frac{\Delta B_0}{B_0}, \quad \left.\frac{\Delta A_{exp}}{A_{exp}}\right|_{B_0} = \frac{\sin^2\theta_c}{2\cos\theta_c(1+\cos\theta_c)}\frac{\Delta B_1}{B_1} \tag{7.2}$$

with the field homogeneity and $\Delta A_{exp}/A_{exp}$ defined as the relative deviations from the values in standard configuration

$$\frac{\Delta B_{0,1}}{B_{0,1}} = \frac{B - B_{0,1}}{B_{0,1}}, \quad \frac{\Delta A_{exp}}{A_{exp}} = \frac{A_{exp} - A^0_{exp}}{A^0_{exp}} \tag{7.3}$$

B_1 homogeneity.

As the highest field experienced by the e^-/p^+ particles, the selector field B_1 is required to be homogeneous in the cross-section of the e^-/p^+-beam at the middle of the selector coil. For this purpose, two correction coils and two filter coils are applied outside the selector coil.

However, as listed in table 7.1, the shifts of the e^-/p^+-beam position in the selector coil due to B_1 variations introduce considerable difficulties on the optimizations of the field homogeneity. In this case, the position of e^-/p^+-beam must be same as the position of the most homogeneous area (i.e. the field minimum in x-y plane) in the selector coil, when B_1 is changing from 3 T to 6 T.

In the dromedary geometry, the three bending coils generate a minus gradient of magnetic field along the y-direction. Together with the contribution of the filter coils, both the field minimum and the e^-/p^+-beam are shifted down when B_1 increases. By delicately adjusting the lengths, positions, radii and windings of the coils, we try to synchronize the two shifts as well as possible. Figure 7.9 plots the relative B_1 deviations in the x-y plane at the middle of the selector coil, for B_1 as 3 T and 6 T.

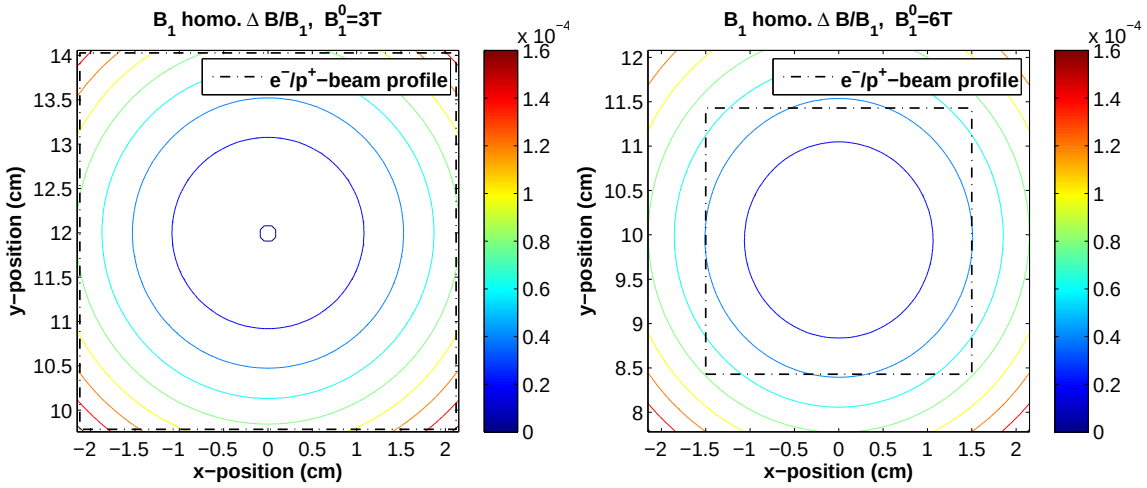

(a) 3 T **(b)** 6 T

Figure 7.9: The contour plots of the B_1 relative deviations in the x-y plane at the middle of the selector coil, for B_1 equals 3 T and 6 T. The black dash frames denote the profile of e^-/p^+-beam cross-section.

Table 7.3 summarizes the maximal B_1 deviation in e^-/p^+-beam, and the resulted A_{exp} deviations for 3 T to 6 T cases.

As shown in table 7.3, the maximal B_1 deviation in the e^-/p^+-beam cross-section is below 1.6×10^{-4}, which results the maximal A_{exp} deviation below 3.3×10^{-5}.

B_0 homogeneity.

B_1	Max. $\frac{\Delta B_1}{B_1}$	Deviation Ratio $\frac{\Delta A_{exp}}{A_{exp}} / \frac{\Delta B_1}{B_1}$	Max. $\frac{\Delta A_{exp}}{A_{exp}}$
3 T	1.6×10^{-4}	0.207	3.3×10^{-5}
4 T	1.6×10^{-4}	0.133	2.1×10^{-5}
5 T	8.1×10^{-5}	0.098	7.9×10^{-6}
6 T	8.0×10^{-5}	0.077	6.2×10^{-6}

Table 7.3: The relative deviations of the selector field B_1 in the e^-/p^+-beam cross-sections, and the resulted A_{exp} deviations. The term *Deviation Ratio* is calculated with eqn. 7.2.

As shown in figure 6.4 and table 7.1, the B_0 field in the middle of the decay volume has a uniform distribution, but is maximally decreased by 44% at the beginning of the n-guide, and increased by 55% in the decoupling area. The electrons generated in different regions result in different measured A_{exp}. Figure 7.10 shows the deviation of A_{exp} values, which are induced by the neutrons along the z-direction of the decay volume.

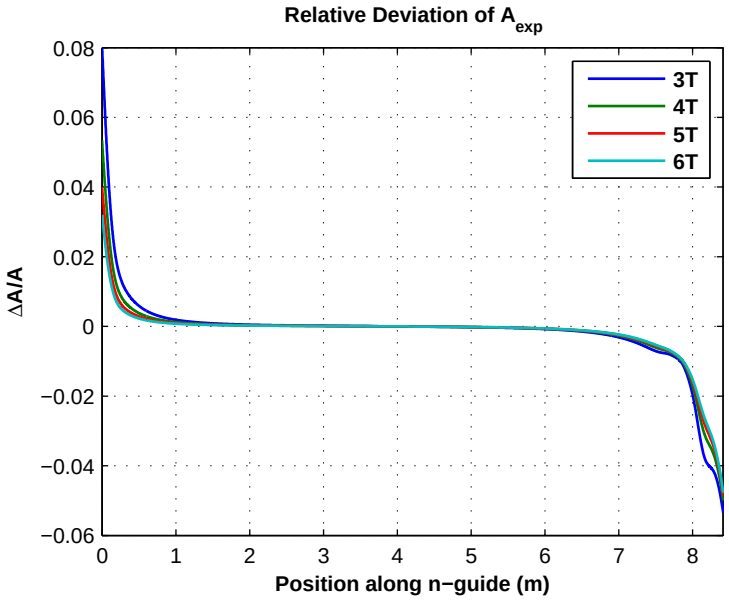

Figure 7.10: The relative deviations of A_{exp} that are induced by neutrons at different positions in the decay volume, with the selector field B_1 from 3 T to 6 T. The deviations are relative to the theoretical value A^0_{exp}, which assumes B_0 = 1.5 T.

In the continuous n-beam mode, the total deviation of A_{exp} measured by detector is that integrated over the decay volume space

$$D_A = \frac{1}{A^0_{exp}} \frac{\int [A_{exp}(\mathbf{r}) - A^0_{exp}] N(\mathbf{r}) \mathrm{d}\mathbf{r}^3}{\int N(\mathbf{r}) \mathrm{d}\mathbf{r}^3} \tag{7.4}$$

A^0_{exp} is the expected asymmetry when B_0 = 1.5 T, and $A_{exp}(\mathbf{r})$ is the measured asymmetry with the neutrons at position $\mathbf{r}$, where has a field of $B_0(\mathbf{r})$. The event rate $N(\mathbf{r})$ is dependent

on the neutron density $\rho(\mathbf{r})$ and the solid angle defined by critical angle $\theta_c(\mathbf{r})$

$$N(\mathbf{r}) \propto \rho(\mathbf{r}) \cdot \frac{1}{2}(1 - \cos\theta_c(\mathbf{r})) \tag{7.5}$$

The neutron density $\rho(\mathbf{r})$ can be considered as constant in the n-guide. From the n-guide end to the separation point, it is assumed that the overlap of the e^-/p^+- and n-beams is decreased linearly. Table 7.4 lists the integrated deviations D_A over different ranges of the decay volume.

B_1	Total D_A	Beginning (0~1 m)	Middle (1~7 m)	End (7~8.4 m)
3 T	-7.76×10^{-4}	1.13×10^{-2}	-1.37×10^{-4}	-1.24×10^{-2}
4 T	-1.01×10^{-3}	7.44×10^{-3}	-1.56×10^{-4}	-1.09×10^{-2}
5 T	-1.15×10^{-3}	5.56×10^{-3}	-1.66×10^{-4}	-1.02×10^{-2}
6 T	-1.25×10^{-3}	4.46×10^{-3}	-1.72×10^{-4}	-9.92×10^{-3}

Table 7.4: Integrated deviations D_A over the ranges of the decay volume, with the selector field B_1 from 3 T to 6 T.

The total D_A stands for the correction on A_{exp} caused by B_0 homogeneity in continuous n-beam mode, and is on the level of 10^{-3} as shown in table 7.4.

However, the $\Delta A_{exp}/A_{exp}$ from the beginning and the end part of decay volume make opposite contributions, thus result a cancellation of D_A. To acquire a better understanding to the systematical errors of B_0 corrections, we define the *standard deviation* σ_A of A_{exp} relative to the theoretical value A^0_{exp} (not relative to the average value) as

$$\sigma_A = \frac{1}{A^0_{exp}} \sqrt{\frac{\int [A_{exp}(\mathbf{r}) - A^0_{exp}]^2 N(\mathbf{r}) \mathrm{d}\mathbf{r}^3}{\int N(\mathbf{r}) \mathrm{d}\mathbf{r}^3}} \tag{7.6}$$

which can reflect the possible scale of the systematic errors on the B_0 homogeneity corrections. The σ_A over different ranges in the decay volume are summarized in table 7.5.

B_1	Total σ_A	Beginning (0~1 m)	Middle (1~7 m)	End (7~8.4 m)
3 T	9.11×10^{-3}	1.87×10^{-2}	8.70×10^{-4}	1.67×10^{-2}
4 T	7.11×10^{-3}	1.23×10^{-2}	7.10×10^{-4}	1.45×10^{-2}
5 T	6.27×10^{-3}	9.20×10^{-3}	6.40×10^{-4}	1.35×10^{-2}
6 T	5.86×10^{-3}	7.36×10^{-3}	6.01×10^{-4}	1.31×10^{-2}

Table 7.5: Integrated standard deviations σ_A over the ranges of the decay volume, with the selector field B_1 from 3 T to 6 T.

As shown in table 7.4, in the 6 m middle range of the decay volume, the correction of A_{exp} is on the order of 10^{-4}. This range can be chosen as the *effective decay volume* for the pulse n-beam mode measurements.

For continuous n-beam, the correction is on the level of 10^{-3}. If the experiment requires the A_{exp} errors on 10^{-4} level, the measurement of B_0 should obtain an accuracy on 10^{-3} according to the *Deviation Ratio* column in table 7.3.

7.3.4 Adiabatic criterion of e^-/p^+ transports

The non-adiabatic transports of charged particles may cause the changes of their pitch angles as introduced in Section B.2. The changes of pitch angles further lead to distortion of the measured spectra when the magnetic mirror B_0/B_1 is applied.

In the precise measurement of PERC, the adiabatic criterion of e^-/p^+ transports, namely the field change in one helical pitch is required to be $\gamma \ll 1$ [Dub08]. Figure 7.11 plots the maximal values of the criterion γ along the e^-/p^+-beam.

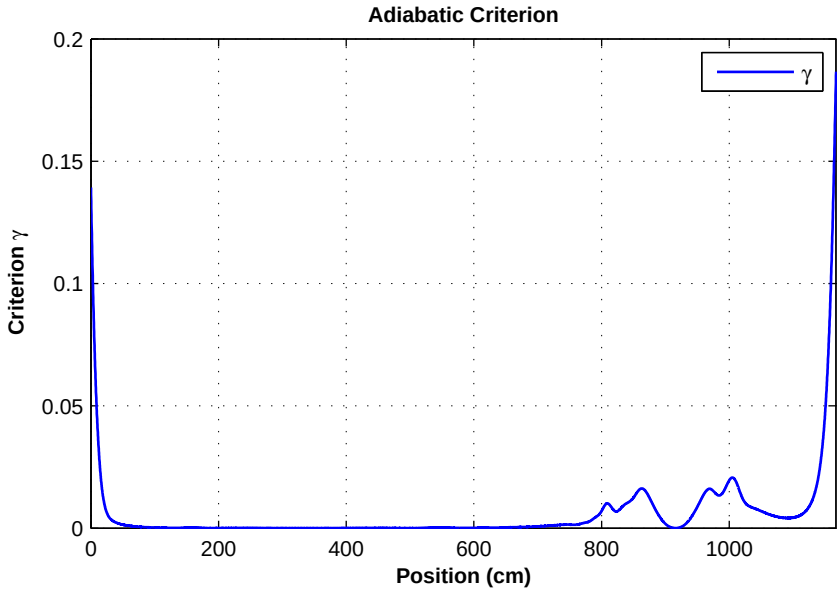

Figure 7.11: The maximal values of adiabatic criterion γ relative to the positions along the e^-/p^+-beam. Assuming the e^-/p^+ pitch angle is $\theta = 0^o$, e^-/p^+ momenta $p = 1.19$ MeV/c and selector field $B_1 = 6$ T.

As shown in figure 7.11, the value of γ is below 2.1×10^{-2} from the middle of decay volume to the middle of detector vessel. At the beginning of the decay volume, γ has the value of 0.14, which is caused by the field increase in this range. The non-adiabatic effect from this range is unavoidable in experiments, and should be studied in the data analysis. At the detector, γ increases to 0.18 due to the low magnetic field and the fast field decrease at the end of PERC.

The non-adiabatic effects after the selector coil do not influence normal energy or asymmetry measurements, but possibly influence other measurements of post spectrometers, e.g. proton retardation detector with electrodes. If we apply spectrometers sensitive to the

e^-/p^+ pitch angles, e.g. aSPECT or magnetic spectrometer, the adiabatic criterion should be fulfilled by other contributions from the post spectrometers.

7.3.5 R×B drift effects

In PERC instrument, the **R**×**B** drift effect are sufficiently suppressed by the high magnetic field and the dromedary magnetic field geometry.

The maximal drift for e^-/p^+ with momentum p = 1.19 MeV/c, emission angle $\theta_0 = 45^o$, and selector field B_1 = 3 T, is 0.06 mm from the decay volume to the selector, and 0.16 mm to the detector. The negligible drift ensures our calculations of e^-/p^+-beam by magnetic lines.

Chapter 8

Experimental Properties of PERC

8.1 Experimental Properties Related to PERC Magnet System

8.1.1 Inductances of magnets

The superconducting magnets in PERC have large inductances, and store much energy when they generate high magnetic fields

$$W_m = \frac{1}{2}\sum_n I_m L_{mn} I_n \tag{8.1}$$

where L_{mn} are the self- and mutual inductances between the coils, and $I_{m,n}$ are the currents of them. Table 8.1 lists the simulated the self- and mutual inductances of the magnets in PERC and the stored energies.

Coils	Self-inductance (H)	Mutual-inductance (H)	Stored Energy (J)
Decay Coil	1.99×10^{0}	8.94×10^{-2}	9.31×10^{5}
Bend Coil 1	2.21×10^{-1}	2.02×10^{-1}	7.46×10^{4}
Bend Coil 2	5.74×10^{-1}	6.08×10^{-1}	2.03×10^{5}
Selector Coil	4.72×10^{0}	6.47×10^{0}	1.93×10^{6}
Sele.Corr. 1	1.19×10^{-1}	7.35×10^{-1}	1.47×10^{5}
Sele.Corr. 2	1.19×10^{-1}	7.39×10^{-1}	1.47×10^{5}
Filter Coil 1	4.23×10^{0}	4.16×10^{0}	1.54×10^{6}
Filter Coil 2	4.23×10^{0}	4.16×10^{0}	1.54×10^{6}
Bend Coil 3	7.91×10^{-1}	6.51×10^{-1}	2.45×10^{5}
Detector Coil	4.97×10^{-1}	1.52×10^{-1}	1.10×10^{5}

Table 8.1: Self- and mutual inductances of the PERC magnets, and the stored energies in them when B_1 is 6 T. The *Mutual-inductance* denote the sum of the mutual inductances with all other coils. The small correction coils on the decay coil are not considered here.

The whole magnet system stores 6.87×10^{6} J energy in the standard operation mode.

8.1.2 Superconducting wire and quenching effect

For the PERC instrument that produces strong magnetic fields, much attention has to be paid on the behaviours of the superconducting wires in the design of the magnet system.

Experimentally, the superconductor (SC) can suddenly lose the superconductivity and convert into normal conductor due to the vibrations of the environments, so called as the superconductor *quenching*.

The criterion of the quenching is related to the temperature T, the experienced magnetic field B and the current density J. For the type II superconductor Niobium Titanium alloy (NbTi), an empirical formula to describe the relations of the critical B_c and T_c is [Lub83]

$$B_c(T) = B_c(0)\left[1 - \left(\frac{T}{T_c}\right)^{1.7}\right] \tag{8.2}$$

And the critical current density J_c is [Bot00]

$$J_c(B,T) = J_c(5T, 4.2K) \cdot \frac{28.4}{B} \cdot \left[\frac{B}{B_c(T)}\right]^{0.8} \cdot \left[1 - \frac{B}{B_c(T)}\right]^{0.89} \left[1 - (\frac{T}{T_c})^{1.7}\right]^{1.87} \tag{8.3}$$

The fitting parameters in the equation are evaluated by [Bot00]. $T_c(0)$ and $B_c(0)$ are the critical temperature and magnetic field, and are 9.35 K and 14.25 T respectively. From the data sheet from EAS Bruker [EAS], we set the $J_c(5T, 4.2K)$ as 2754 A/mm^2, which is the superconducting wire used in ATLAS magnets in LHC of CERN.

Figure 8.1 plots the critical surface of NbTi.

Once a segment of the superconductor quenches into normal conductor, the stored energy in the magnet will produce much heat on the quenched point, thus probably cause damages on the magnet or other contacted material, e.g. the electrical insulations or cooling system. Additionally, the heat can rapidly boil the cooling cryogen e.g. liquid He (if LHe bath is used for cooling), then produce high pressure in short time and cause explosion in the worst case.

To avoid the quenching as far as possible, the superconducting wires and the current densities should be well defined. A conventional superconducting wire for magnets has a set of twisted NbTi filaments embedded inside a Cu matrix, which has better electrical and thermal conductivity than normal NbTi. When the inner SC quenches, the Cu matrix can share the current flow in the wire, and produce less heat, further transmit the heat away faster than NbTi.

In the PERC design, we assume the superconducting wire has the cross-section of 3.1×2.2 mm^2, and 3.2×2.4 mm^2 including the insulation, with the ratio of Cu and SC as 10. Figure 8.2 shows the cross-section view of the superconducting wire, and the critical current versus magnetic field according to eqn. 8.2.

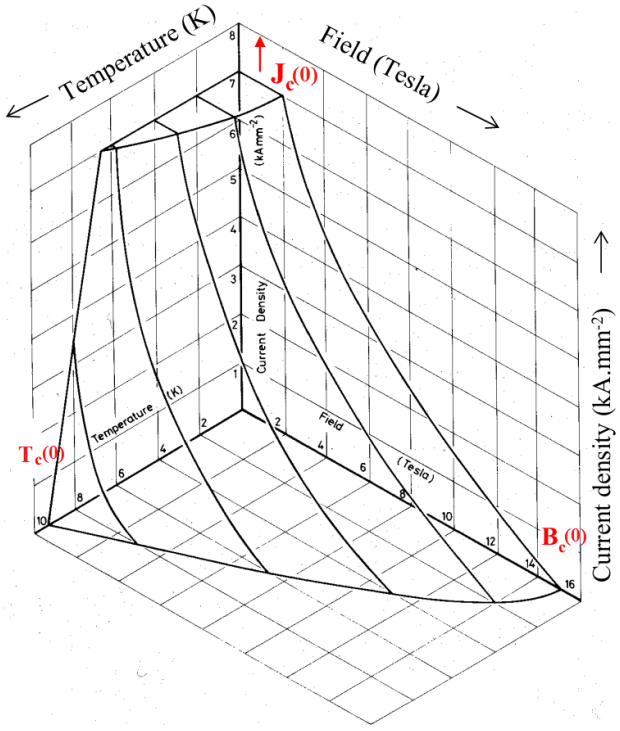

Figure 8.1: The critical surface of NbTi between superconductive and normal resistive states as a function of temperature T, magnetic field B and current density J. The range beneath the surface denotes the superconducting state. $T_c(0)$ and $B_c(0)$ are the critical temperature and magnetic field respectively. The critical current density $J_c(0)$ out of the plot, is dependent on wire processing. Figure is from [Wil87].

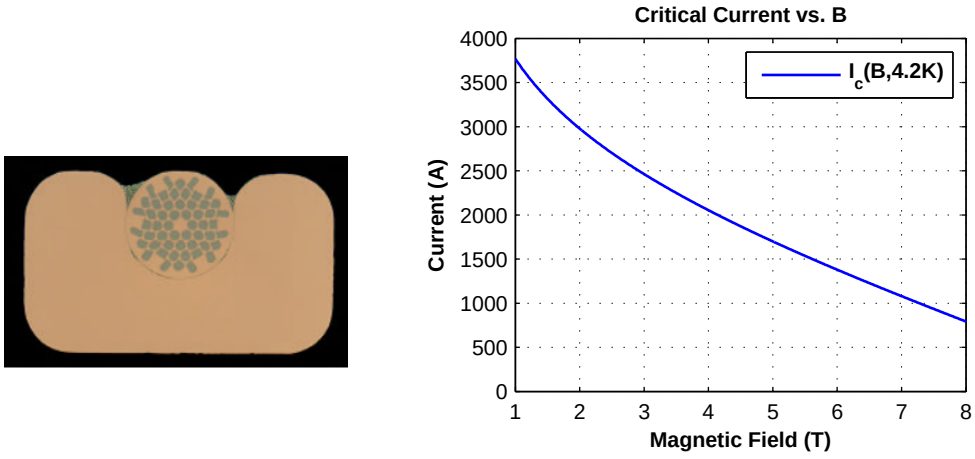

(a) **(b)**

Figure 8.2: The superconducting wire assumed in PERC design. **(a)** Plot of the wire cross-section. Figure is from [EAS]. **(b)** The critical current I_c of the wire versus the B field at the temperature of T = 4.2 K. The J_c(5T,4.2K) on SC is assumed as 2754 A/mm^2, the ratio of Cu and SC in the wire cross-section is assumed as 10.

The critical currents of PERC magnets can be calculated with the information of the B_{max} in table D.1. The nominal currents for the magnets in PERC are chosen to be at least 40% less than the critical current.

To reduce the damages on magnets, every power supply has a security system to damp the current when the magnets lose superconductivity. The security system can detect the quenching electronically after a time interval t_D, then cuts off the power of magnet, at the same time connects a discharge resistance R in the circuit. Figure 8.3 **(a)** sketches the mechanism of the security system.

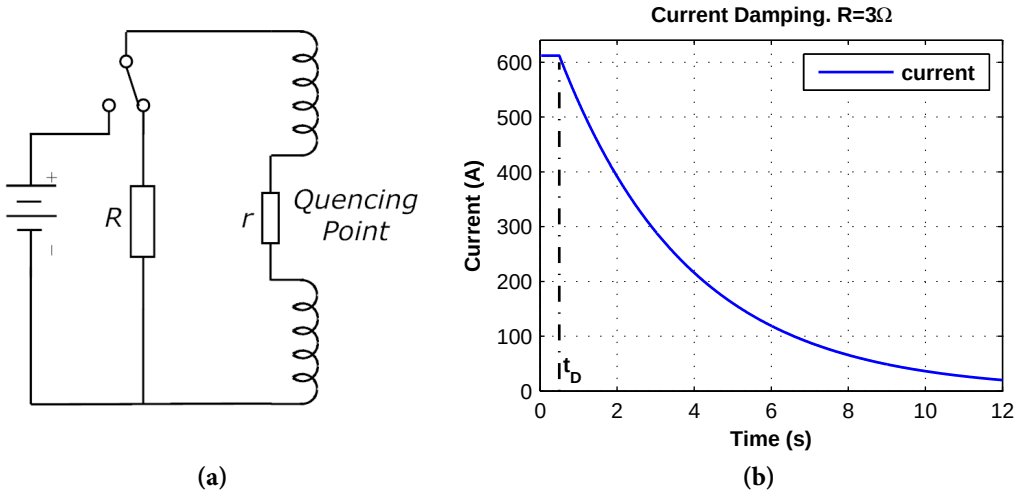

(a) **(b)**

Figure 8.3: (a) Sketch of a security system for the current damping. **(b)** An example of the current damping of the filter coils as a function of time. The current-constant power supply is cut off after a time interval t_D = 0.5 s, the total resistance R+r is assumed as 3Ω, inductance L_{lk} is from table 8.1. The current decreases to 10% at 8.2 s.

Assuming the quenched segment has a constant resistance of r, the voltage in the magnet is

$$\varepsilon_m = I \cdot (R + r) = -\sum_n L_{mn} \frac{\mathrm{d}I_n}{\mathrm{d}t} \tag{8.4}$$

If the magnets number l to k share one power supply, and other magnets do not quench, the voltage will be

$$\varepsilon = \sum_{m=l}^{k} \varepsilon_m = -L_{lk} \frac{\mathrm{d}I}{\mathrm{d}t}, \quad \text{with} L_{lk} = \sum_{m=l}^{k} \sum_{n=l}^{k} L_{mn} \tag{8.5}$$

The current in the magnet will decrease with time

$$I = I_0 e^{-\frac{R+r}{L_{lk}} t} \tag{8.6}$$

Figure 8.3 **(b)** plots the current damping of the two filter coils. The total resistance R+r is assumed as a constant [1].

Including the detection time t_D, the total heat generated by the sector of quenched wire is

$$Q = \frac{1}{2} W \frac{r}{R+r} + I_0^2 \, r \, t_D \tag{8.7}$$

with W the stored energy in table 8.1. The effects caused by the heat according to eqn. 8.7, need to be well studied in the manufacture of the magnets and cooling system.

8.1.3 Magnetic shielding

The strong magnetic field from PERC is dangerous for people with cardiac pacemaker, and possibly influences other experiments nearby. The magnetic field outside PERC is required to be shielded by non-linear material, and attenuated to 5 Gauss in a reasonable distance. Figure 8.4 **(a)** sketches a design of the magnetic shielding of PERC.

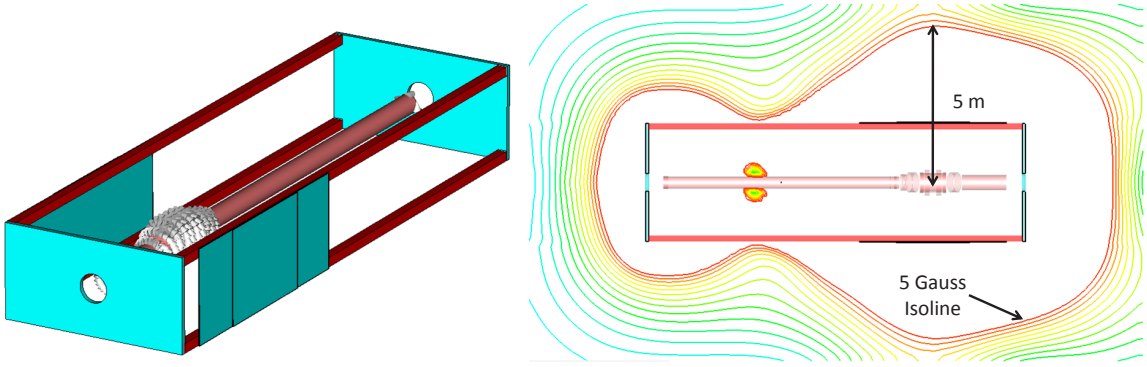

Figure 8.4: (a) Sketch of the magnetic shielding of PERC. **(b)** Magnetic field distribution out of PERC. The maximal distance from the 5 Gauss isoline to the PERC central axis is 5 m.

The magnetic shielding consists of several steal plates for the field screening, and four iron pillows to guide the magnetic lines in a loop. The magnetic field outside PERC can be decreased to 5 Gauss at 5 m distant from the PERC central axis, as shown in figure 8.4 **(b)**.

However, the non-linear material also influences the delicate magnetic field inside PERC. Figure 8.5 plots the relative changes of the magnetic field along the e^-/p^+-beam, caused by the magnetic shielding.

[1] In reality, the heat generated in the quenched segment is transmitted along the wire, and cause the temperature rise further the quenching of other segments. The propagation speed of quenching effect is about 5-20 m/s. Furthermore, the resistivity of Cu also changes with the temperature. Therefore, the resistance r is not a constant, and the current damping in the real magnet is more complex.

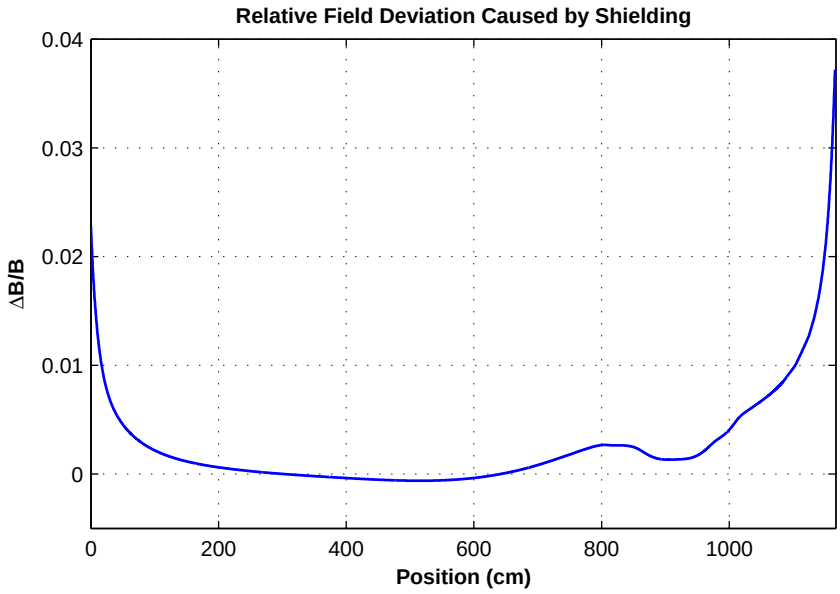

Figure 8.5: The relative changes of the magnetic field $\Delta B/B$ along the e^-/p^+-beam, caused by the non-linear magnetic shielding.

The figure 8.5 shows a maximally 3.7% change of the field by the shielding material. From the simulation, the homogeneity of B_1 in e^-/p^+-beam cross-section is changed by about 0.5%.

It is necessary to note, the properties of the shielding highly depend on the material purity and manufacture processes, which are more complex than that in the simulation. The real influences of the material on the field inside PERC can be more serious than expected. One has to optimize the shielding configuration with highest efficiency, as well as minimize the influences from the non-linear material.

8.1.4 Forces and torques

The information of the magnetic forces and torques on the coils and magnetic shielding are necessary for the design of mechanic supports. Table 8.2 lists the forces and the torques on the coils and on different parts of the shielding.

8.2 R×B Drift Momentum Spectrometer

In this section, we propose the method of a new kind of e^-/p^+momentum spectrometer, which uses the **R**×**B** drift effect to disperse the e^-/p^+particles due to their momenta.

Coils	F_x (N)	F_y (N)	F_z (N)	Torque (N·m)
Decay Coil	0.00×10^{0}	2.29×10^{3}	1.59×10^{5}	1.66×10^{3}
Bend Coil 1	0.00×10^{0}	6.26×10^{4}	1.40×10^{5}	-1.47×10^{4}
Bend Coil 2	0.00×10^{0}	-3.94×10^{4}	5.15×10^{5}	2.64×10^{4}
Selector Coil	0.00×10^{0}	4.47×10^{4}	2.74×10^{4}	-5.19×10^{4}
Sele.Corr. 1	0.00×10^{0}	-2.09×10^{4}	1.14×10^{6}	1.15×10^{5}
Sele.Corr. 2	0.00×10^{0}	-2.21×10^{4}	-1.13×10^{6}	-6.58×10^{4}
Filter Coil 1	0.00×10^{0}	-1.57×10^{4}	1.35×10^{6}	1.31×10^{5}
Filter Coil 2	0.00×10^{0}	-1.43×10^{4}	-1.34×10^{6}	-9.88×10^{4}
Bend Coil 3	0.00×10^{0}	2.68×10^{3}	-6.86×10^{5}	-1.74×10^{4}
Detector Coil	0.00×10^{0}	2.26×10^{4}	-1.60×10^{5}	-5.24×10^{4}
Shielding				
Back Plate	0.00×10^{0}	0.75×10^{0}	2.29×10^{3}	6.72×10^{0}
Front Plate	0.00×10^{0}	1.23×10^{1}	-1.02×10^{4}	-1.15×10^{2}
Left Part	-2.14×10^{3}	8.06×10^{1}	2.78×10^{3}	7.01×10^{3}

Table 8.2: The forces and torques on the coils and the shielding. The definitions of x, y, z directions are same as in figure 6.1. The torque axis is located at the end of the n-guide, and points to positive x-axis. The forces of the right part of shielding is symmetric to the left part. The correction coils on the decay coil are not considered here.

8.2.1 Momentum analysis and magnetic spectrometer

A magnetic spectrometer for the momentum measurements of e^-/p^+particles is desired in the experiments with PERC. Besides the energy spectra, the momentum spectra can supply another resolution to investigate the charged decay products, as well as realize the measurements of both electrons and protons at the same time. The principle of a magnetic spectrometer is sketched in figure 8.6.

As shown in figure 8.6, the magnetic spectrometer must firstly shield the field of detector coil B_2 at the end of PERC, and apply a vertical weak magnetic field B_3. The incident $e^-/p^+$from PERC pass through a small aperture, then disperse in B_3 field due to their charges, momenta and incident angles. The position sensitive detectors for electrons and protons are placed on both sides of the incident window. The *dispersion distances* of the particles are

$$D = 2\frac{p}{qB}\cdot f(\theta) = 2\frac{p}{qB}\cos\theta \tag{8.8}$$

where p and q are the momentum and charge of a particle. θ is the incident angle, as shown in figure 8.6 **(b)** [2].

Compare with energy resolving detectors, the magnetic spectrometer has the advantages:

[2]Eqn. 8.8 is valid for incident e^-/p^+in any direction.

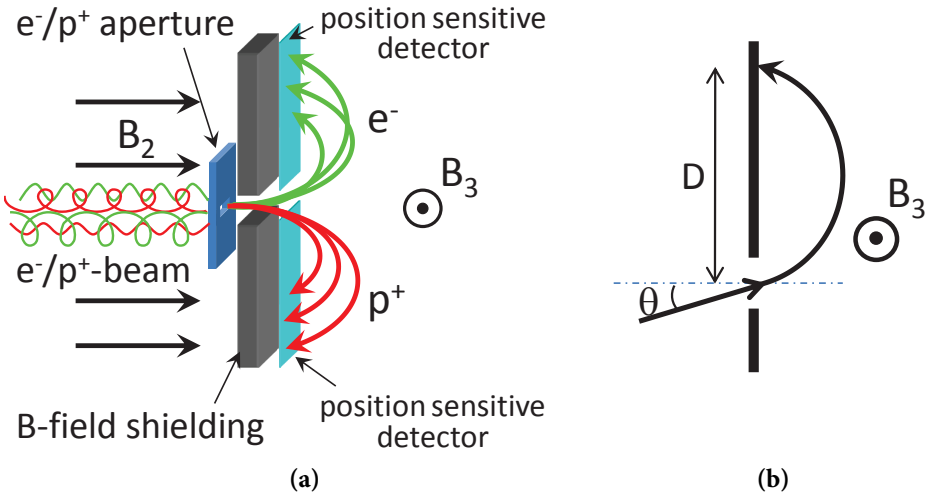

Figure 8.6: The principle of a magnetic spectrometer after PERC.

- *Versatile measurements.*

  As shown in figure 6.6, the magnetic spectrometer can be used in nearly all measurements of PERC.

- *e^-/p^+ detection at the same time.*

  In the magnetic spectrometer, electrons and protons are dispersed in different directions. The momenta of them can be measured at the same time, with coincidence or without. For instance, the TOF of protons can be measured by using electrons as trigger signals.

- *Momentum analyses.*

  The magnetic spectrometer realizes the momentum analyses, which supply another scale of the e^-/p^+spectra. Compare with the energy spectrum, the momentum spectrum has more resolutions in low energies range, as shown in figure 8.7. As stated in Section 2.3.3 , the measurements of low energy e^- are especially needed for the determination of the Fierz interference term b_F.

- *Backscattering suppression.*

  An ideal magnetic spectrometer can use digital pixel detector to measure the positions of the particles. The pixel detector only requires a deposition energy of particles over a low threshold, hence the backscattering effect does not influence the measurement greatly.

- *Background and environment insensitivity.*

  The digital pixel detector is much less sensitive to the environment e.g. temperature and γ-ray than energy spectra detectors. The background can be strongly suppressed, and the calibration of detector is not required frequently.

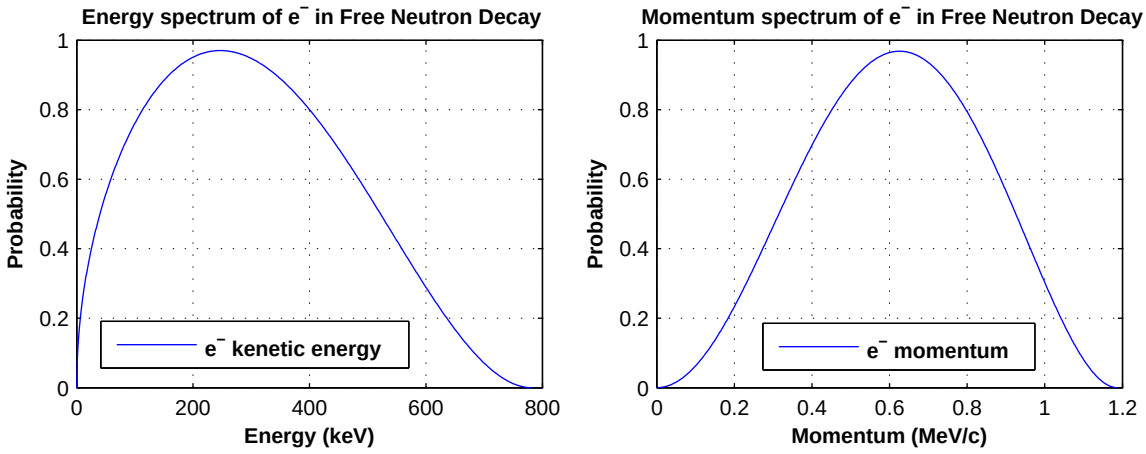

(a) e^- energy spectrum. **(b)** e^- momentum spectrum

Figure 8.7: Energy and momentum spectra of e^- from free neutron decay, according to eqn. 2.11. The momentum spectrum has more resolutions in the low energy range.

However, we found difficulties in eliminating the guiding field of PERC during the design of the magnetic spectrometer. As shown in figure 8.6 **(c)**, the magnetic spectrometer must drastically decrease the guiding field B_2 from 0.2 T to about 10 mT in very short distance at the incident window, typically in several mm [Dub08]. In addition, the field of PERC must be totally shielded in the spectrometer.

From the simulation, we cannot find a proper non-linear material to decrease the guiding field in very short distance, neither to shield the strong PERC field completely. The charged e^-/p^+ from PERC will follow the combination of residual B_2 and B_3 fields, and hardly be dispersed, as plotted in figure 8.8 **(a)**.

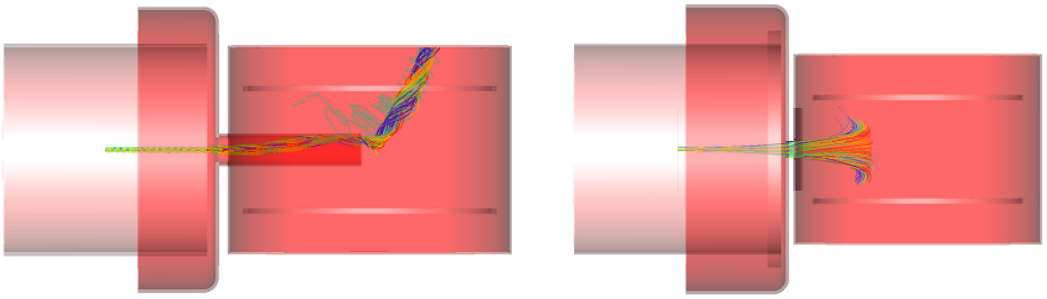

(a) **(b)**

Figure 8.8: Attempts to the magnetic spectrometer design. A pair of shielded Helmholtz coils are placed after PERC to generate a vertical analysing field B_3. **(a)** Only with the non-linear material (red part) around the spectrometer, it is not enough to completely shield the B_2 field. **(b)** Additionally with a set of correction coils on the detector coil, the B_2 field can be rapidly decreased. Whereas the pitch angles of e^-/p^+ are strongly distorted. The e^-/p^+ are emitted from the left side with emission angle of 0^o. After they pass through the aperture, their pitch angles are increased to about $\pm 15^o$ in B_3.

If we additionally apply a set of correction coils, B_2 can be fast decreased, but the pitch angles of $e^-/p^+$are strongly distorted, as plotted in figure 8.8 **(b)**.

From the theoretical point of view, since the magnetic lines do not vanish, they can only spread in vertical directions if the field decreases, as sketched in figure 8.9.

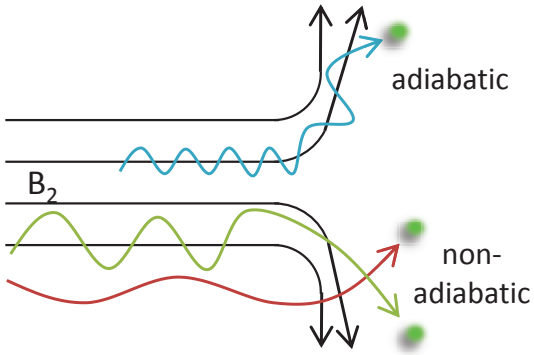

Figure 8.9: Sketch of e^-/p^+motion in the drastically decreased B_2 field. The magnetic field lines spread in vertical directions when the field strength decreases. For the adiabatic transports of e^-/p^+, the particles follow the magnetic lines to vertical directions. In non-adiabatic transports, the $e^-/p^+$are bended in the vertical field. In both cases the pitch angles of the particles are highly distorted.

When the e^-/p^+pass the spreaded fields adiabatically, they will follow the magnetic lines. If they move non-adiabatically, they will be bended by the vertical field due to Lorentz force. In both cases, the pitch angles of the e^-/p^+particles are highly distorted in this area.

The distortions the e^-/p^+pitch angles strongly depend on the field distribution and the e^-/p^+momenta, hence are not predictable nor controllable. Therefore, the distribution of particles on the detector can hardly represent their momenta.

8.2.2 Principle of R×B drift spectrometer

Because of the failure on the attempts to the design of the dispersive magnetic spectrometer, here we propose a method of **R**×**B** drift momentum spectrometer, which can realize the momentum analyses of decay e^-/p^+without eliminating the guiding field of PERC.

As discussed in Section B.4, when a charged particle propagates in a curved magnetic field, it has the drift effect perpendicular to the magnetic field **B** and the field curvature **R**. In the static magnetic field, the velocity components of a particle parallel and vertical to the magnetic field line $v_\parallel$ and $v_\perp$, can be expressed with the particle velocity v and pitch angle θ

$$v_\parallel = v \cdot \cos\theta \ , v_\perp = v \cdot \sin\theta \tag{8.9}$$

From eqn. B.11, the drift velocity $\mathbf{v}_d$ of first order can be expressed as

$$\mathbf{v}_d = \frac{mv^2}{qBR}(\cos^2\theta + \frac{1}{2}\sin^2\theta) \cdot \frac{\mathbf{R}\times\mathbf{B}}{RB} \tag{8.10}$$

where m is the mass of the particle. Suppose that we apply a uniformly curved magnetic field, with the curvature R and the magnetic field B as constants. In this case, the curved magnetic lines are distributed parallel and coaxial, as shown in figure 8.10.

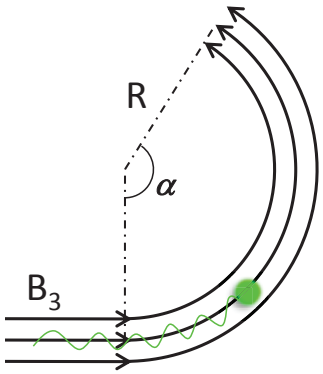

Figure 8.10: Sketch of the principle of the **R**×**B** drift spectrometer, in which a uniformly curved magnetic field B_3 is generated. The magnetic field lines are distributed parallelly and coaxially, and are bended by an angle of α.

In the uniformly curved magnet field, the drift velocity v_d is a constant according to eqn. 8.10, and the second order contribution related to $\dot{\mathbf{v}}_d$ as shown in eqn. B.13 is zero. During a propagating time of T, the drift distance D of a particle is the integration of v_d

$$D(p,\theta) = \int_T v_d \mathrm{d}t = \frac{p}{qB} \cdot \alpha \cdot f(\theta) \tag{8.11}$$

where α is the bending angle of the route of particle gyration center during the time T

$$\alpha = \frac{v_\parallel T}{R} \tag{8.12}$$

as marked in figure 8.10. $f(\theta)$ is a factor related to the particle pitch angle

$$f(\theta) = \frac{1}{2}\left(\cos\theta + \frac{1}{\cos\theta}\right) \tag{8.13}$$

Compare eqn. 8.11 with eqn. 8.8, the behaviours of **R**×**B** drift are similar as the particle dispersion in the magnetic spectrometer. The drift and dispersion distances in both cases are proportional to the particle momentum, and inversely proportional to the analysing magnetic field and particle charge.

With this principle, we built up the magnet system of the **R**×**B** drift momentum spectrometer in simulation, as shown in figure 8.11 **(a)**.

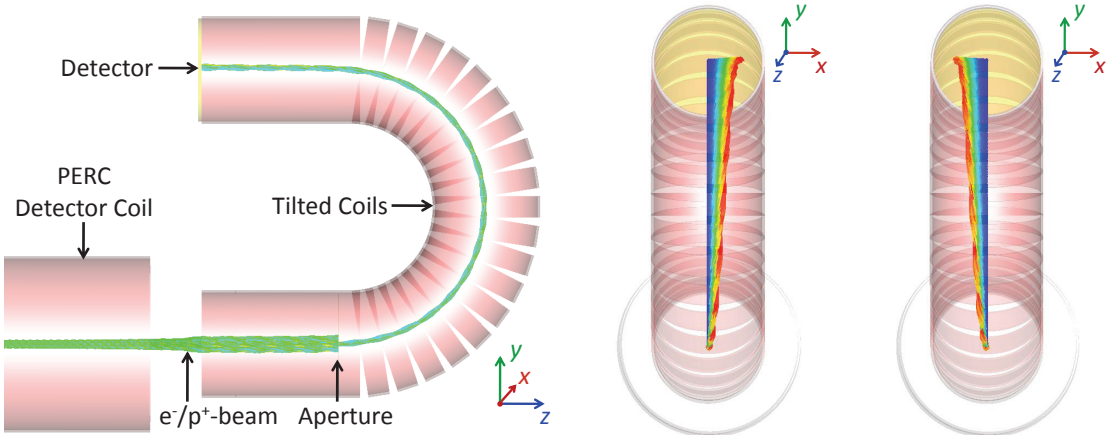

(a) Left Side View **(b)** Electron. **(c)** Proton.

Figure 8.11: (a) The design of the **R**×**B** spectrometer at the end of PERC, and the simulated trajectories of e^-/p^+. **(b)** The front view of the simulated electron and **(c)** the proton trajectories in spectrometer. The colors of the trajectories denote the particle momenta, that are arranged continuously from 0 to 1.19 MeV/c.

At the beginning of the **R**×**B** spectrometer, we apply several connected coils to gradually decrease the guiding field of PERC from 0.5 T to 0.15 T, with the field gradient satisfies the e^-/p^+adiabatic transports. After these coils, a series of tilted coils generate a 180° bended magnetic field. Along the central line of the tilted coils, the curvature of the magnetic field line is $R = 40$ cm, and the field strength is kept as a constant $B_3 = 0.15$ T. Figure 8.12 plots the magnetic field from the end of PERC to the **R**×**B** spectrometer detector.

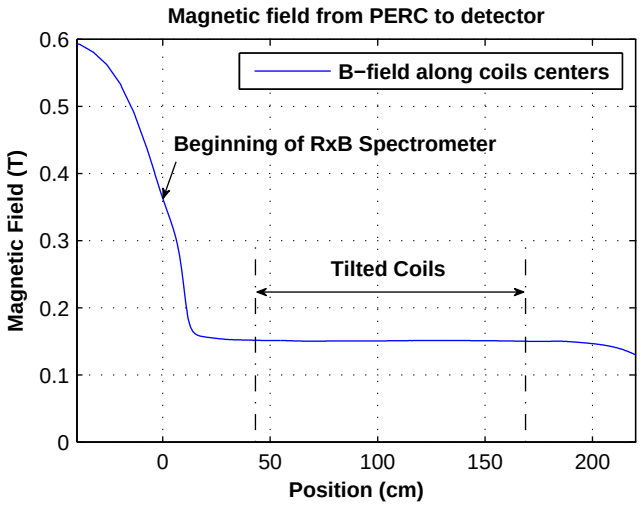

Figure 8.12: The magnetic field strength along the central line of the coils from the end of PERC to the detector of **R**×**B** spectrometer. The field is decreased gradually from $B_2 = 0.5$ T at the end of PERC to $B_3 = 0.15$ T, and is kept as constant in the tilted coils. The zero position denotes the beginning of the **R**×**B** spectrometer.

At the beginning of the tilted coils, we apply an aperture of 1×1 cm^2 to define the size of the

incident e^-/p^+-beam. The particles through the aperture follow the curved magnetic lines, and turn 180° then reach the detector on top. During the propagation, they drift along the positive and negative x-axis according to their charges and momenta. The dispersion of electrons and protons can be clearly observed in the simulation, as shown in figure 8.11 **(b)** and **(c)**.

Hence the **R**×**B** drift spectrometer, instead of eliminating the guiding field of PERC, evolves the field smoothly and gradually to the analysing magnetic field. The charged particles can be transported adiabatically during the processes, and the angular information of them can be kept and measured.

Table 8.3 lists the parameters of the standard configuration of the **R**×**B** spectrometer design.

Parameter	Comment	Value	Parameter	Comment	Value
B_3	Analysing field	0.15 T	B_1	Selector field	6 T
R_0	Field line curvature	40 cm	θ_{max}	Max. pitch angle	9.1°
w	Aperture width	1 cm	r_{max}	Max. gyration radius	0.42 cm
h	Aperture height	1 cm	D_{max}	Max. drift	8.29 cm
α	Bending angle	π			

Table 8.3: Parameters of the standard configuration of the **R**×**B** drift spectrometer.

w and h in table 8.3 are the width and height of the aperture along the x- and y-axes. θ_{max} and r_{max} are the maximum pitch angle and gyration radius of the decay e^-/p^+ in the B_3 field. For the e^-/p^+ from B_1 = 6 T to B_3 = 0.15 T, their pitch angles and gyration radii are limited in

$$0 \leqslant \theta_3 \leqslant \theta_{max} = \arcsin\sqrt{\frac{B_3}{B_1}}, \quad 0 \leqslant r \leqslant r_{max} = \left|\frac{p_{max}}{qB_3}\right| \sin\theta_{max} \tag{8.14}$$

where p_{max} = 1.19 MeV/c is the maximum momentum of e^-/p^+ from the free neutron decay [PDG12].

With the standard configuration, the maximum drift D_{max} for p_{max} is 8.29 cm.

8.2.3 Corrections on R×B drift spectrometer and e^-/p^+ distribution

In the **R**×**B** spectrometer, the particle distribution on the detector is influenced by the properties of the particles and the instrument.

e^-/p^+ *pitch angle* θ

Compare eqn. 8.11 with eqn. 8.8, both the drift and the dispersion have corrections related to the pitch (incident) angle θ. However, because of the presence of the $v_\perp$ component in **R**×**B** drift in eqn. B.11, the influence of the correction factor $f(\theta)$ in the **R**×**B** spectrometer is much smaller than that in the dispersive magnetic spectrometer. In figure 8.13, the magnitudes of both correction factors are plotted.

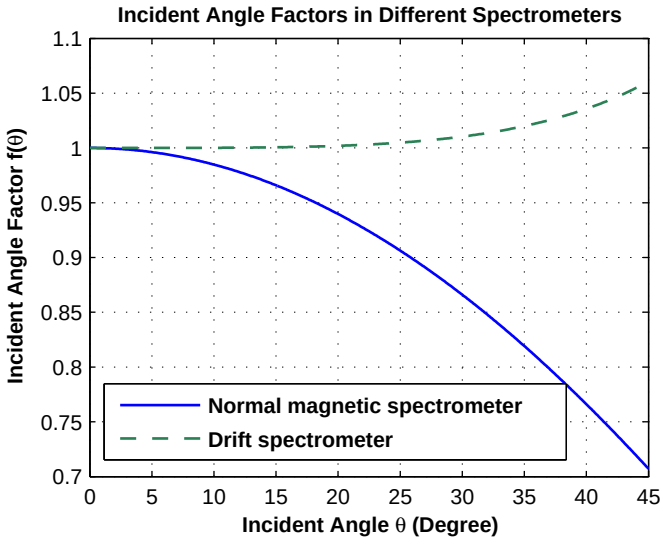

Figure 8.13: The incident angle factors $f(\theta)$ in the dispersive magnetic spectrometer and the $\mathbf{R}\times\mathbf{B}$ drift spectrometer, versus the incident (pitch) angle θ from 0° to 45°.

For $\theta < 9.6°$, i.e., the solid angle less than 88 msr, the $f(\theta)$ in the $\mathbf{R}\times\mathbf{B}$ drift is negligible as less than 10^{-4} deviated from 1, while the deviation in the magnetic spectrometer is 1.4×10^{-2}. Hence the $\mathbf{R}\times\mathbf{B}$ spectrometer has large acceptance of e^-/p^+incident angles, which is a significant advantage.

***Gyration radius** r **and aperture width** w*

In the $\mathbf{R}\times\mathbf{B}$ spectrometer, the gyration radii of particles remain during the drifts and the detection. For a given momentum, the maximum gyration radius of the particle is

$$r_c(p) = \left|\frac{p}{qB_3}\right| \cdot \sin\theta_{max} \tag{8.15}$$

Through the aperture, the size of the e^-/p^+-beam on the detector will be

$$S_{e^-/p^+\text{-beam}} = W \times H = (w + 4r_c(p)) \times (h + 4r_c(p)) \tag{8.16}$$

as sketched in figure 8.14 **(a)**. Therefore, the maximum deviation induced by the gyration radius r_c relative to the drift D is

$$\frac{4\,r_c(p)}{D(p,\theta_3)} = \frac{4}{\alpha}\frac{\sin\theta_{max}}{f(\theta_3)} \approx \frac{4}{\alpha}\cdot\sqrt{\frac{B_3}{B_1}} \tag{8.17}$$

which is related to the mirror field B_1 and analysing field B_3, and the bending angle α.

***Beam hight** H **and curvature** R*

In the uniformly curved magnetic field, the magnetic field strength has a gradient along the direction of $\mathbf{R}$

$$\nabla \times \mathbf{B} = 0, \quad B_3 \cdot R_0 = B \cdot R \tag{8.18}$$

B_3 and R_0 are the field strength and the curvature along the central line of the tilted coils. The particles at different positions along **R** will experience deviated magnetic fields, thus have the drift

$$D = \frac{p}{qB_3} \cdot \alpha \cdot f(\theta_3) \cdot \frac{R}{R_0} = D_0 \frac{R}{R_0} = D_0 \frac{R_0 + y}{R_0} \tag{8.19}$$

where y is the vertical position of the particle on the detector relative to the beam center. The maximum deviation of the drift is

$$\frac{\Delta D}{D_0} = \frac{h + 4r_c}{R_0} = \frac{H}{R_0} \tag{8.20}$$

Hence the e^-/p^+-beam height relative to the field curvature H/R_0 tilts the particles distribution on the detector, as sketched in figure 8.14 **(b)**. For a detector only sensitive to x-position, the measured particle distribution is widened.

Particle distributions on detector

The corrections caused by r, H/R_0 and w influence the dispersion of the e^-/p^+particles in the drift spectrometer. Figure 8.14 shows the sketchy patterns of electrons at the detector affected by these factors.

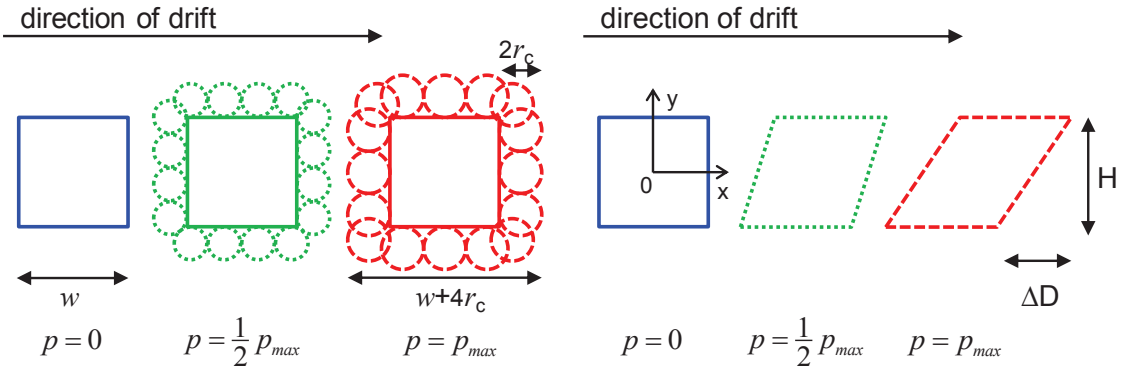

(a) Electron distribution influenced by w and r.

(b) Electron distribution influenced by H/R_0

Figure 8.14: Sketchy plots of the electron pattern on the detector with discrete momenta, influenced by w , r and H/R_0. p_{max} denotes the maximum electron momentum in free neutron decay.

Figure 8.15 shows the simulated distributions of electrons on the detector, with discrete momenta from 0 to 1.19 MeV/c.

The deviation of the drift caused by w is a constant, while that induced by r and H/R_0 are proportional to the drift distance. Hence at the low momentum range, the **R**×**B** spectrometer has better performance.

Furthermore, in normal magnetic spectrometer, the particles with very small momenta cannot be totally measured if their dispersion distances are smaller than the aperture width $D < w$. While as shown in figure 8.15, the **R**×**B** spectrometer doesn't have this limit. It can measure the full range of the momentum even when $p \to 0$.

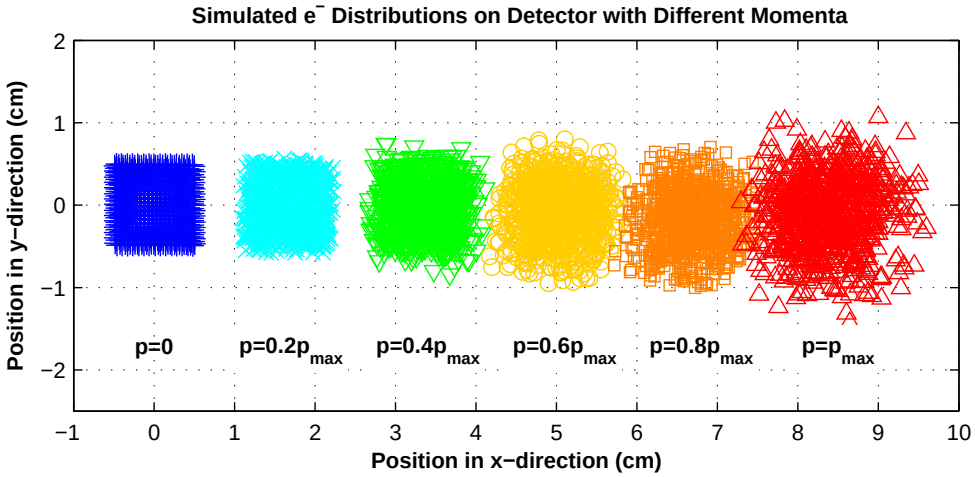

Figure 8.15: Simulated electron distribution on the detector of the **R**×**B** spectrometer with discrete momenta. p_{max} denotes the maximum electron momentum in free neutron decay as 1.19 MeV/c. The particles with $p \to 0$ can also be measured in the spectrometer. The deviations caused by r an H are proportional to the drift distance D.

8.2.4 Transfer function

The motions of the e^-/p^+particles in the **R**×**B** spectrometer are clearly defined during the drift processes. We are interested in the distribution of the e^-/p^+particles along the x-axis. The transfer function, i.e., the relation between the momentum spectrum $F(p)$ and the particle distribution on the detector $G(x)$, can be calculated and used in the data analyses. In this section, we discuss the transfer function including the corrections of r, w, and H. The negligible correction $f(\theta)$ is not considered here. And the higher order contributions, e.g., the R deviation induced by v_d, the r deviation induced by the B_3 gradient along R, are not taken into account in the transfer function.

Particle distribution from point source

We assume the $e^-/p^+$are homogeneously emitted in the decay volume of PERC. In addition, the size of the e^-/p^+-beam at the end of PERC is much larger than the size of the aperture's open window. Therefore, the particles that pass through the aperture, can be treated as emitting from the open window of the aperture.

If the particles are emitted from a point source at position $x = 0$ with given momentum and pitch angle, we can assume their gyration centers are homogeneously distributed on the circumference with radius $r(p,\theta)$. As shown in figure 8.16 **(a)**, the distribution density of the gyration centers along x-axis is

$$f(x,r) = \frac{\mathrm{d}N_{gyr.}}{\mathrm{d}x} = \frac{r(p,\theta)}{\pi\sqrt{r^2(p,\theta) - x^2}} \tag{8.21}$$

As shown in figure 8.16 **(b)**

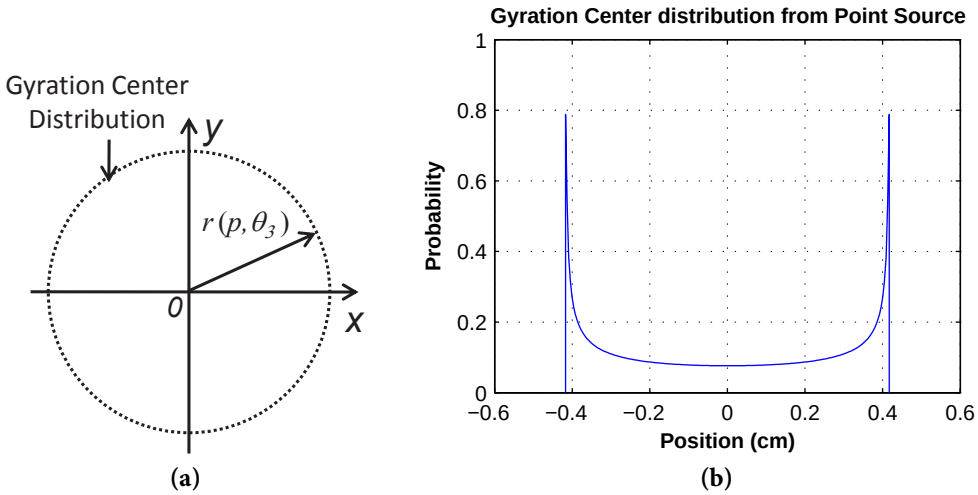

Figure 8.16: **(a)** Sketch of the distribution of gyration centers of the particles from a point source. **(b)** Gyration center distribution along x-axis.

With a certain gyration center, the particles are also homogeneously distributed in the circumference of $r(p,\theta)$. Hence their distribution density is the same as eqn. 8.21. The particle distribution according to the point source at $x = 0$ is then the integration

$$g(x,r) = \frac{\mathrm{d}N}{\mathrm{d}x} = \frac{1}{\pi^2}\int f(x',r)f(x-x',r)\mathrm{d}x' = [f(r) * f(r)](x) \tag{8.22}$$

which is the convolution of $f(x,r)$, as sketched in figure 8.17 **(a)**. Solving eqn. 8.22 results in [Dub08PSF]

$$g(x,p,\theta_3) = \frac{1}{\pi^2 r(p,\theta_3)} K\left(1 - \frac{x^2}{4r^2(p,\theta_3)}\right) \tag{8.23}$$

where K denotes the complete elliptical integral of the first kind. Figure 8.17 **(b)** shows the particle distribution from the point source according to eqn. form:PSF

Angular distribution of particles in B_3 field

We assume the unpolarized neutrons are applied in PERC experiments, thus the $e^-/p^+$are isotropically emitted in the decay volume as shown in eqn. 2.10. Their angular distribution in the field B_0 is

$$W_0(\theta_0) = \frac{\mathrm{d}N}{\mathrm{d}\theta_0} = \frac{1}{2}\sin\theta_0 \tag{8.24}$$

As stated in Section 4.3.1, when the particles propagate from B_0 to B_3, their angular distribution is transformed to

$$W(\theta_3) = \frac{\mathrm{d}N}{\mathrm{d}\theta_3} = \frac{1}{2}\frac{B_0}{B_3}\frac{\sin\theta_3\cos\theta_3}{\sqrt{1-\frac{B_0}{B_3}\sin^2\theta_3}} \quad \text{with} \quad 0 \leqslant \theta_3 \leqslant \theta_{max} \tag{8.25}$$

according to eqn. B.6.

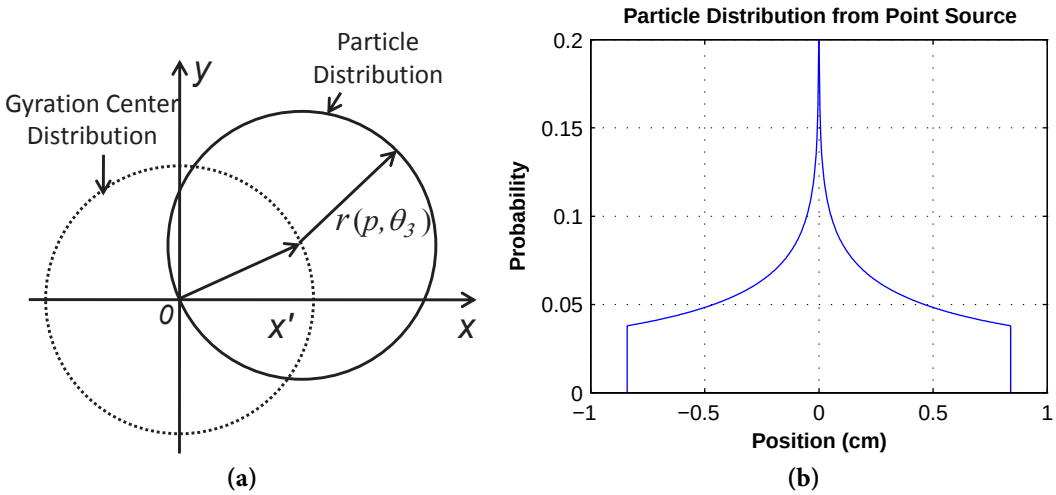

Figure 8.17: **(a)** Sketch of the distribution of the particles from a point source. **(b)** Particle distribution along x-axis.

If the aperture is sufficiently thin, it does not distort the angular distribution of the particles. We integrate eqn. 8.23 over θ_3, the particle distribution along the x-axis from a point source is then

$$L(x,p) = \int_0^{\theta_{max}} W(\theta_3) \cdot g(x,p,\theta_3)\, \mathrm{d}\theta_3 \tag{8.26}$$

Figure 8.18 **(a)** plots the distribution $L(x,p)$ of particles in the B_3 field with different momenta.

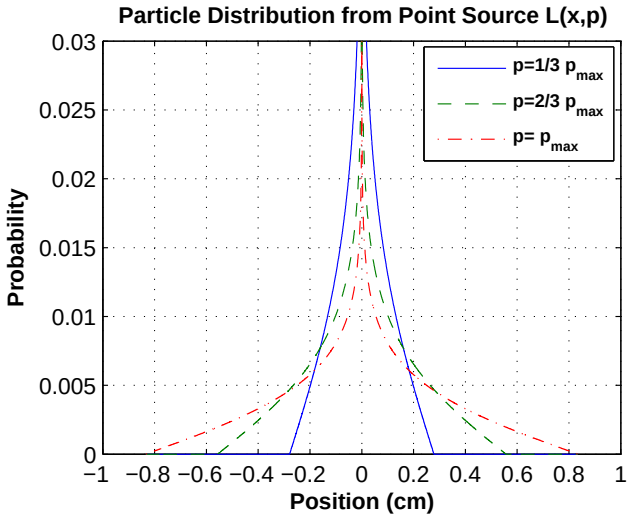

Figure 8.18: The distribution $L(x,p)$ of particles from a point source in the B_3 field along the x-axis, as given in eqn. 8.26. Different curves denote the particles with different momenta. p_{max} is the maximum momentum of e^-/p^+ in free neutron decay as 1.19 MeV/c.

Transmission function of aperture

Since the distance from the aperture to the detector is much longer than the helical pitches of the particles, we assume the particle distribution on the detector from any point in the aperture follows eqn. 8.26.

Define the transmission function of the aperture along the x-axis as

$$T(x) = \begin{cases} 1\ ; & -w/2 \leqslant x \leqslant w/2 \\ 0\ ; & x < -w/2\ ,\ x > w/2 \end{cases} \tag{8.27}$$

We treat the particles as emitted from the aperture's open window. On the detector, the particles then have a distribution of

$$P(x,p) = [T * L(p)](x) \tag{8.28}$$

which is the convolution of the aperture function $T(x)$ and the distribution $L(x,p)$ of point source.

Correction of H

For the correction of beam height H, we consider the particle distribution along the y-axis. For simplicity, we use the condition $w = h$, so the distribution along the y-axis is the same as eqn. 8.28, i.e., $P(y,p)$.

Since the factor H/R_0 tilts the particle distribution on detector, $P(y,p)$ is projected on the x-axis. From eqn. 8.19, the momentum p is given, so D_0 is constant. We set the position D_0 as zero point x=0, then we have

$$x = D - D_0 = \frac{D_0}{R_0} y \quad \text{and} \quad \mathrm{d}x = \mathrm{d}y \frac{D_0}{R_0} \tag{8.29}$$

If the projection of $P(y,p)$ on x-axis is written as $Q(x,p)$, we have

$$P(y,p)\mathrm{d}y = Q(x,p)\mathrm{d}x \tag{8.30}$$

so

$$Q(x,p) = \frac{\mathrm{d}y}{\mathrm{d}x} P(y,p) = \frac{R_0}{D_0(p)} \cdot P\left(\frac{x \cdot R_0}{D_0(p)}, p\right) \tag{8.31}$$

Transfer function

All together, we take the corrections related to r, w, H, as well as the drift $D(p)$ into account. The total transfer function is then the convolution of the distributions in eqn. 8.28 and eqn. 8.31

$$M(x,p) = [P(p) * Q(p)](x - D(p)) \tag{8.32}$$

For a given momentum spectrum $F(p)$, the particle distribution on the detector can be derived

$$G(x) = \int_0^{p_{max}} M(x,p) \cdot F(p)\ \mathrm{d}p \tag{8.33}$$

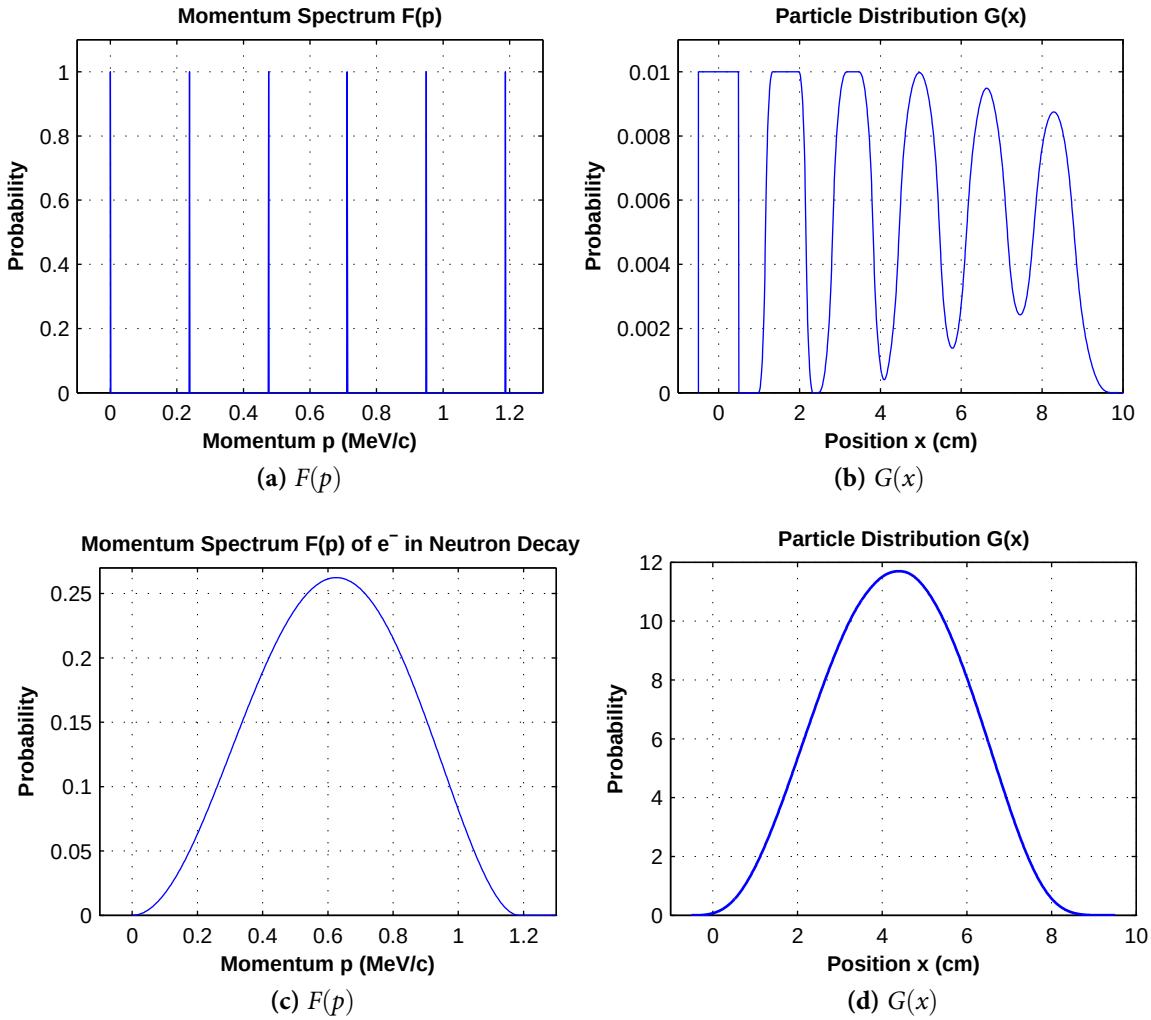

(a) $F(p)$ **(b)** $G(x)$ **(c)** $F(p)$ **(d)** $G(x)$

Figure 8.19: Examples of given $F(p)$ and resulted $G(x)$ according to eqn. 8.33. Figures **(a)** and **(b)** denote discrete momentum and position distribution same as shown in figure 8.15. Figures **(c)** and **(d)** denote the theoretical momentum spectrum of electrons in free neutron decay and their position distribution.

Figure 8.19 shows the examples of the given momentum spectra $F(p)$ and the resulted $G(x)$ from Eq. 8.33.

In experiments, $G(x)$ is measured by the position sensitive detectors. One is able to fit the momentum spectrum $F(p)$ to $G(x)$ with eqn. 8.33.

Resolution of Momentum and Reconstruction of $F(p)$

Eqn. 8.33 is the Fredholm integral equation of first type, and $M(x, p)$ is the kernel function. In principle, we are able to calculate $F(p)$ directly from measured $G(x)$ by solving the equation. However, $M(x, p)$ is so complicated that we can not find an analytical solution.

A numerical solvent of this problem is to convert the integral into the quadrature calculation, the $F(p)$ and $G(x)$ into arrays, thus convert the kernel function $M(x,p)$ into a square matrix [Del88, Pre07]. Eqn. 8.33 then can be written as

$$\mathbf{G} = \mathbf{M} \cdot \mathbf{F} \tag{8.34}$$

and the momentum spectrum **F** can be reconstructed with the inverse matrix of **M**

$$\mathbf{F} = \mathbf{M}^{-1} \cdot \mathbf{G} \tag{8.35}$$

In case that **M** is reversible, it should be a square matrix. Therefore, the **G** and **F** have the same number of rows, thus the same resolution. In the standard configuration, if **G** has a resolution of 1 mm, the momentum spectrum **F** can reach a resolution of 14.4 keV/c.

However, one problem arises in this special case, that the kernel matrix **M** is nearly singular. The behaviour of this problem is that the reconstructed **F** is very sensitive to the errors of **G**. A little deviation of **G** from theoretical value will result in huge oscillation of **F**. Figure 8.20 shows examples of the evaluated **F**, when we introduce small errors in **G** of figure 8.19 **(d)**.

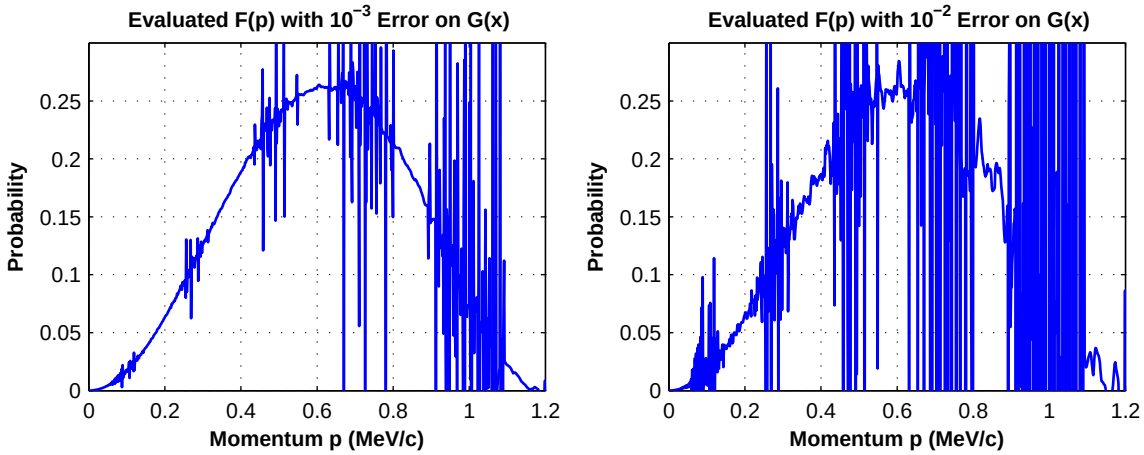

(a) 10^{-3} error on **G**. **(b)** 10^{-2} error on **G**.

Figure 8.20: Examples of evaluation of **F** from **G** with eqn. 8.35. **G** is from figure 8.19 **(d)**. When we introduce 10^{-3} and 10^{-2} deviations on one element of **G**, the resulted **F** oscillates hugely.

The possible solution for that is to regularize the kernel matrix **M**. Some of the methods are introduced in [Del88] and [Pre07].

High Order Aberrations of the Transfer Function.

The transfer function in this section only considers the motions of the e^-/p^+particles to the first order. The higher order contributions including the acceleration $\dot{\mathbf{v}}_d \times \mathbf{B}$ in eqn. B.13 is related to B_3 homogeneity, and introduce the drift **D** along **R** direction. If B_3 fluctuate around a average value, the $\dot{\mathbf{v}}_d$ term cancels itself. We think this aberration is small.

Another aberration is the r variation due to field deviation ΔB_3 along R. Since we have

$$B_0 r_0^2 = B r^2 \quad \text{and} \quad B_0 R_0 = BR \tag{8.36}$$

The maximum deviation of r is

$$\frac{\Delta r}{r_0} = \sqrt{1 + \frac{H}{2R_0}} - \sqrt{1 - \frac{H}{2R_0}} = 2.3\% \tag{8.37}$$

Another aberration is the curvature $\mathbf{R}$ deviation. During the drifts, the real curvature has the contribution from the drift distance D

$$\mathbf{R} = \mathbf{R}_0 + \mathbf{D} \tag{8.38}$$

Hence the face of $\mathbf{R}$ is no longer vertical to $\mathbf{B}$. The $\mathbf{R}\times\mathbf{B}$ term can induce the drift along minus $\mathbf{R}_0$ direction. From simulation in figure 8.15, we can see the y positions of particles decreases with the drift distance. This contribution introduces more complicated corrections. For a rough estimation, the induced deviation of D is

$$\frac{\Delta D}{D_0} = 1 - \cos\frac{D_0}{R_0} = 2.5 \times 10^{-2} \tag{8.39}$$

As for other high order contributions, we need more precise description of the particle motion in magnetic field, which is related to plasma physics.

8.2.5 Event rate estimation

If we apply the $\mathbf{R}\times\mathbf{B}$ drift spectrometer after PERC, the event rate of the spectrometer N_d is proportional to that of PERC N_{PERC}

$$N_d = N_{PERC}\frac{B_3 \cdot w \cdot h}{B_0 \cdot s_0} \tag{8.40}$$

s_0 and B_0 are the e^-/p^+-beam size and magnetic field at the decay volume, with values of 5×5 cm^2 (e^-/p^+-window considered) and 1.5 T respectively.

With the PERC event rates in table 6.2 and the standard configuration in table 8.3, the event rates of the $\mathbf{R}\times\mathbf{B}$ drift spectrometer are listed in table 8.4. The selector field of PERC B_1 is set as 6 T. [3]

[3] To reduce the influences of gyration radius r, B_1 should be as high as possible. The cases with B_1 less than 6 T are not considered in the spectrometer design.

Beam Mode	Cont. Unpol.	Cont. Pol.	Pulse. Unpol.	Pulse. Pol.
Event Rate	440 Hz	88 Hz	22 Hz	4.4 Hz

Table 8.4: Estimated event rate of **R**×**B** spectrometer after PERC. The selector field B_1 is set as 6 T.

8.2.6 Conclusion

The **R**×**B** drift spectrometer offers the opportunity of momentum measurements of charged particles in the instrument with guiding fields, in which case the normal magnetic spectrometers cannot work well. In this proposed drift spectrometer, the guiding field is not eliminated, but gradually evolved to the analysing field. The drifts of the particles in the uniformly curved magnetic field have similar behaviours as in the normal dispersive magnetic spectrometer.

The **R**×**B** spectrometer has the advantages:

- *Adiabatic transports of particles.*

  As shown in figure 8.12, from the guiding field to the detector of the **R**×**B** spectrometer, the charged particles can be adiabatically transported. The angular distribution of the particles can be kept and measured.

- *Low momentum measurements.*

  As shown in figure 8.15, the particles with very small momentum $p \rightarrow 0$ can be measured in the **R**×**B** spectrometer, while they cannot be totally detected in normal magnetic spectrometer if their dispersion $D < w$.

- *Large acceptance of incident angle.*

  As shown in figure 8.13, when $\theta \leqslant 9.6^{o}$, corresponding to 88 msr solid angle, the direct aberration induced by the e^{-}/p^{+}incident angle is very small as less than 10^{-4}.

As a conceptual design of **R**×**B** spectrometer, the particle drifts are considerably influenced by the systematics related to both the instrument and the particle properties. Table 8.5 lists the maximum sizes of the corrections in the standard configuration.

Correction	Comment	Max. Size
$4r_c/D$	Gyration Radius	2.0×10^{-1}
w/D_{max}	Aperture Width	1.2×10^{-1}
H/R_0	Aperture Height	6.7×10^{-2}
ΔB_3	Field Homogeneity	8×10^{-3}
$f(\theta_{max})$	Incident Angle	8×10^{-5}
$O(v_d)$	High Order Contribution	2.5×10^{-2}

Table 8.5: Estimated maximum correction sizes on the e^{-}/p^{+}particles dispersion in the **R**×**B** spectrometer.

However, the motions of the e^-/p^+particles are clearly defined during the drifts, thus the transfer function of the particles can be well known. Experimentally, one is able to fit the momentum spectrum $F(p)$ to the measured particle distribution $G(x)$, or numerically evaluate $F(p)$ from $G(x)$. In the standard configuration, if the position detector has a resolution of 1 mm, the momentum spectra can reach a resolution of 14.4 keV/c. Additionally, by performing detector calibration with defined particle sources, the systematic errors can be controlled at low level.

Besides, there is also room for improvement of the $\mathbf{R}\times\mathbf{B}$ spectrometer design. For further development, we can decrease the corrections. By increasing the bending angle α, and decreasing the analysing magnetic field B_3, we can enlarge the drift D, and reduce the r correction. But decreasing B_3 also reduces the event rate, and introduce more difficulties in homogenizing of the field. By increasing the curvature R, we can reduce the corrections of H and higher order contributions. Figure 8.21 shows the relation between the parameters and the systematic effects.

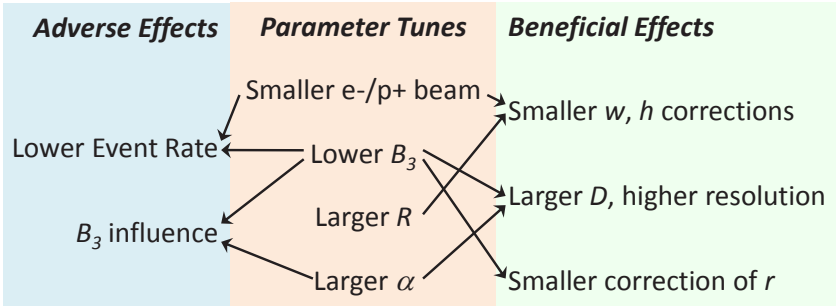

Figure 8.21: Diagram of the relations between the parameters of spectrometer and the caused adverse and benificial effects.

Additionally, more accurate transfer function can be calculated analytically, and results in 2-dimensional particle distribution on detector. In future investigation, the transfer function can also be determined numerically with a desired precision, e.g., precise simulation of e^-/p^+trajectories.

As a summary, we list the open questions of the $\mathbf{R}\times\mathbf{B}$ spectrometer in future developments:

- *Manufacture.*

  The manufacture of the system with series of tilted normal Cu coils or superconducting coils is difficult.

- *Large corrections.*

  The corrections caused by gyration radius r and the incident beam height H are large.

- *Control of the magnetic field homogeneity.*

  The analysing field B_3 should be homogeneous in the cross-section of e^-/p^+-beam, and along the magnetic line. Considering the strong influences from PERC, the homogeneity of B_3 is difficult to be controlled.

- *High order contributions.*

  Precise calculations of the high contributions need to be done.

8.3 Possible Post Spectrometers of PERC

As introduced in Chapter 6, PERC can supply general-purpose e^-/p^+-beam that is able to be used in various experiments by applying different post spectrometers after PERC. In this section, we give sketchy introductions to two possible post spectrometers. Detailed properties and reliabilities of these post spectrometers should be well studied in other works.

8.3.1 PERKEOIII

Because of the dromedary geometry of PERC instrument, it is difficult to achieve the real time neutron polarization measurement during the e^-/p^+detection, as stated in Section 7.1. One possible solution is to use one detector vessel of PERKEOIII as the post spectrometer. Figure 8.22 shows the possible structure with PERKEOIII detector vessel after PERC.

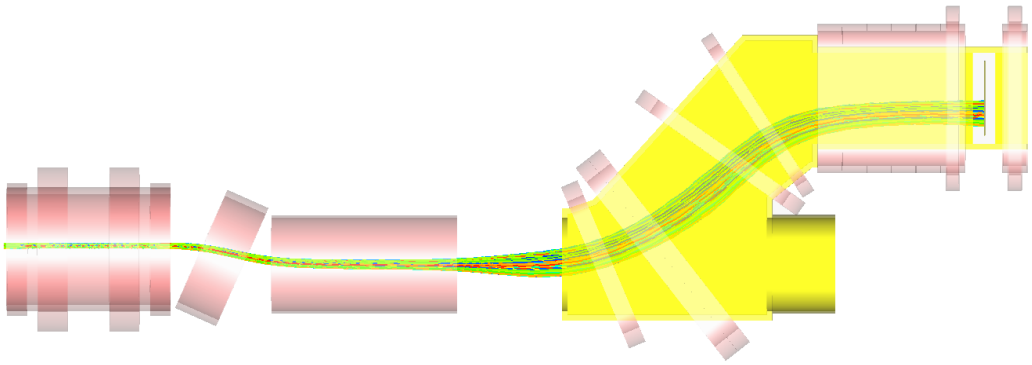

Figure 8.22: Geometry of PERC and PERKEOIII detector vessel as post spectrometer, and the simulated trajectories of electrons from the decay volume.

Since the n-beam and e-beam have overlap in the PERC detector coil, only pulsed n-beam can be applied in the experiment. Assuming PERC can supply the effective decay volume of 6 m (Section 7.3.3), and the background $B(E)$ measurement and neutron absorption take twice time as $S(E)$, then the measurement efficiency t_{signal}/t_{total} can reach about 23%, comparable with the case of PERKEOIII that has t_{signal}/t_{total} = 1.4 ms/10.6 ms = 13% (Section 4.2).

8.3.2 aSPECT

The instrument aSPECT is a retardation spectrometer for measurement of angular correlation coefficient a that between $\bar{\nu}_e$ and p^+ momenta in the neutron β decay [Zim00, Bae08,

Sim09, Kon11]. By applying static electrodes, aSPECT measures the spectrum of the decay protons which pass a electrical barrier. If we rotate aSPECT by 90°, there is possibility to use aSPECT as the post spectrometer after PERC. Figure 8.23 shows the geometry of magnetic coils of the combined system, and the proton trajectories.

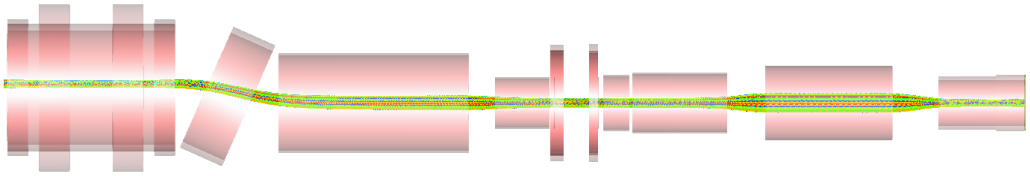

Figure 8.23: PERC system with aSPECT as post spectrometer. The magnets configuration of aSPECT is supplied by Dr. G. Konrad of Atominstitut TU-Wien.

The magnetic field along the proton beam is plotted in figure 8.24.

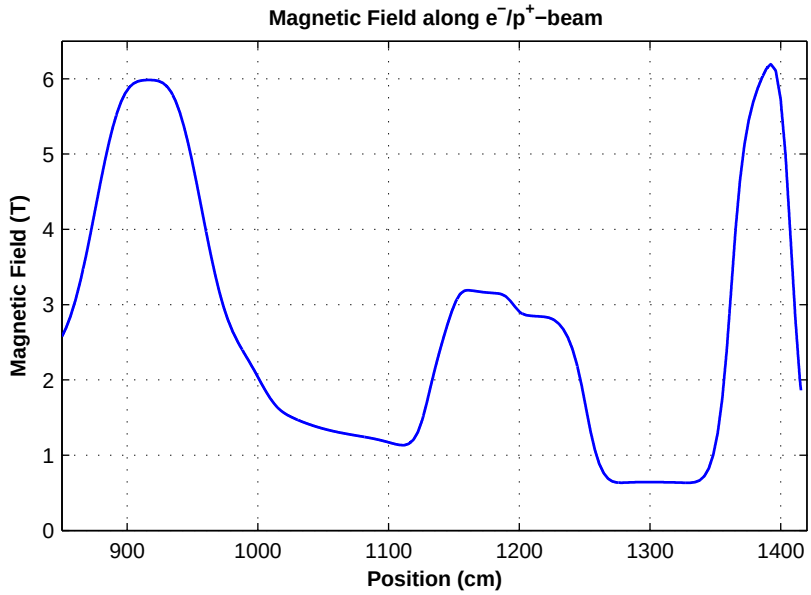

Figure 8.24: Magnetic field strength along the proton beam from PERC selector coil to aSPECT.

As shown in figure 8.24, there are two field minima in PERC detector coil and in aSPECT. To eliminate the trapped protons, electrodes for $\mathbf{E}\times\mathbf{B}$ drifts are probably needed in the detector coil.

Chapter 9

Summary and Outlook

The β-decay of free neutron, which played a prominent role in the developments of particle physics and cosmology, also provides a unique platform for the researches in forefront of physics nowadays. By investigating the observables in the free neutron decay precisely, a lot of quantities in and beyond the Standard Model can be tested.

From the first PERKEO spectrometer developed in 1986, there has been three generations of instruments and tens of experiments, which have done precise measurements of various quantities in free neutron decay. For the PERKEOIII experiment in 2008-2009, the β asymmetry, i.e. the electron angular correlation coefficient A was measured. It is the first time for PERKEO series instruments to use pulsed neutron beam as the decay source. The neutron pulses provide an additional time scale on the measurement, in which case the data can be selected with specified time ranges. Therefore, systematic errors caused by the edge effect and magnetic inhomogeneity are highly suppressed.

In the mean time, the properties of the neutron pulse and the magnetic field become important. From the simulation, the complicated properties of neutron beam are able to be studied in detail. In the data analyses, we used the neutron simulation to determine the time windows for data selections, also to calculate the corrections of magnetic mirror effect. With the information from neutron and magnetic field simulations, the corrections are determined with high precisions.

With the statistics of 9 months measurements, we deduce the preliminary result of the coefficient A, further the ratio of the Axial-vector and Vector coupling strengths λ. Solely from the statistics point of view, the PERKEOIII results are 5 times more precise than the latest values.

As the next generation of decay product spectrometer, the beam station PERC aims to measure the observables in free neutron decay with distortion-free on the level of 10^{-4}. To realize the precise measurements, as a unique feature, PERC has a specified functional magnetic field distribution, which is supplied by a set of superconducting magnets. With the application of the magnetic mirror, we are able to select the e^-/p^+signals due to their emission angles, and the measurements can obtain high efficiencies and suppressed error levels.

In order to acquire the expected performance, the magnetic field system of PERC, the behaviours of the charged particles in the instrument, and the related systematics, are delicately designed and studied.

The magnets system of PERC shows a dromedary geometry, with which the background can be highly decreased by the beamstop. However, the unsymmetric geometry also causes considerable changes of e^-/p^+-beam due to the selector field variation. We study the properties of the magnetic field, the trajectories of e^-/p^+particles, as well as the related systematic effects, and optimize the magnet system.

The practical and experimental factors are considered in the design of PERC, including the necessary spaces in the magnets system, the inductances of the coils, the properties of superconducting wire, magnetic field shielding and the magnetic forces and torques on the components. These factors also need to be taken into account in the manufacture of the instrument.

Because of the strong magnetic field of PERC, we did not find a practical solution for eliminating the guiding field in a magnetic spectrometer. In order to achieve the momentum analysis, we propose a method of $\mathbf{R}\times\mathbf{B}$ drift spectrometer, which disperses the e^-/p^+particles due to their drift effects in the curved magnetic field. In the $\mathbf{R}\times\mathbf{B}$ spectrometer, the strong field of PERC is not eliminated, but smoothly guided and bended, and the e^-/p^+particles can be adiabatically transported and analysed. The e^-/p^+dispersion in $\mathbf{R}\times\mathbf{B}$ spectrometer have similarities as that in magnetic spectrometer, and the $\mathbf{R}\times\mathbf{B}$ spectrometer has some features better than normal magnetic spectrometer.

In future developments, the detection system for electron and proton measurements can be improved. The scintillator detector as used in PERKEOIII has the errors from calibration, position dependencies etc., and the Silicon detector normally has high backscattering probabilities. To test the new physics on 10^{-4} level, the detector should also reach a higher precision than now.

From the theories point of view, there is also opportunities to search other quantities which are measurable in PERC, as well as new methods for the measurements.

Appendix A

Introduction to $V-A$ Theory and Free Neutron Decay

The Fermi's theory and the resultant $V-A$ theory are kinds of phenomenological theories, that represent the weak interaction as the contact couplings of charged currents. Compare with later electroweak theory, the $V-A$ theories have some limits

- The $V-A$ theory is not a gauge theory, and the contact interaction is not renormalizable. The high order processes, e.g. the loop diagram can not be calculated.
- The $V-A$ theory is only valid when the momentum transfer $q \ll m_W$.
- The $V-A$ theory only explains the charged transition current. The phenomenons of neutral currents, e.g. neutrino scattering, are not included in the theory.

However, in the processes of nucleus and neutron decays, the $V-A$ theory works very well.

In this chapter, we provide an introduction to the Fermi's theory, and the deduction of the $V-A$ theory with helicity operator. From the deduction, we can get better understanding of the principle of the current-current couplings, and see the possibilities of searching new physics beyond Standard Model. The deductions are from [Gre00].

A.1 Fermi's Theory and Proper Operators

In Fermi's theory, the neutron decay is described by the interaction term in Hamiltonian

$$H_{int} = \frac{G_F}{\sqrt{2}} \sum_i C_i \int (\bar{u}_p \hat{O}_i u_n)(\bar{u}_e \hat{O}_i u_\nu) \mathrm{d}x^3 = \frac{G_F}{\sqrt{2}} \sum_i C_i \int J_H^i J_L^i \mathrm{d}x^3 \tag{A.1}$$

$u_{p,n,e,\nu}$ are 4-component Dirac spinors of the four particles, the bars on them denote their Dirac adjoints, which have the relations with their Hermitian conjugates

$$\bar{u}_k = u^\dagger \gamma_0, \quad k = p, n, e, \nu. \tag{A.2}$$

J_H and J_L denote the hadronic and leptonic transition currents. The proper operators $\hat{O}_i$ that characterize the decay process, are weighted by constants C_i. Since u_k are 4-spinors, the $\hat{O}_i$ should to be 4×4 spin matrices.

Further, the Hamiltonian should transform like the time component of the 4-momentum vector. Therefore, the H_{int} as an integration over the space, is required to be a Lorentz scalar, hence the transition currents J must be proper quantities under Lorentz transformation. Under this general condition, it can be proven the operators $\hat{O}_i$ must be one of the 16 possibilities, which are arranged in 5 categories

$$1, \quad \gamma^\mu, \quad \sigma^{\mu\nu}, \quad \gamma^\mu\gamma_5, \quad \gamma_5 \tag{A.3}$$

with σ and γ_5

$$\sigma^{\mu\nu} = \frac{i}{2}[\gamma^\mu\ \gamma^\nu], \quad \gamma_5 = i\gamma^0\gamma^1\gamma^2\gamma^3 \tag{A.4}$$

It can be shown that, under the Lorentz transformation and space inversion (parity transformation), the transition current with these operators $J^i = \bar{u}\hat{O}_i u$ behave as Scalar (S), Vector (V), Tensor (T), Axial vector (A) and Pseudo scalar (P) quantities. Table A.1 lists the categories of the operators and behaviours of the resulted transition currents.

$\hat{O}_i$	$\bar{u}\hat{O}_i u$ under L & P Transform.	Number of Matrics	$\hat{O}'_i$=$\hat{P}_+\hat{O}_i\hat{P}_-$
1	Scalar (S)	1	0
γ^μ	Vector (V)	4	$\frac{1}{2}\gamma^\mu(1-\gamma_5)$
$\sigma^{\mu\nu}$	Tensor (T)	6	0
$\gamma^\mu\gamma_5$	Axial Vector (A)	4	$-\frac{1}{2}\gamma^\mu(1-\gamma_5)$
γ_5	Pseudoscalar (P)	1	0

Table A.1: Possibilities of the operators $\hat{O}_i$ and their properties under Lorentz and Parity transformations, and chirality projection.

The interaction Hamiltonian of the weak processes should be the combination of the 5 kinds of currents couplings.

A.2 Hadronic Current in Low Energy Limit

In the nucleus or neutron decay, the nucleus, or the neutron and the proton move non-relativistically. Hence the upper 2-spinors ϕ in the wave functions of the nucleus are much larger than the lower 2-spinors χ.

$$\Psi_n = \begin{pmatrix}\phi\\ \chi\end{pmatrix}, \quad \phi \gg \chi \tag{A.5}$$

In case we neglect the small χ component, the hadronic current can be simplified.

With the properties of the γ matrices [1]

$$\gamma^0 = \beta = \begin{pmatrix}1 & 0\\ 0 & -1\end{pmatrix}, \ (\gamma^0)^\dagger = \gamma^0, \ \gamma^0\gamma^0 = 1, \ \gamma_5 = \begin{pmatrix}0 & 1\\ 1 & 0\end{pmatrix} \tag{A.6}$$

[1] Please distinguish the 4×4 tensor $\sigma^{\mu\nu}$ matrix and the 2×2 Pauli matrix $\boldsymbol{\sigma}_k$.

$$\boldsymbol{\alpha}_k = \begin{pmatrix} 0 & \boldsymbol{\sigma}_k \\ \boldsymbol{\sigma}_k & 0 \end{pmatrix}, \ \gamma_k = \beta\boldsymbol{\alpha}_k, \ \gamma_k^\dagger = -\gamma_k, \ k = 1,2,3. \tag{A.7}$$

$$\gamma_5^\dagger = \gamma_5, \ \gamma_5\gamma_5 = 1, \ \{\gamma^\mu, \gamma_5\} = \gamma^\mu\gamma_5 + \gamma_5\gamma^\mu = 0, \ \mu = 0,1,2,3 \tag{A.8}$$

we can derive the scalar hadronic current in low energy limit [GT36]

$$S = \bar{u}_p u_n = (\phi_p^\dagger, \chi_p^\dagger)\gamma^0 \begin{pmatrix} \phi_n \\ \chi_n \end{pmatrix} = \phi_p^\dagger\phi_n - \chi_p^\dagger\chi_n \to \phi_p^\dagger\phi_n \tag{A.9}$$

The 4-component vector current is

$$\begin{aligned} V =& \{\bar{u}_p\gamma^0 u_n, \bar{u}_p\gamma_k u_n\} = \left\{ (\phi_p^\dagger, \chi_p^\dagger)\begin{pmatrix} \phi_n \\ \chi_n \end{pmatrix}, (\phi_p^\dagger, \chi_p^\dagger)\boldsymbol{\alpha}_k\begin{pmatrix} \phi_n \\ \chi_n \end{pmatrix} \right\} \\ =& \{\phi_p^\dagger\phi_n + \chi_p^\dagger\chi_n, \phi_p^\dagger\boldsymbol{\sigma}_k\chi_n + \chi_p^\dagger\boldsymbol{\sigma}_k\phi_n\} \to \{\phi_p^\dagger\phi_n, \mathbf{0}\} \end{aligned} \tag{A.10}$$

that only the zero component remains.

For the axial current

$$\begin{aligned} A =& \{\bar{u}_p\gamma^0\gamma_5 u_n, \bar{u}_p\gamma_k\gamma_5 u_n\} = \left\{ (\phi_p^\dagger, \chi_p^\dagger)\begin{pmatrix} \chi_n \\ \phi_n \end{pmatrix}, (\phi_p^\dagger, \chi_p^\dagger)\boldsymbol{\alpha}_k\begin{pmatrix} \chi_n \\ \phi_n \end{pmatrix} \right\} \\ =& \{\phi_p^\dagger\chi_n + \chi_p^\dagger\phi_n, \phi_p^\dagger\boldsymbol{\sigma}_k\phi_n + \chi_p^\dagger\boldsymbol{\sigma}_k\chi_n\} \to \{0, \phi_p^\dagger\boldsymbol{\sigma}_k\phi_n\} \end{aligned} \tag{A.11}$$

the zero component vanishes, but the 3-component spatial part remains.

For the tensor elements σ^{0k}, when $k = 1,2,3$

$$\sigma^{0k} = i\boldsymbol{\alpha}_k = i\begin{pmatrix} 0 & \boldsymbol{\sigma}_k \\ \boldsymbol{\sigma}_k & 0 \end{pmatrix}, \quad \text{when } i = 1,2,3. \tag{A.12}$$

The corresponding elements in the tensor are

$$\bar{u}_p\sigma^{0k}u_n = i(\phi_p^\dagger, \chi_p^\dagger)\gamma^0\begin{pmatrix} 0 & \boldsymbol{\sigma}_k \\ \boldsymbol{\sigma}_k & 0 \end{pmatrix}\begin{pmatrix} \phi_n \\ \chi_n \end{pmatrix} = i\phi_p^\dagger\boldsymbol{\sigma}_k\chi_n - i\chi_p^\dagger\boldsymbol{\sigma}_k\phi_n \to 0 \tag{A.13}$$

For the T elements σ^{ij} when $i,j = 1,2,3$, it can be proven

$$\sigma^{ij} = \begin{pmatrix} \boldsymbol{\sigma}_k & 0 \\ 0 & \boldsymbol{\sigma}_k \end{pmatrix}, \quad \text{when } i,j,k = 1,2,3. \tag{A.14}$$

The corresponding elements are

$$\bar{u}_p\sigma^{ij}u_n = (\phi_p^\dagger, \chi_p^\dagger)\gamma^0\begin{pmatrix} \boldsymbol{\sigma}_k & 0 \\ 0 & \boldsymbol{\sigma}_k \end{pmatrix}\begin{pmatrix} \phi_n \\ \chi_n \end{pmatrix} = \phi_p^\dagger\boldsymbol{\sigma}_k\phi_n - \chi_p^\dagger\boldsymbol{\sigma}_k\chi_n \to \phi_p^\dagger\boldsymbol{\sigma}_k\phi_n \tag{A.15}$$

All together, the tensor current is

$$T \to \phi_p^\dagger\boldsymbol{\sigma}_k\phi_n \tag{A.16}$$

The pseudo scalar current is

$$P = \bar{u}_p\gamma_5 u_n = (\phi_p^\dagger, \chi_p^\dagger)\gamma^0\begin{pmatrix} \chi_n \\ \phi_n \end{pmatrix} = \phi_p^\dagger\gamma^0\chi_n + \chi_p^\dagger\gamma^0\phi_n \to 0 \tag{A.17}$$

which vanishes in low energy limit of nucleus decay.

A.3 Fermi and Gamov-Teller Transitions and Electron Emission Probability

As a conclusion of above section, the transition currents in low energy neutron decay are simplified as

$$S, V \to \phi_p^\dagger \phi_n, \qquad A, T \to \phi_p^\dagger \boldsymbol{\sigma}_k \phi_n, \qquad P \to 0 \tag{A.18}$$

The S, V transitions are named as Fermi transitions. In the Fermi transition, the nucleus spin remains unchanged. Because of the spin conservation, the spins of e^- and $\bar{\nu}_e$ are reverse, and can point to any directions.

The transitions in A, T currents are named as Gamov-Teller (GT) transitions. In contrast to Fermi transition, the spin of the nucleus in GT transitions changes due to the operation of $\boldsymbol{\sigma}_k$. Therefore, both e^- and $\bar{\nu}_e$ must have the same spin direction as the initial neutron spin. A sketch of the spin states of the particles in nucleus decay is shown in figure A.1.

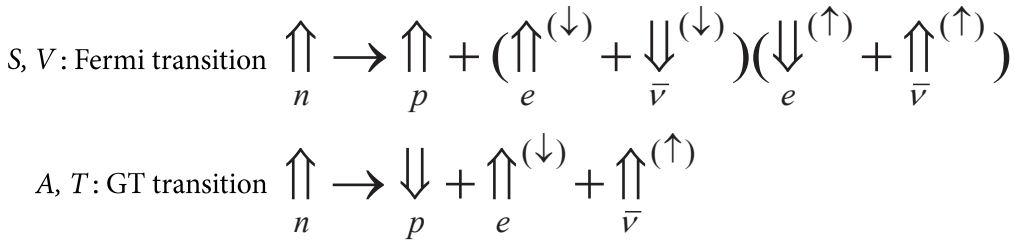

Figure A.1: A rough sketch of the spin states (double arrows) of the particles in Fermi transition and Gamov-Teller transition. The small arrows denote the motion of e^- and $\bar{\nu}$ when assuming the leptons have negative helicities.

If we assume the emitted leptons have only negative helicity, the electrons momentum should always be opposite to their spins, and the anti-neutrino momentum should be same as their spins. Therefore in Fermi transition, the electrons can be emitted arbitrarily to the neutron spin, whereas in GT transition, the electron motions are limited in the opposite direction to the neutron spin.

In the Wu's experiments [Wu57], the $^{60}Co(5\hbar)$ nucleus in the decay

$$^{60}Co(5\hbar) \to {}^{60}Ni(4\hbar) + e^-(\hbar/2) + \bar{\nu}_e(\hbar/2) \tag{A.19}$$

is changed by $\hbar$, hence the process is pure GT transition. Assume the ^{60}Co spin is on the plus z-axis, the electron momentum $\mathbf{p}$ has an angle θ to z-axis. The eigenfunction of electron with negative helicity can be obtained by solving Dirac equation

$$\varphi(t) = N\begin{pmatrix} \chi \\ -a\chi \end{pmatrix} e^{i(\mathbf{p}\cdot\mathbf{r}-Et)/\hbar}, \quad \text{with } a = \frac{E - m_0c^2}{cp}, \ \chi = \begin{pmatrix} -\sin\frac{\theta}{2} \\ \cos\frac{\theta}{2} \end{pmatrix} \tag{A.20}$$

Due to the spin conservation, the only part of wave function that can contribute to the process, is the function which polarized in the same direction as ^{60}Co nuclei, namely the

plus z-direction. The function of electron with negative helicity thus has the momentum in minus z-direction, i.e. the emission angle $\theta = \pi$

$$\chi^{(-)}_{\theta=\pi} = \begin{pmatrix} -1 \\ 0 \end{pmatrix} \tag{A.21}$$

Therefore, the probability of electron emission is then the overlap of the spinors (assuming electrons are highly relativistic)

$$W(\theta) = |\langle \chi^{(-)}_{\theta=\pi} | \chi^{(-)}_{\theta} \rangle|^2 \propto \sin^2 \frac{\theta}{2} = \frac{1}{2}(1 - \cos\theta) \tag{A.22}$$

as plotted in figure A.2 **(b)**. In this case, the electrons are mostly emitted opposite to the nucleus spin, which is exactly the phenomenon discovered in Wu's experiment.

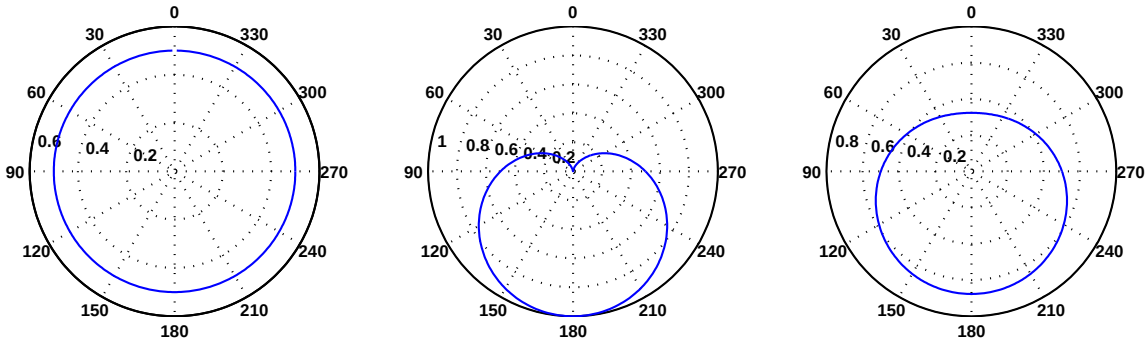

(a) Fermi Transition **(b)** GT Transition **(c)** Free Neutron Decay

Figure A.2: Sketches of electron emission probabilities in nucleus decay. **(a)** In Fermi transition, electrons are emitted isotropically. **(b)** In GT transition, electron are predominantly emitted opposite to neutron spin, as discovered in Wu's experiment. **(c)** In case of free neutron decay, the process is a combination of the two transitions, which are weighed by the coupling constants g_V and g_A. The ratio $\lambda = g_A/g_V$ determines the asymmetry of electron emissions. Neutron spin states in the plots are in 0^o direction.

A.4 $V-A$ Theory

Based on the Fermi's theory and the assumption of maximal P-violation, the $V-A$ theory was developed in 1957-1958 with different methods. In this section, we derive the $V-A$ theory with the helicity operator Λ.

From the experiments [Wu57] and [Gol58], it was found only leptons of negative helicities participate in the weak interaction. The helicity operator in quantum theory is

$$\hat{\Lambda} = \frac{\hat{\boldsymbol{\Sigma}} \cdot \mathbf{p}}{p}, \quad p = |\mathbf{p}| \tag{A.23}$$

$\hat{\Sigma}_i$ are 4×4 Pauli matrices

$$\hat{\mathbf{\Sigma}}_k = \begin{pmatrix} \boldsymbol{\sigma}_k & 0 \\ 0 & \boldsymbol{\sigma}_k \end{pmatrix}, \quad k = 1, 2, 3. \tag{A.24}$$

It can be proven, the helicity operator has only ±1 eigenvalues, for the positive and negative helicity eigenstates.

$$\hat{\Lambda} u^{(\pm)} = \pm u^{(\pm)} \tag{A.25}$$

An arbitrary wave function can be decomposed into two components with positive and negative helicities

$$u = u^{(+)} + u^{(-)} \tag{A.26}$$

We can define the projection operators

$$\hat{P}_\pm = \frac{1 \pm \hat{\Lambda}}{2} \tag{A.27}$$

to project the components of positive and negative helicity out of the arbitrary spinor

$$\hat{P}_+ u = u^{(+)}, \quad \hat{P}_- u = u^{(-)} \tag{A.28}$$

However, neither $\hat{\Lambda}$ nor $\hat{P}_\pm$ are Lorentz invariant. It can be understood when we change the observing frame. When a real particle moves with a velocity of $v < c$ in the direction of its spin, it has positive helicity. If one chooses a observing frame that moves faster than the particle $v_{ob} > v$, the particle will be observed as moving opposite to its spin, thus results in negative helicity.

To solve that problem, we can take the consideration that the e^- and the massless ν_e (or with very small mass) are highly relativistic, so $E \approx p \gg m_0$. With the Dirac equation

$$(\boldsymbol{\alpha} \cdot \mathbf{p} + \beta m_0) u = E u, \quad \boldsymbol{\alpha} = \gamma_5 \hat{\mathbf{\Sigma}} = \hat{\mathbf{\Sigma}} \gamma_5 \tag{A.29}$$

and properties of γ matrices in eqn. A.8, the helicity projections on spinor can be approximated to

$$\begin{aligned} \hat{P}_\pm u = \frac{1}{2}(1 \pm \hat{\Lambda}) u = \frac{1}{2} \left(1 \pm \frac{\hat{\mathbf{\Sigma}} \cdot \mathbf{p}}{p} \right) u = \frac{1}{2} \left(1 \pm \gamma_5 \frac{\boldsymbol{\alpha} \cdot \mathbf{p}}{p} \right) u \\ = \frac{1}{2} \left(1 \pm \gamma_5 \frac{E - \beta m_0}{p} \right) u \approx \frac{1}{2}(1 \pm \gamma_5) u \end{aligned} \tag{A.30}$$

Thus the projection operators are formulated as

$$\hat{P}_+ = \frac{1}{2}(1 + \gamma_5), \quad \hat{P}_- = \frac{1}{2}(1 - \gamma_5) \tag{A.31}$$

which are Lorentz invariants, so called as the projection operators on states of positive and negative *chirality*.

It is necessary to note that, the projection operators are deduced when electrons and neutrinos have high velocities. When the leptons have low velocities, the chirality projection operators $\hat{P}_{\pm}$ considerably differ from the helicity projection operators. Therefore, the statement that the electrons always have negative helicity is only approximately correct. However, in nuclear and neutron β decays, the contributions of positive helicity currents are usually too small to be detected.

We apply $\hat{P}_-$ on the lepton wave function to obtain the negative helicity component. For its Dirac adjoint, the projector is transformed as

$$\bar{u} \to \overline{(\hat{P}_- u)} = (\hat{P}_- u)^\dagger \gamma^0 = u^\dagger \hat{P}_-^\dagger \gamma^0 = u^\dagger \left(\frac{1-\gamma_5}{2}\right)^\dagger \gamma^0 = u^\dagger \gamma^0 \frac{1+\gamma_5}{2} = \bar{u}\hat{P}_+ \tag{A.32}$$

Hence the leptonic current under the projection is

$$\bar{u}_e \hat{O}_i u_\nu \to \overline{(\hat{P}_- u_e)} \hat{O}_i (\hat{P}_- u_\nu) = \bar{u}_e \hat{P}_+ \hat{O}_i \hat{P}_- u_\nu = \bar{u}_e \hat{O}_i' u_\nu \tag{A.33}$$

with the modified operators as

$$\hat{O}_i' = \hat{P}_+ \hat{O}_i \hat{P}_- \tag{A.34}$$

With the calculations with eqn. A.8, the results of the modified operators are listed in table A.1.

As it is shown in the table, under the chirality projections, only the V and the A operators remain non-zero. Further, the two modified operators have the same structure: the vector operator γ^μ minus the axial vector operator $\gamma^\mu\gamma_5$.

As a result, for any combinations of $\hat{O}_i$, only V and A currents can finally appear in the Hamiltonian, and they always result in the same $V-A$ structure in the leptonic current. This is the so called $V-A$ theory.

In the neutron decay, the Hamiltonian contributions from V and A are weighted by the coupling constants g_V and g_A in the hadronic current, and stand for the strengths of Fermi and Gamov-Teller transitions, as shown in figure A.2. The ratio of the couplings $\lambda = g_A/g_V$ that induced by strong interactions should be measured in experiments.

A.5 Angular Correlation Coefficients in Free Neutron Decay

Considering the left- and right-handed V, A, S, T currents, the angular correlation coefficients can be derived from eqn. 2.57

$$\xi = |C_V|^2 + |\overline{C}_V|^2 + |C_S|^2 + |\overline{C}_S|^2 + 3|C_A|^2 + 3|\overline{C}_A|^2 + 3|C_T|^2 + 3|\overline{C}_T|^2 \tag{A.35}$$

$$A\xi = 2 \cdot Re(2C_A\overline{C}_A^* - C_V\overline{C}_A^* - \overline{C}_VC_A^* - C_S\overline{C}_T^* - \overline{C}_SC_T^* - 2C_T\overline{C}_T^*) \tag{A.36}$$

$$a\xi = |C_V|^2 + |\overline{C}_V|^2 - |C_A|^2 - |\overline{C}_A|^2 - |C_S|^2 - |\overline{C}_S|^2 + |C_T|^2 + |\overline{C}_T|^2 \tag{A.37}$$

$$B = B_0 + b_\nu \frac{m_e}{E_e}, \qquad \text{with} \tag{A.38}$$

$$B_0\xi = 2 \cdot Re(-2C_A\overline{C}_A^* - C_V\overline{C}_A^* - \overline{C}_VC_A^* + C_S\overline{C}_T^* + \overline{C}_SC_T^* - 2C_T\overline{C}_T^*) \tag{A.39}$$

$$b_\nu\xi = 2 \cdot Re(2C_T\overline{C}_A^* + 2\overline{C}_TC_A^* - C_S\overline{C}_A^* - \overline{C}_SC_A^* + C_V\overline{C}_T^* + \overline{C}_VC_T^*) \tag{A.40}$$

$$b_F\xi = 2 \cdot Re(C_SC_V^* + \overline{C}_S^*\overline{C}_V^* - 3C_TC_A^* - 3\overline{C}_T\overline{C}_A^*) \tag{A.41}$$

Other coefficients can be found in [Jac57]

Appendix B

Motion of Charged Particles in Static Magnetic Field

The motions of charged particles in the non-uniform electromagnetic field are extremely complicated. Fortunately, in an *adiabatic condition*, we are able to obtain approximations of the particle behaviours. More information about this topic can be found in Plasma Physics [Din05].

B.1 Helical Motion of Charged Particles in Magnetic Field

Due to Lorentz force, a charged particle moves helically in the static magnetic field. The gyration radius r is proportional to the momentum component $p_\perp$ that vertical to the magnetic line. Define the *pitch angle* θ as the angle between magnetic field $\mathbf{B}$ and momentum $\mathbf{p}$, the gyration radius is

$$\mathbf{r} = \frac{\mathbf{p} \times \mathbf{B}}{qB^2} = \frac{\mathbf{p}_\perp}{qB}, \quad p_\perp = p \cdot \sin\theta \tag{B.1}$$

B and q are the magnetic field and the charge of the particle. In a static magnetic field, the vertical component of momentum $p_\perp$ rotates around the magnetic field line, and the parallel component $p_\parallel$ determines the propagation speed. If there are no external forces or drift effects on the particle, the gyration center of the particle will always stay on the same magnetic line. With this property, we are able to denote the particle trajectories with magnetic lines.

B.2 Adiabatic Condition and Adiabatic Invariant

If the magnetic field experienced by charged particles changes negligibly in the course of one revolution of the helical motion, the motions of the particles are *adiabatic*. The variation of magnetic field in one helical pitch should fulfil the criterion:

$$\gamma = \left|\frac{\Delta B}{B}\right| = 2\pi \frac{p\cos\theta}{qB^2}\left|\frac{\partial \mathbf{B}}{\partial \mathbf{r}}\right| \ll 1 \tag{B.2}$$

where ΔB is the field variation in one helical distance, $\mathbf{r}$ denotes the position on the route of particle gyration center.

During the adiabatic motion, the magnetic moment of the particle gyration μ is an invariant:

$$\mu = \frac{\frac{1}{2}mv_{\perp}^2}{B} = const. \tag{B.3}$$

With eqn. B.1, the invariant can be equivalently expressed as:

$$\mathbf{L} = \mathbf{r} \times \mathbf{p} = const. \,, \quad \phi = B \cdot \pi r^2 = const. \,, \quad \frac{p_{\perp}^2}{B} = const. \tag{B.4}$$

which indicate the angular momentum $\mathbf{L}$ and magnetic flux of gyration circle ϕ are conserved.

In the non-adiabatic transport of particles, the magnetic moment is not conserved, and the pitch angles will be changed with certain probabilities [Var01].

B.3 Magnetic Mirror Effect and Magnetic Bottle

In a static field, if the external force is not doing work on the particle (e.g. Lorentz force), the energy of a particle remains conserved.

$$p^2 = p_{\parallel}^2 + p_{\perp}^2 = const. \tag{B.5}$$

Together with eqn. B.4, we can see both $p_{\perp}$ and $p_{\parallel}$ change with the B-field. The pitch angle θ of the particle helical motion is a function of B-field:

$$\frac{\sin^2\theta}{B} = const. \quad \text{or} \quad \sin\theta = \sqrt{\frac{B}{B_0}}\sin\theta_0 \tag{B.6}$$

So when a charged particle moves along an increasing magnetic field, the longitudinal momentum $p_{\parallel}$ is transferred to the transverse component $p_{\perp}$, and the pitch angle θ increases. When $p_{\parallel}$ decreases to zero, namely θ increases to 90°, $p_{\parallel}$ will change the sign and the particle will start to move to the reverse direction. The reflection effect caused by the magnetic field gradient is so called as *magnetic mirror effect*, as sketch in figure B.1.

The critical pitch angle $\theta_{crit.}$, which is the maximal pitch angle for the particle to pass through the magnetic mirror $B_{mirr.}$ from B, can be given as:

$$\theta_{mirr.} = 90^{\circ}, \quad \theta_{crit.} = \arcsin\sqrt{\frac{B}{B_{mirr.}}} \tag{B.7}$$

Any charged particles that emitted in B with pitch angle $\theta > \theta_{crit.}$ will be reflected back, while other particles are allowed to pass the $B_{mirr.}$ barrier. The solid angle of transited particles (loss cone) is then given as:

$$\Omega = 2\pi(1 - \cos\theta_{crit.}) \tag{B.8}$$

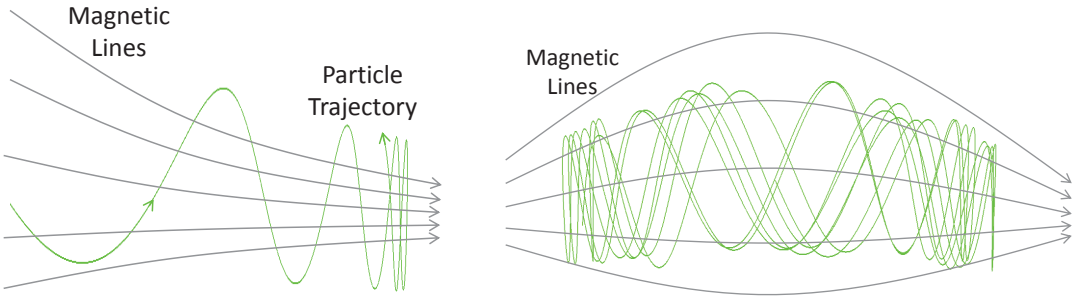

(a) Magnetic mirror **(b)** Magnetic bottle

Figure B.1: Sketches of the magnetic mirror effect and magnetic bottle. The gray lines denote the magnetic lines, green curves denote the trajectories of the charged particles.

With two magnetic mirrors, it can form a *magnetic bottle* to trap the charged particles, as shown in figure B.1. The charged particles emitted in the low field region with the pitch angle $\theta > \theta_{crit.}$ can be reflected by magnetic mirrors from both sides, and keep oscillating inside the minimum range of the magnetic field .

Due to uncontrollable influences, e.g. variations of magnetic field, external forces, non-adiabatic motions, drift effects, collisions with air molecule etc., the trapped particle has probabilities to escape from the magnetic bottle, with the energies or pitch angles distorted by the influences. A theoretical calculation for particle escape probability due to non-adiabatic motion is referred in [Var71]

In neutron decay experiments, the magnetic field minima on the e^-/p^+ or neutron beam can act as magnetic bottles and trap e^-/p^+ inside them. The traps of e^-/p^+ can cause signal losses, and the escaped e^-/p^+ can also reach the detector at an unpredictable time, thus distort the measured results. Therefore, any minima of the magnetic field on e^-/p^+ or neutron beam should be avoided as far as possible.

B.4 Drifts of Charged Particles in Curved Magnetic Field

A charged particle has a drift effect when it is propagating in a curved magnetic field. The approximate drift velocity v_d caused by B-field curvature can be formulated on first order as:

$$\mathbf{v}_d = \frac{m v_\parallel^2}{qRB} \frac{\mathbf{R} \times \mathbf{B}}{RB} \tag{B.9}$$

$\mathbf{R}$ is the curvature of the magnetic line, $v_\parallel$ is the particle velocity along the magnetic field. If we don't consider the electrical current that passes the area of particle's motion, the curved magnetic field has a gradient along the direction of $\mathbf{R}$ according Maxwell equations:

$$\nabla \times \mathbf{B} = 0, \quad \frac{\mathrm{d}B}{\mathrm{d}R} = -\frac{B}{R} \tag{B.10}$$

The magnetic field gradient will cause another drift contribution from the perpendicular velocity $v_\perp$. The total drift velocity is then written as:

$$\mathbf{v}_d = \frac{m}{qRB}\left(v_\parallel^2 + \frac{1}{2}v_\perp^2\right)\frac{\mathbf{R}\times\mathbf{B}}{RB} \tag{B.11}$$

Eqn. B.11 is an approximate description on the first order. It works when the gyration radius of particle r_{gyr} is much smaller than the radius of the curved magnetic field, and the changes of the field strength is negligible during one helical cycle:

$$r_{gyr.} \ll R, \quad r_{gyr}|\nabla\mathbf{B}| \ll B \tag{B.12}$$

To the second order, this formula has a contribution from the variation of $\mathbf{v}_d$ [Erz09]

$$\mathbf{v}_d = \frac{m}{qRB}\left(v_\parallel^2 + \frac{1}{2}v_\perp^2\right)\frac{\mathbf{R}\times\mathbf{B}}{RB} - \frac{m}{B^2}(\dot{\mathbf{v}}_d\times\mathbf{B}) \tag{B.13}$$

As shown in eqn. B.11, the drift caused by curved magnetic field ($\mathbf{R}\times\mathbf{B}$ drift) has a direction perpendicular to the magnetic field and the field curvature.

Appendix C

Compare of Magnetic Field Results from Different Simulation Programs

In the design of magnetic field systems, we mainly use two programs for simulation: the finite element simulation program CST Studio [Cst], and magnetic field calculation program magfield3.c developed by F. Glück [Glu11].

The program CST Studio is a commercial program driven with finite element method, and widely used in high and low frequency electromagnetic field simulations. In static field simulation, it is able to calculate the magnetic field, trajectories of particles, non-linear material and forces. Whereas the finite element method is not very good at defining the accurate magnetic field on a specific point, hence can hardly simulate the magnetic lines. Additionally, the results from CST Studio are dependent on the boundary conditions and the size of calculation domains.

The magfield3.c program is based on C++, and can logically calculate the 3D magnetic field generated by circular magnets on any specified point with high precision. With this feather, we can deduce secondary results from the simulated fields, e.g. the precise distribution of magnetic lines etc.

For the design of PERC, which has only circular magnets, we used both programs for different purposes. The results from the programs based on different calculation methods are compared. The figures below show the relative deviations of the simulated magnetic fields from both programs. The relative deviation is defined as

$$\frac{\Delta B}{B_{mag}} = \frac{B_{CST} - B_{mag}}{B_{mag}} \tag{C.1}$$

In the figures, the deviations are plotted along the central line of the e^-/p^+-beam and along the vertical central line of the selector coil.

As shown in the figures, the deviations are smaller than 5×10^{-3}.

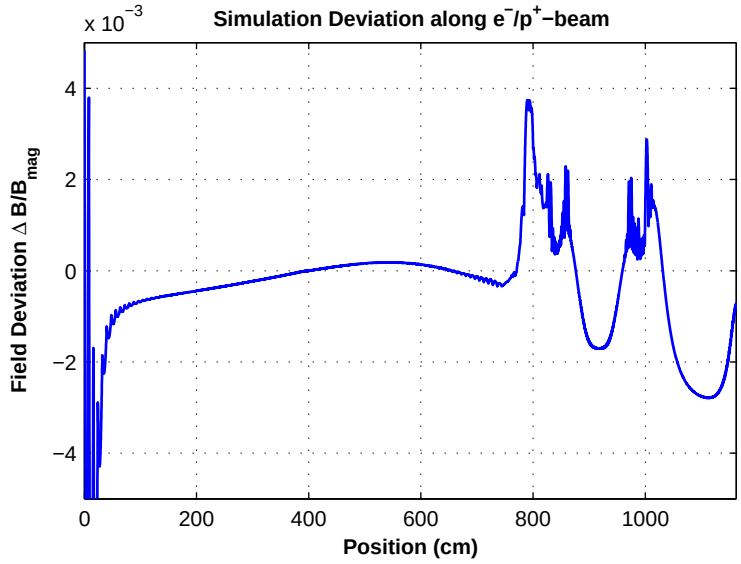

Figure C.1: The relative deviations of the simulated magnetic fields from both programs along the central line of the e^{-}/p^{+}-beam.

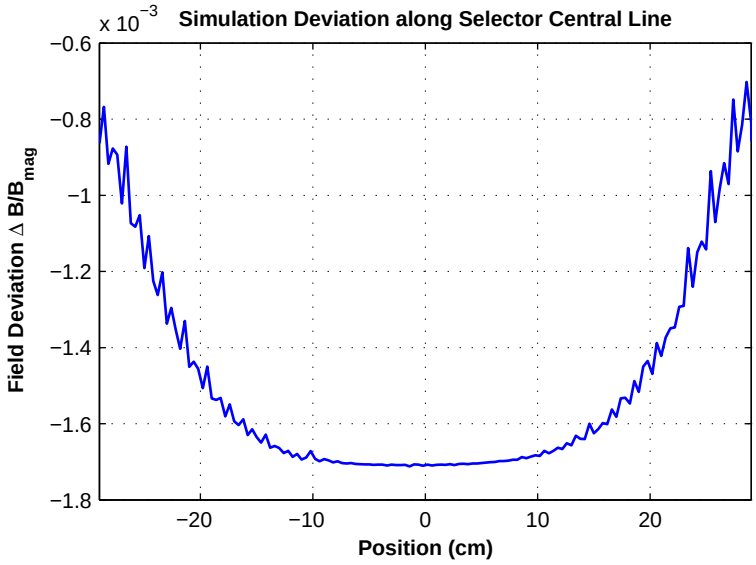

Figure C.2: The relative deviations of the simulated magnetic fields along the central line in y-axis of the selector coil. Zero point denotes the center of selector coil.

Appendix D

Parameters of Magnets of PERC

Table D.1 lists the technical parameters of the magnets of PERC. In the table, some items should be noted:

1. The *Pos.y* and *Pos.z* denote the positions of the centers of the magnets along y- and z-axes. The zero point is located at the center of the n-guide end, directions of y and z are the same as plotted in figure 6.2.
2. The items *Length* and r_{in}, r_{out} denote the lengths and the inner, outer radii of the coils including necessary insulations.
3. In the winding process of the superconducting magnets, every layer of the wires *loses half turn of winding at each ends of the coil* for mechanic filler. Hence the real lengths of the coils are one winding shorter than the product lengths in the table.
4. The correction coils on decay coil *Dec.Corr. 2* and *3* have negative current, and indicate removing windings from the decay coil. They *do not have the half turn losses*.
5. The geometry values denote that in the 4.2 K temperature. The thermal expands must be considered in manufacture.
6. The *current density* is the current density over the cross-section of one wire, i.e. $I/(3.2\times2.4$ mm^2).
7. The current of *Filter Coils* are varied from 0 A to 612 A to tune B_1 from 3T to 6T in experiment.
8. The *Max. B-field* denotes the highest magnetic fields that the coils can experience, which are necessary to determine the *nominal current* (Section 8.1.2).

Coils	Pos.y [mm]	Pos.z [mm]	Angle [°]	r_{in} [mm]	r_{out} [mm]	length [mm]	Max. B-field[T]	Current [A]	Curr.Density [A/mm^2]	Turns	Layers	Turns per layer	Wire length [m]
Decay Coil	0	-4000.0	0	200.0	209.6	8000.0	1.92	954	124.22	9996	4	2499	12863
Decay Corr. 1	0	-7920.0	0	209.6	212.0	160.0	1.32	954	124.22	49	1	49	65
Decay Corr. 2	0	-123.2	0	207.2	209.6	80.0	1.60	-954	-124.22	25	1	25	33
Decay Corr. 3	0	-305.6	0	207.2	209.6	22.4	1.60	-954	-124.22	7	1	7	9
Bend Coil 1	-31	152.9	10.5	254.3	280.7	176.0	2.53	580	75.52	594	11	54	998
Bend Coil 2	40	445.1	22	309.5	338.3	240.0	4.05	580	75.52	888	12	74	1807
Selector Coil	80	1152.3	0	298.0	331.6	880.0	7.31	580	75.52	3836	14	274	7587
Sele.Corr. 1	80	766.7	0	331.6	355.6	108.8	3.70	580	75.52	330	10	33	712
Sele.Corr. 2	80	1537.9	0	331.6	355.6	108.8	3.70	580	75.52	330	10	33	712
Filter Coil 1	80	960.3	0	331.6	434.8	160.0	4.86	610	79.43	2107	43	49	5073
Filter Coil 2	80	1344.3	0	331.6	434.8	160.0	4.86	610	79.43	2107	43	49	5073
Bend Coil 3	34	1868.7	-24	311.8	345.4	240.0	4.25	580	75.52	1036	14	74	2139
Detector coil	0	2635.1	0	250.0	262.0	998.4	1.93	580	75.52	1555	5	311	2501

Table D.1: Parameters of the magnets of PERC.

Bibliography

[Abe00] H. Abele. "The Standard Model and the neutron β-decay". *Nucl. Instr. and Meth. A* **440(3)** (2000) 499–510.

[Abe08] H. Abele. "The neutron. Its properties and basic interactions". *Prog. Part. Nucl. Phys.* **60(1)** (2008) 1–81.

[Abe97] H. Abele et al. "A measurement of the beta asymmetry A in the decay of free neutrons". *Phys. Lett. B* **407(3–4)** (1997) 212–218.

[Abe02] H. Abele et al. "Is the Unitarity of the Quark-Mixing CKM Matrix Violated in Neutron β-Decay?" *Phys. Rev. Lett.* **88** (2002) 211801.

[Abe06] H. Abele et al. "Characterization of a ballistic supermirror neutron guide". *Nucl. Instr. and Meth. A* **562(1)** (2006) 407–417.

[And04] S. Ando et al. "Neutron beta-decay in effective field theory". *Phys. Lett. B* **595(1–4)** (2004) 250–259.

[Bae08] S. Baeßler et al. "First measurements with the neutron decay spectrometer a SPECT". *Eur. Phys. J. A* **38** (2008) 17–26.

[Ban06] G. Ban et al. "A Mott polarimeter for the search of time reversal violation in the decay of free neutrons". *Nucl. Instr. and Meth. A* **565(2)** (2006) 711–724.

[Baz93] A. Bazhenov et al. "An adiabatic resonance spin-flipper for thermal and cold neutrons". *Nucl. Instr. and Meth. A* **332(3)** (1993) 534–536.

[Beg77] M. A. B. Bég et al. "Manifest Left-Right Symmetry and its Experimental Consequences". *Phys. Rev. Lett.* **38** (1977) 1252–1255.

[BD64] J. Bjorken and S. Drell. *Relativistic quantum mechanics*. International series in pure and applied physics. McGraw-Hill (1964).

[Bop86] P. Bopp et al. "Beta-Decay Asymmetry of the Neutron and g_A/g_V". *Phys. Rev. Lett.* **56** (1986) 919–922.

[Bot00] L. Bottura. "A practical fit for the critical surface of NbTi". *IEEE Trans. Appl. Supercond.* **10(1)** (2000) 1054 –1057.

[Cab63] N. Cabibbo. "Unitary Symmetry and Leptonic Decays". *Phys. Rev. Lett.* **10** (1963) 531–533.

[Cha14] J. Chadwick. "The Intensity Distribution in Magnetic Spectrum of β-Rays of Radium B + C". *Verhandl. Dtsch. Phys. Ges* **16** (1914) 383.

[Cha32] J. Chadwick. "Possible Existence of a Neutron". *Nature* **129** (1932) 312.

[Cla97] K. Clausen et al. "The RITA spectrometer at Risø — design considerations and recent results". *Phys. B* **241–243(0)** (1997) 50–55.

[CB83] E. Commins and P. Bucksbaum. *Weak Interactions of Leptons and Quarks*. Cambridge University Press (1983). ISBN 9780521273701.

[Cst] CST Computer Simulation Technology AG. Url: http://www.cst.com/.

[Cza04] A. Czarnecki et al. "Precision measurements and CKM unitarity". *Phys. Rev. D* **70** (2004) 093006.

[Cza07] A. Czarnecki et al. "Electroweak Radiative Corrections to Muon Capture". *Phys. Rev. Lett.* **99** (2007) 032003.

[Dai] Daimler-Benz Aerospace, Dornier Satellitensysteme GmbH. "Neutron Velocity Selector, Blade rotor developed by Dornier/GKSS/PTB." Datasheet.

[Del88] L. Delves and J. Mohamed. *Computational Methods for Integral Equations*. Cambridge University Press (1988). ISBN 9780521357968.

[Din05] A. Dinklage. *Plasma Physics: Confinement, Transport And Collective Effects*. Lecture Notes in Physics. Springer (2005). ISBN 9783540252740.

[Don94] J. Donoghue et al. *Dynamics of the Standard Model*. Cambridge Monographs on Particle Physics, Nuclear Physics and Cosmology. Cambridge University Press (1994). ISBN 9780521476522.

[Dub08] D. Dubbers et al. "A clean, bright, and versatile source of neutron decay products". *Nucl. Instr. and Meth. A* **596(2)** (2008) 238–247.

[Dub08PSF] D. Dubbers et al. "The point spread function of electrons in a magnetic field, and the beta-decay of free neutrons" ArXiv:0812.0347v1.

[EAS] EAS-Bruker, Bruker Corporation. Url: http://www.bruker-est.com/lts-dir.html.

[Erz09] D. Eržen et al. "Simulations of single charged particle motion in external magnetic and electric fields". *Eur. Phys. J. D* **54** (2009) 409–415.

[Fer34] E. Fermi. "Versuch einer Theorie der β-Strahlen. I". *Zeitschrift für Physik A Hadrons and Nuclei* **88** (1934) 161–177.

[GT36] G. Gamow and E. Teller. "Selection Rules for the β-Disintegration". *Phys. Rev.* **49** (1936) 895–899.

[Gla61] S. L. Glashow. "Partial-symmetries of weak interactions". *Nucl. Phys.* **22(4)** (1961) 579–588.

[Glu11] F. Glück. "AXISYMMETRIC MAGNETIC FIELD CALCULATION WITH ZONAL HARMONIC EXPANSION". *Prog. Electromagn. Res. B* **32** (2011) 351–388.

[Glu95] F. Glück et al. "Measurable parameters of neutron decay". *Nucl. Phys. A* **593(2)** (1995) 125 – 150.

[GT92] F. Glück and K. Tóth. "Order-α radiative corrections for semileptonic decays of polarized baryons". *Phys. Rev. D* **46** (1992) 2090–2101.

[Gol58] M. Goldhaber et al. "Helicity of Neutrinos". *Phys. Rev.* **109** (1958) 1015–1017.

[Gre00] W. Greiner and B. Müller. *Gauge Theory of Weak Interactions*. Physics and Astronomy Online Library. Springer (2000). ISBN 9783540676720.

[Gud06] V. Gudkov et al. "General classification and analysis of neutron β-decay experiments". *Phys. Rev. C* **73** (2006) 035501.

[HT05] J. C. Hardy and I. S. Towner. "New Limits on Fundamental Weak-Interaction Parameters from Superallowed β Decay". *Phys. Rev. Lett.* **94** (2005) 092502.

[HT09] J. C. Hardy and I. S. Towner. "Superallowed $0^+ \rightarrow 0^+$ nuclear β decays: A new survey with precision tests of the conserved vector current hypothesis and the standard model". *Phys. Rev. C* **79** (2009) 055502.

[HM89] J. B. Hayter and H. A. Mook. "Discrete thin-film multilayer design for X-ray and neutron supermirrors". *J. Appl. Crystallogr.* **22(1)** (1989) 35–41.

[Her01] P. Herczeg. "Beta decay beyond the standard model". *Prog. Part. Nucl. Phys.* **46(2)** (2001) 413–457.

[Hol74] B. R. Holstein. "Recoil effects in allowed beta decay: The elementary particle approach". *Rev. Mod. Phys.* **46** (1974) 789–814.

[Hae02] H. Häse et al. "A long ballistic supermirror guide for cold neutrons at ILL". *Nucl. Instr. and Meth. A* **485(3)** (2002) 453–457.

[HS95] J. H. Hubbell and S. M. Seltzer. "Tables of x-ray mass attenuation coefficients and mass energy-absorption coefficients 1 keV to 20 MeV for elements Z = 1 to 92 and 48 additional substances of dosimetric interest". Tech. Rep. 5632, NIST, Gaithersburg, MD (1995).

[Jac57] J. D. Jackson et al. "Possible Tests of Time Reversal Invariance in Beta Decay". *Phys. Rev.* **106** (1957) 517–521.

[PDG12] J.Beringer et al. (Particle Data Group). "Review of Particle Physics". *Phys. Rev. D* **86** (2012) 010001.

[Kno10] G. Knoll. *Radiation Detection and Measurement*. John Wiley & Sons (2010). ISBN 9780470131480.

[KM73] M. Kobayashi and T. Maskawa. "*CP*-Violation in the Renormalizable Theory of Weak Interaction". *Prog. Theor. Phys.* **49(2)** (1973) 652–657.

[Kon11] G. Konrad. "Measurement of the Proton Recoil Spectrum in Neutron Beta Decay with the Spectrometer aSPECT: Study of Systematic effects". Ph.D. thesis, University of Mainz (2011).

[Kon12] G. Konrad et al. "Neutron Decay with PERC: a Progress Report". *Journal of Physics: Conference Series* **340(1)** (2012) 012048.

[Koz09] A. Kozela et al. "Measurement of the Transverse Polarization of Electrons Emitted in Free-Neutron Decay". *Phys. Rev. Lett.* **102** (2009) 172301.

[Kre05] M. Kreuz et al. "The crossed geometry of two super mirror polarisers—a new method for neutron beam polarisation and polarisation analysis". *Nucl. Instr. and Meth. A* **547(2–3)** (2005) 583–591.

[LY56] T. D. Lee and C. N. Yang. "Question of Parity Conservation in Weak Interactions". *Phys. Rev.* **104** (1956) 254–258.

[Lub83] M. Lubell. "Empirical scaling formulas for critical current and critical field for commercial NbTi". *IEEE. T. Magn.* **19(3)** (1983) 754–757.

[Mes11] H. Mest. "Measurement of the β-Asymmetry in the Decay of Free Polarized Neutrons with the Spectrometer PERKEOIII". Ph.D. thesis, Universität Heidelberg (2011).

[Mae09] B. Märkisch et al. "The new neutron decay spectrometer Perkeo III". *Nucl. Instr. and Meth. A* **611(2–3)** (2009) 216–218.

[Mun12] D. Mund et al. "Determination of the Weak Axial Vector Coupling from a Measurement of the Beta-Asymmetry Parameter A in Neutron Beta Decay" ArXiv:1204.0013v1.

[Pre07] W. Press. *Numerical Recipes: The Art of Scientific Computing*. Cambridge University Press (2007). ISBN 9780521880688.

[abBA07] R. Alarcon et al. "The abBA Experiment Proposal" (2007).

[Ram08] M. Ramsey-Musolf and S. Su. "Low-energy precision tests of supersymmetry". *Phys. Rep.* **456(1–2)** (2008) 1–88.

[Rav95] C. Raven. "Erste Messungen mit Perkeo II:b-Asymmetrie im Neutron-Zerfall". Master's thesis, Universität Heidelberg (1995).

[Rei00] J. Reich et al. "A measurement of the beta asymmetry in neutron decay with PERKEO II". *Nucl. Instr. and Meth. A* **440(3)** (2000) 535–538.

[RK11] T. Rekveldt and W. Kraan. "Spin flippers for Larmor labeling methods in monochromatic and white neutron beams". *Nucl. Instr. and Meth. A* **629(1)** (2011) 239–244.

[RT99] A. Riotto and M. Trodden. "RECENT PROGRESS IN BARYOGENESIS". *Annu. Rev. Nucl. Part. Sci.* **49(1)** (1999) 35–75.

[Sal68] A. Salam. "Elementary Particle Physics: Relativistic Groups and Analyticity". *Almquvist and Wiksell* **Stockholm** (1968) 367.

[Sch07d] M. Schumann. "Measurement of Neutrino and Proton Asymmetry in the Decay of polarized Neutrons". Ph.D. thesis, Universität Heidelberg (2007).

[Sch07] M. Schumann et al. "Measurement of the Neutrino Asymmetry Parameter *B* in Neutron Decay". *Phys. Rev. Lett.* **99** (2007) 191803.

[Sch08] M. Schumann et al. "Measurement of the Proton Asymmetry Parameter in Neutron Beta Decay". *Phys. Rev. Lett.* **100** (2008) 151801.

[Sev06] N. Severijns et al. "Tests of the standard electroweak model in nuclear beta decay". *Rev. Mod. Phys.* **78** (2006) 991–1040.

[Sim09] M. Simson et al. "Measuring the proton spectrum in neutron decay—Latest results with aSPECT". *Nucl. Instr. and Meth. A* **611** (2009) 203–206.

[Sir67] A. Sirlin. "General Properties of the Electromagnetic Corrections to the Beta Decay of a Physical Nucleon". *Phys. Rev.* **164** (1967) 1767–1775.

[Sir75] A. Sirlin. "Generalization of the radiative corrections to β and μ decays in the SU(2)L × U(1) gauge model". *Nucl. Phys. B* **100(2)** (1975) 291–301.

[Sol02] T. Soldner et al. "Installation and first tests of the new PF1b polariser". Tech. rep., ILL (2002).

[Tow92] I. Towner. "The nuclear-structure dependence of radiative corrections in superallowed Fermi beta-decay". *Nucl. Phys. A* **540** (1992) 478 – 500.

[Tre58] S. B. Treiman. "Recoil Effects in *K* Capture and β Decay". *Phys. Rev.* **110** (1958) 448–450.

[Tur67] V. F. Turchin. "Deposited Paper". *At. Energy* **22** (1967) No. 2.

[Var71] R. K. Varma. ""Wave-Mechanical" Model for the Nonadiabatic Loss of Particles from Magnetic-Mirror Traps". *Phys. Rev. Lett.* **26** (1971) 417–420.

[Var01] R. K. Varma. "Probability amplitude description of the dynamics of charged particles in a magnetic field in the macrodomain". *Phys. Rev. E* **64** (2001) 036608.

[Wei67] S. Weinberg. "A Model of Leptons". *Phys. Rev. Lett.* **19** (1967) 1264–1266.

[Wer09] D. Werder. "Development and Characterization of a Pulsed Beam for Neutron Decay Experiments". Master's thesis, Universität Heidelberg (2009).

[Wie05] F. Wietfeldt et al. "A backscatter-suppressed beta spectrometer for neutron decay studies". *Nucl. Instr. and Meth. A* **538(1–3)** (2005) 574–591.

[Wie09] F. Wietfeldt et al. "aCORN: An experiment to measure the electron–antineutrino correlation in neutron decay". *Nucl. Instr. and Meth. A* **611(2–3)** (2009) 207 – 210.

[Wil82] D. Wilkinson. "Analysis of neutron β-decay". *Nucl. Phys. A* **377(2–3)** (1982) 474–504.

[McS] P. Willendrup et al. "User and Programmers Guide to the Neutron Ray-Tracing Package McStas, Version 1.12" (2009).

[Wil88] W. Williams. *Polarized neutrons*. Oxford series on neutron scattering in condensed matter. Clarendon Press (1988). ISBN 9780198510055.

[Wil87] M. Wilson. *Superconducting Magnets*. Monographs on Cryogenics. Oxford University Press, USA (1987). ISBN 9780198548102.

[Wu57] C. S. Wu et al. "Experimental Test of Parity Conservation in Beta Decay". *Phys. Rev.* **105** (1957) 1413–1415.

[Zei06] K. Zeitelhack et al. "Measurement of neutron flux and beam divergence at the cold neutron guide system of the new Munich research reactor FRM-II". *Nucl. Instr. and Meth. A* **560(2)** (2006) 444–453.

[Zim00] O. Zimmer et al. ""aspect" – a new spectrometer for the measurement of the angular correlation coefficient a in neutron beta decay". *Nucl. Instr. and Meth. A* **440** (2000) 548–556.

Acknowledgements

I would like to take this opportunity to appreciate my friends and colleagues, from whom I have acquired a lot of helps during my doctoral work.

I would like to express my sincere gratitude to my supervisor, Univ. Prof. Dr. Hartmut Abele, who offers me this unique opportunity for the interesting subject, on which I was able to make efforts. From the experiment of PERKEOIII in Grenoble, to the design of the PERC, I have received much valuable guidance, assistances, and supports from Prof. Abele. During the doctoral work, I learned from him much knowledges, which are always very helpful and instructive.

I would like to thank my colleagues Dr. Gertrud Konrad and Miss Jacqueline Erhart of our PERC group in Atominstitut TU Wien. The collaboration with them is always pleased. From the discussions with them, I can usually learn constructive suggestions and ideas. I am obliged to Dr. Konrad, for her very helpful supports of the quantity limit calculations in this dissertation.

I would like to thank my colleagues Prof. Dr. Torsten Soldner of ILL, Dr. Holger Mest, Dr. Bastian Maerkisch, and Mr. Dominik Werder of University of Heidelberg. In 2008 to 2009, we collaborate on the experiment of PERKEOIII. This is an impressive and rare experience, that working with them on such big instrument. I am grateful to Dr. Mest that I learned much knowledge from him about the electronics and programming.

I would like to thank my colleagues Mr. Harald Fillunger, Dr. Reinhard Maix, and Mr. Miklos Horvath of Atominstitut TU Wien. During the design of PERC, I got much supports and advices from them for mechanic and the magnet design. I also learned a lot of useful knowledges related to the superconducting magnets from Mr. Fillunger and Dr. Maix.

Finally, I would like to thank all people who helped and supported me during the period of my doctoral work.